Energy & Environmental Science

ROYAL SOCIETY OF CHEMISTRY

REVIEW

View Article Online
View Journal | View Issue

Cite this: *Energy Environ. Sci.*, 2020, **13**, 4450

Li-rich cathodes for rechargeable Li-based batteries: reaction mechanisms and advanced characterization techniques

Wenhua Zuo, [a] Mingzeng Luo, [a] Xiangsi Liu, [a] Jue Wu,[a] Haodong Liu,[b] Jie Li, *[cd] Martin Winter,[ce] Riqiang Fu, [f] Wanli Yang [g] and Yong Yang *[a]

Received 27th May 2020,
Accepted 18th September 2020

DOI: 10.1039/d0ee01694b

rsc.li/ees

Due to their high specific capacities beyond 250 mA h g^{-1}, lithium-rich oxides have been considered as promising cathodes for the next generation power batteries, bridging the capacity gap between traditional layered-oxide based lithium-ion batteries and future lithium metal batteries such as lithium sulfur and lithium air batteries. However, the practical application of Li-rich oxides has been hindered by formidable challenges. To address these challenges, the understanding of their electrochemical behaviors becomes critical and is expected to offer effective guidance for both materials and cell development. This review aims to provide fundamental insights into the reaction mechanisms, electrochemical challenges and modification strategies of lithium-rich oxides. We first summarize the research history, the pristine structures, and the classification of lithium-rich oxides. Then we review the critical reaction mechanisms that are closely related to their electrochemical features and performances, such as lattice oxygen oxidation, oxygen vacancy formation, transition-metal migration, layered to spinel transitions, 'two-phase mechanism', and lattice evolution. These discussions are coupled with state-of-the-art characterization techniques. As a comparison, the anionic redox reactions of layered sodium transition metal oxides are also discussed. Finally, after a brief overview of the correlation among the aforementioned mechanisms, we provide perspectives on the rational design of lithium-rich oxides with high energy densities and long-term cycling stability.

Broader context

Electric vehicles are a promising solution to the challenges of green energy security, climate change, local air quality, and geopolitical concerns of fossil fuels. To meet the demands of long-distance driving and low-cost electric vehicles, advanced rechargeable lithium batteries with enhanced energy densities are needed, which triggers the extensive pursuit of novel cathode materials with high average working potentials and/or large capacities. High-voltage cathodes, *e.g.* $LiNi_{0.5}Mn_{1.5}O_2$ spinel and polyanionic compounds Li(Co, Ni)PO_4, generally suffer from limited specific capacity, severe electrolyte decomposition, fast electrode degradation, and the consequent safety issues. In contrast, lithium-rich oxides exhibit enhanced specific capacities (>250 mA h g^{-1}) and energy densities (>900 W h kg^{-1}), which satisfy the needs of the next generation rechargeable lithium batteries for large-scale grid storage and electric vehicles. However, undesirable issues like large initial irreversible capacity and severe voltage decay seriously hinder their practical application. This paper aims to comprehensively review the research history, up-to-date progress, recently employed advanced characterization techniques, and trends in the studies of reaction mechanisms of lithium-rich materials, *i.e.* redox mechanisms, structural transformations, interfacial reactions, and their intrinsic relationships. We hope to provide valuable considerations for future studies on lithium-rich materials from the perspective of practical applications.

[a] *State Key Laboratory for Physical Chemistry of Solid Surfaces and Department of Chemistry College of Chemistry and Chemical Engineering, Xiamen University, Xiamen, 361005, People's Republic of China. E-mail: yyang@xmu.edu.cn*
[b] *Department of NanoEngineering, University of California San Diego, La Jolla, California 92093, USA*
[c] *Helmholtz-Institute Münster (IEK-12), Forschungszentrum Jülich GmbH, Corrensstraße 46, 48149, Münster, Germany*
[d] *Department of Energy, Politecnico di Milano, Via Lambruschini, 4, 20156 Milano, Italy. E-mail: jie1.li@polimi.it*
[e] *MEET Battery Research Center, University of Münster, Corrensstraße 46, 48149, Münster, Germany*
[f] *National High Magnetic Field Laboratory, 1800 E. Paul Dirac Drive, Tallahassee, FL 32310, USA*
[g] *Advanced Light Source, Lawrence Berkeley National Laboratory, Berkeley, California 94720, USA*

1. Introduction

Due to their superior properties, especially their high gravimetric/volumetric energy densities and long lifetimes, lithium-ion batteries (LIBs) have led the market of energy storage systems for EVs (Fig. 1a).[1–5] Although present EVs based on LIBs support a vehicle range of more than 300 km and almost meet the daily needs of urban life, many key parameters, *e.g.*, the driving distance, cost, lifetime, charging speed and safety, still fall behind consumers' expectations.[6–8] To meet the criteria of the next generation power batteries,[9–11] a variety of advanced anodes, cathodes, and electrolytes have been proposed and have attracted enormous attention.[12–17] In particular, as the bottleneck of battery capacity and energy density, the reversible specific capacities of commercially available cathodes remain lower than 200 mA h g^{-1}.[18,19] Considering the practical capacity of 700–2000 mA h g^{-1} for silicon–carbon compounds and a high theoretical capacity of 4200 mA h g^{-1} and 3860 mA h g^{-1} displayed by silicon and Li metal, respectively,[20–24] the development, improvement, and optimization of battery cathode materials have become crucial for achieving high energy density of LIBs and for meeting the demands of EV applications.[25,26] When it comes to lithium metal batteries, the identification of high capacity cathodes is equally important to realize the advantages of high capacity Li metal anodes also in practice.[27]

Commercially available cathodes for LIBs include layered $LiCoO_2$(LCO), spinel $LiMn_2O_4$(LMO), olivine $LiFePO_4$(LFP), layered $LiNi_xCo_yMn_{1-x-y}O_2$ (NCM) and $LiNi_xCo_yAl_{1-x-y}O_2$ (NCA). Their cost, volumetric and specific energy densities are shown in Fig. 1b. Due to its high electronic and Li^+-ion

Wenhua Zuo

Wenhua Zuo received his Bachelor's degree from Lanzhou University and his Master's degree from Central China Normal University. He is now a PhD candidate under the supervision of Prof. Yong Yang in Xiamen University. His research interests focus on Li/Na layered transition metal oxide cathodes.

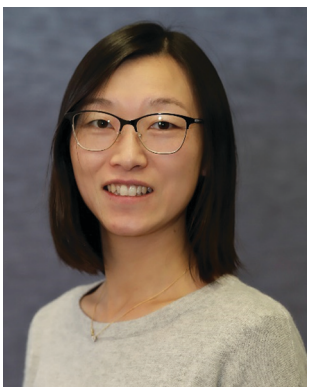

Jie Li

Jie Li received her PhD in Chemistry from Xiamen University and carried out her post-doctoral research at the MEET Battery Research Center in the University of Münster. From 2012 to 2018, she was co-funded by three German ministries (BMBF, BMWi and BMU) to lead an independent young research group. Then, she joined Helmholtz Institute Muenster as a group leader. Currently, she works as an associate professor at the Department of Energy in Politecnico di Milano, Italy (from September 2020) and also serves as the Editor of the Journal of Power Sources. Her main research interest focuses on materials synthesis and characterization for Li- and Na-ion batteries.

Martin Winter

Martin Winter has been researching in the field of electrochemical energy storage and conversion for almost 30 years. His focus is on the development of new materials, components and cell design for lithium ion, lithium–metal batteries and alternative battery systems. He is the founder and scientific director of the MEET Battery Research Center at the Münster University and of the Helmholtz-Institute Münster (HI MS), a division of Forschungszentrum Jülich. Among more than 40 awards and recognitions, he holds the Carl Wagner Memorial Award of the Electrochemical Society (ECS) and the renowned Braunschweig Research Prize.

Riqiang Fu

Riqiang Fu obtained his PhD in 1992 from the Wuhan Institute of Physics in honor of the Academic President Award of the Chinese Academy of Sciences. After a post-doctoral fellowship at the University of Lausanne, Switzerland, in 1994, he worked at the National High Magnetic Field Laboratory (NHMFL) at Florida State University. Currently he is a Research Faculty III at NHMFL. He specializes in solid-state NMR methodology development and NMR applications in materials science (such as lithium ion battery materials) and biological systems (such as membrane proteins).

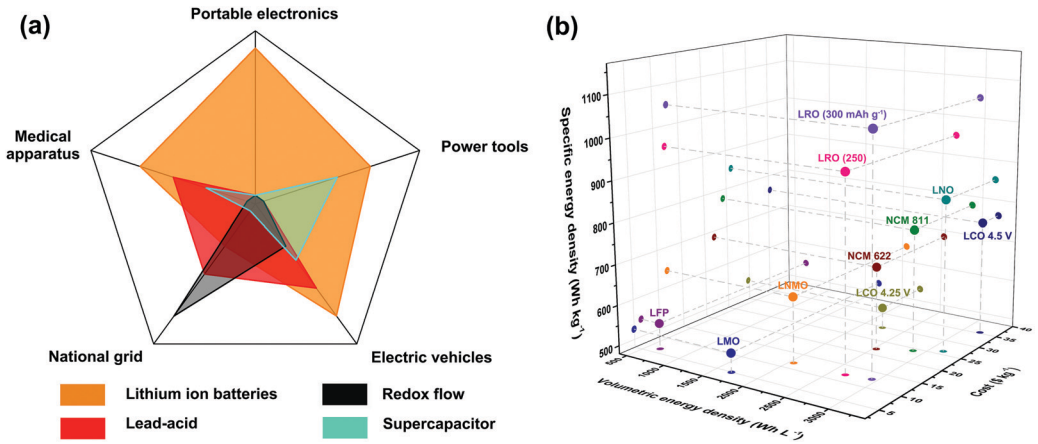

Fig. 1 (a) Main markets of the state-of-the-art rechargeable electrochemical energy storage devices. (b) The volumetric/specific energy densities and cost of prevailing cathode materials for lithium ion batteries.

conductivities, LCO, the first commercialized cathode by Sony Corporation in 1990,[28] has been widely used in battery cells for portable electronics. One of the recent challenges of LCO has been how to enhance its upper charge voltage for achieving high energy density while maintaining good cycling stability.[29,30] Although LCO was applied in EV power battery packs by Panasonic,[31] the limited reserves and high toxicity of Co and the low practical capacity and poor safety of LCO at high temperature make it a substandard candidate for large scale energy storage and EVs. Spinel $LiMn_2O_4$[32] and olivine $LiFePO_4$[33,34] have distinct advantages such as low cost and abundant supply of raw materials, highly reversible structural changes, outstanding thermal stability and environmental benignity.[7,35–37] However, their limited capacity and energy density are intrinsic drawbacks that withhold their further application in EVs. In recent years, layered NCM and NCA have quickly occupied the market of power tools and EVs, owing to their relatively high practical capacity and the flexibility of tuning energy and power densities by adjusting the type and stoichiometry of metal ions. Generally, higher Ni content offers higher capacity but poorer safety, employment of Mn or Al provides good cycling and thermal stability, and Co helps to maintain excellent electronic/ionic conductivity.[38,39] However, even if the challenges of Ni-rich materials ($x \geq 0.8$), such as oxygen evolution, volume expansion, poor thermal stability and insufficient service life, could be overcome by adopting novel synthesis procedures, surface modifications, and structural design, their energy densities in full cells reach only 300 W h kg^{-1} at the cell level which is far below the targeted 400 W h kg^{-1}.[40,41] The aforementioned cathode materials might be optimized and used in EVs in the near term, but cathodes with new chemistry and redox mechanisms are in pressing demand to achieve higher energy densities of LIBs beyond those of the conventional materials for EVs in the longer term.

Lithium-rich oxides (LROs) have been considered as the next-generation cathodes for LIBs for a long time, because they

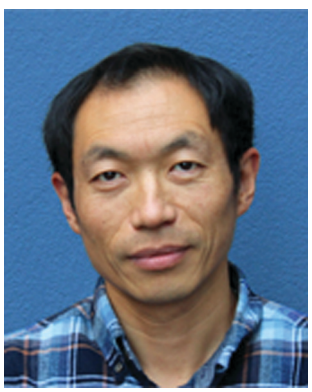

Wanli Yang

Dr Wanli Yang is a senior staff scientist at the Advanced Light Source of Lawrence Berkeley National Laboratory. His research interest focuses on technical developments and scientific applications of soft X-ray spectroscopy for energy science. He developed and formalized the quantitative analysis of both bulk and surface 3d transition-metal oxidation states in battery electrodes through combined spectroscopic tools and fittings. He led the development of high-efficiency mapping of resonant inelastic X-ray scattering (mRIXS) for battery research and introduced mRIXS to the field as a reliable and direct probe for the cationic and anionic states in batteries.

Yong Yang

Yong Yang is a distinguished professor of Chemistry in the State Key Lab for Physical Chemistry of Solid Surface at Xiamen University. He also serves as the Editor of J. Power Sources and the Board Member of International Battery Materials Association (IBA) and International Meeting of Lithium Battery (IMLB). His main research interests are new electrode/electrolyte materials for Li/Na-ion batteries, in situ spectroscopic techniques, and the interfacial reaction mechanism study of electrochemical energy storage and conversion systems.

have provided so far the best rechargeable capacity (over 250 mA h g^{-1}) and average discharge potential (>3.5 V *vs.* Li/Li^+).[42] The high capacity is provided by the cumulative cationic and anionic redox reactions of LROs, and the high content of manganese guarantees good safety and low cost. Thus, LROs are considered as potential cathodes that can bridge the energy density gap between the conventional layered oxide based LIBs and future lithium–sulfur (Li–S) batteries and lithium–air (Li–O_2) batteries. However, obstacles to their practical applications still exist, such as large initial irreversible capacity, inferior cycling stability, poor rate capability, and severe voltage decay, during cycling. Up to now, a great number of studies have been carried out to understand the fundamental mechanisms of LROs such as lattice oxygen redox reactions, O_2 release, transition metal (TM) migration, layered to spinel-like phase (LS) transitions, and the activation of low-voltage redox couples. Due to differences in their local structures arising from different synthesis conditions and stoichiometries and information obtained from various characterization methods, their charge-compensation and structural transition mechanisms remain elusive. Moreover, a great number of layered sodium transition metal oxides, which can be applied as cathodes for sodium ion batteries, have also drawn much attention recently due to their anionic redox reactions and unique structural features. Therefore, a review with a detailed discussion of the intrinsic connection between the anionic redox reactions, structural evolution, and electrochemical characteristics of LROs will be highly appreciated.

Previous reviews on LROs either focused on specific aspects, such as pristine structures and structural transformations,[43–46] anionic redox reactions,[47–50] and lithium-rich oxides with disordered cations,[51] or tended to collect recent advances in characterization, electrode modifications, and chemical/structural transitions.[52–56] Therefore, this review aims to provide fundamental insights into the electrochemical features and performances of LROs focusing on the intrinsic chemical and structural evolution. Importantly, by comparing evidence and the characterization results of the reaction mechanisms, debates and controversies are summarized to guide future developments. Detailed discussions are presented not only in terms of key aspects such as challenges like oxygen evolution, TM migration, phase transformations and voltage fade, strategies like the modification of materials, and newly emerging compounds like sodium-rich oxides, but also in terms of yet less discussed aspects and vital issues including electrolyte compatibility, two-phase reaction mechanisms, and advanced characterization techniques. Last but not least, formidable challenges and prospects for future research on lattice oxygen redox reactions are further elaborated.

2. Brief view on LROs

2.1 Research history of LROs

LROs are a set of lithium transition metal oxides ($Li_{1+x}TM_{1-x}O_2$) with the Li/TM ratio greater than 1 ($0 < x < 1$), such as Li_2MnO_3 and Li_2RuO_3. They attracted extensive interest due to their unique electrochemical properties and complex energy storage mechanisms. To illustrate the research history of LROs, a brief timeline with milestones in the development is displayed in Fig. 2. The investigation of LRO materials, such as layered Li_2SnO_3[57] and Li_2MnO_3,[58] dated back to the 1960s, was much earlier than the development of LIBs.[59] However, compared to the conventional lithium layered oxides, the excess Li^+ results in a high valence state of transition metal ions and thus those materials have not been initially envisaged as potential cathodes for LIBs. In the 1990s, due to the high abundance, low-cost and low toxicity of Mn element, layered $LiMnO_2$ had attracted an enormous number of researchers.[60] Thackeray's group, in 1991, tried to obtain $LiMnO_2$ by leaching Li_2O from Li_2MnO_3 *via* acid treatment and found that the final product $Li_{1.09}Mn_{0.91}O_2$ exhibits electrochemical activities.[61] Up to now, this has been the pioneering finding on the electrochemical behavior of LRO type materials that signals the beginning of LRO research (Fig. 2). In the following ten years, only a few papers presented the electrochemical performance of Li_2MnO_3 and its analogues,[62–65] and their specific capacities reported in these articles were not attractive due to the low upper cut-off potential applied (<4.3 V *vs.* Li/Li^+).

Another milestone was reached in 2001 when Dahn's group firstly charged a series of $Li[Ni_xLi_{(1/3-2x/3)}Mn_{(2/3-x/3)}]O_2$ electrodes to 4.8 V in the first cycle and found that they delivered high reversible capacities of 220 mA h g^{-1} at 55 °C in the voltage range of 2.0–4.6 V.[42] A year later, by using the electrochemical study, powder neutron diffraction (ND), and *in situ* X-ray diffraction (XRD), Lu *et al.*[78–80] performed a comprehensive analysis of the initial structures, electrochemistry, and structural evolution of layered $Li[Ni_xLi_{(1/3-2x/3)}Mn_{(2/3-x/3)}]O_2$ and $Li[Cr_xLi_{(1/3-2x/3)}Mn_{(2/3-x/3)}]O_2$ electrode materials. They further provided a 'lattice oxygen extraction' mechanism to interpret the irreversible plateau (*i.e.* 'activation plateau') and extra capacities in the initial charge process, which had a profound influence on the following research on LROs. Nearly at the same time, based on thermogravimetric analysis-mass spectrometry (TGA-MS) results, Bruce's group put forward the famous "Li^+–H^+ exchange" mechanism to explain the electrochemical activity of Li_2MnO_3.[81–83] Five years later, the Li^+–H^+ exchange mechanism was proved to be a parasitic side reaction when layered lithium-rich Mn-rich oxides ($Li[Li_xNi_yCo_zMn_{1-x-y-z}]O_2$, LMROs) worked in the high voltage range (4.5–4.8 V);[84] however, this mechanism made contribution to the modification of LROs.[85,86] Other charge compensation mechanisms, such as the further oxidation of Mn^{4+},[87] have been excluded with the enrichment of materials systems and the development of characterization techniques.[88] Importantly, in 2006, Bruce's group[66] confirmed the O_2 releasing phenomenon in LMROs for the first time by differential electrochemical mass spectroscopy (DEMS), which is one of the most intimidating challenges of LROs. Delmas *et al.*[84] also observed an increase in the TM/O ratio at the end of the charging plateau by the XRD refinement, consistent with the O_2 loss. In that article,[66] the observation of Ni/Mn condensation provided hints about a "two-phase" mechanism, which was put

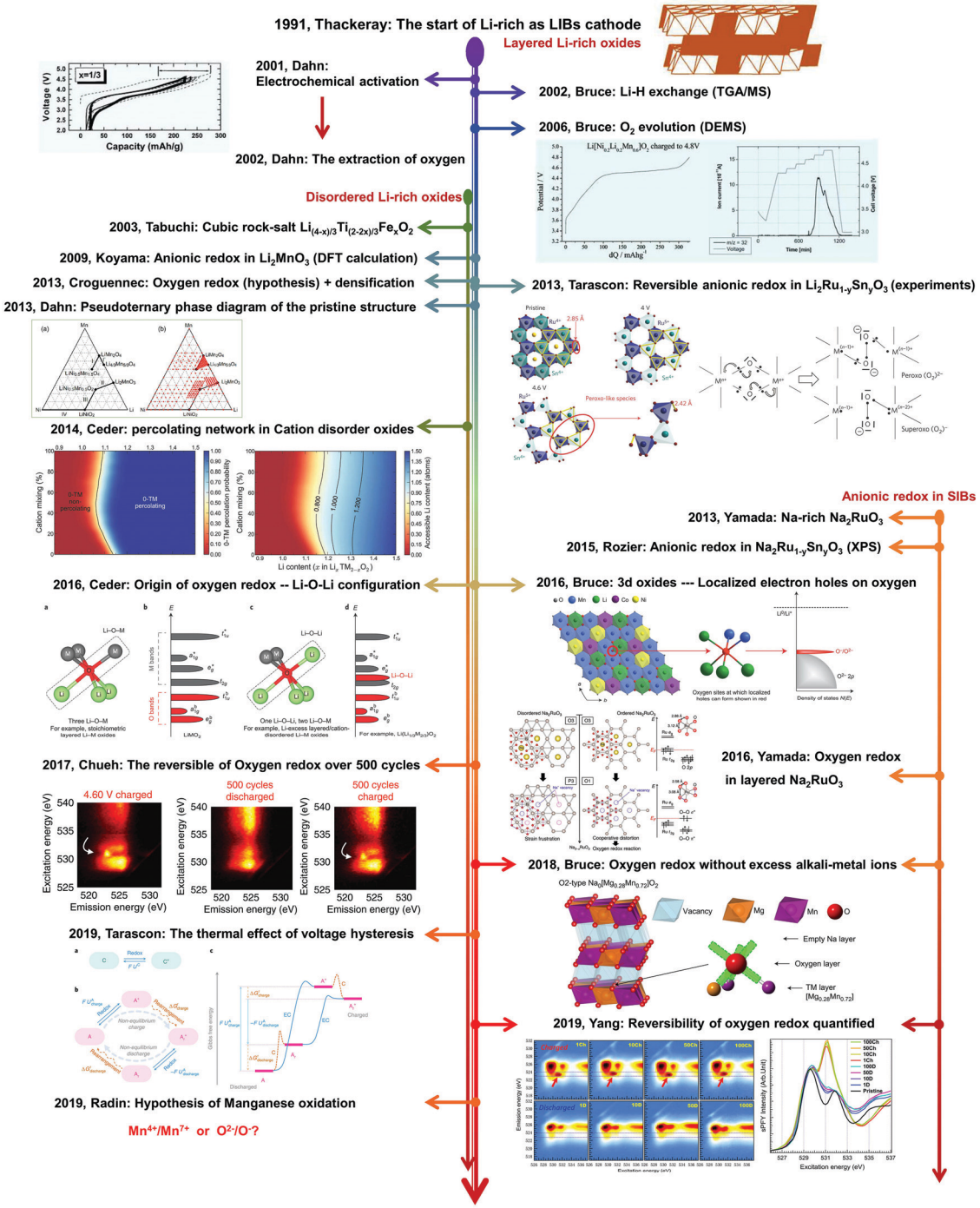

Fig. 2 Brief timeline of the milestones in the development of lithium-rich oxides. Reproduced with permission,[61] Copyright 1991, Elsevier. Reproduced with permission,[42] Copyright 2001, The electrochemical Society. Reproduced with permission,[66] Copyright 2006, American Chemical Society. Reproduced with permission,[67] Copyright 2013, American Chemical Society. Reproduced with permission,[68] Copyright 2013, Nature Publishing group. Reproduced with permission,[69] Copyright 2014, Nature Publishing group. Reproduced with permission,[70–72] Copyright 2016, Nature Publishing group. Reproduced with permission,[73] Copyright 2017, Nature Publishing group. Reproduced with permission,[74] Copyright 2018, Nature Publishing group. Reproduced with permission,[75,76] Copyright 2019, Nature Publishing group. Reproduced with permission,[77] Copyright 2019, Elsevier.

forward by Croguennec and his co-workers 7 years later.[89–91] In 2013–2014, Dr McCalla in Dahn's group mapped out the pseudo-ternary phase diagrams of Li–Co–Mn–O and Li–Ni–Mn–O oxides, which contributed both to the synthesis of desired LMROs and to a stop of the spirited debates on the original structures of LMROs.[67,92]

Although the redox competition between cations and anions had been identified in a variety of electrodes in LIBs,[47,93,94] such as MX_2 (X = S, Se, *etc.*),[95–97] $LiCoO_2$,[98] $LiNi_{1/3}Co_{1/3}Mn_{1/3}O_2$,[99,100] *etc.*, the earliest hypothesis of the anionic redox in LROs came late.[101] In 2009, Koyama *et al.*[101] calculated the

electronic structure of $Li_{2-x}MnO_3$ (x = 2, 1.5, 1 and 0.5) by density functional theory (DFT) calculations and proposed that the Mn^{4+} ions remain stable and the oxidation of lattice oxygen contributes to the charge compensation during the extraction of the Li^+ ions. In 2012, the DFT calculations performed by Xiao *et al.*[102] also indicated that part of the charge compensation of $Li_{2-x}MnO_3$ is provided by the oxidation of lattice oxygen and the O_2 release that takes place when $x > 0.5$. This is therefore very critical for the practical application of LROs due to the poor stability of their structures. In 2013, Koga *et al.*[89] investigated the valence and structural changes of various transition metal ions in $Li_{1.20}Mn_{0.54}Co_{0.13}Ni_{0.13}O_2$ during cycling, and their results suggested the existence of a reversible lattice oxygen reaction. Moreover, they further studied the structural evolution of $Li_{1.20}Mn_{0.54}Co_{0.13}Ni_{0.13}O_2$ by XRD and proposed the 'two-phase' model accordingly.[90] Specifically, the oxygen loss mainly occurs on the surface of the particle and results in a densified phase near the surface due to TM migration, while the bulk of the particle maintains the original structure and undergoes reversible oxygen reactions. In the same year, Tarascon and his co-workers unveiled the reversible oxygen redox reactions in LROs experimentally by investigating the charge compensation mechanism in $Li_2Ru_{1-y}Sn_yO_2$.[68]

As a consequence, the above works have led to recent progress in the development of materials chemistry,[103–107] theories,[69–71,75,76,108] and advanced characterization techniques[109–111] for exploring anionic redox mechanisms in LROs and sodium transition metal oxides,[72,74,77,112,113] as summarized in Fig. 2. All recent milestones will be further discussed in detail in the following sections.

2.2 Classification of LROs

Up to now, LROs can be classified into layered lithium-rich oxides (LLROs) and cation disordered lithium-rich oxides (DLROs). Generally, LLROs exhibit much better cycling stability and higher average working potential, while DLROs show higher specific capacity. Li_2MnO_3 ($Li[Li_{1/3}Mn_{2/3}]O_2$) is one of the most typical LLROs with the space group of $C2/m$ (Fig. 3a)[114] and has a similar layered structure to those of O3-type LCO and NCM oxides (space group: $R\bar{3}m$). The excess Li atoms in the Mn layers tend to form $LiMn_6$ honeycomb structure ($LiMn_2$ planes) and result in the $\sqrt{3} \times \sqrt{3} - R30°$ ordering due to the charge difference between Li^+ and Mn^{4+}.[115] Therefore, along one of the three specific crystal orientations (*i.e.* $[100]_{C2/m}$, $[110]_{C2/m}$, and $[1\bar{1}0]_{C2/m}$),[116] the atomic columns exhibit Mn–Mn–Li ordering (Fig. 3b) with each column only containing either the Li or Mn atom. From aberration-corrected high-angle annular dark-field scanning transmission electron microscopy (HAADF-STEM) results, it is found that the contrast is approximately proportional

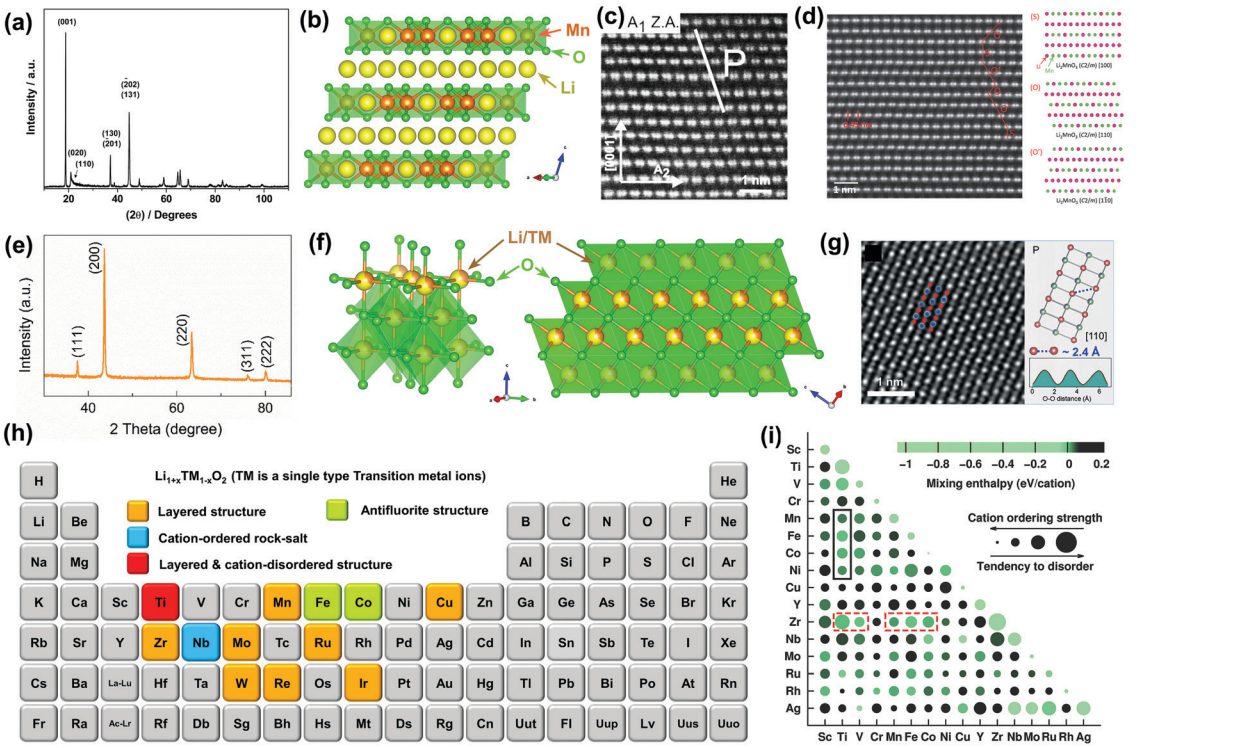

Fig. 3 Classification of LROs. (a) XRD pattern,[114] (b) schematic illustration and (c[117] and d[116]) HAADF-STEM images of Li_2MnO_3. (e) XRD pattern,[122] (f) schematic illustration, and (g) HAADF-STEM image[122] of DLROs. (h) TMs in the periodic system that are utilized in parent hosts for LROs. (i) Structural prediction of $LiA_{0.5}B_{0.5}O_2$ based on Monte-Carlo simulations, the green color suggests structural stability, the darker color means the less stable material; the size of the circle indicates the cation order tendency, the bigger the more the cation disorder tendency.[123] Reproduced with permission,[114] Copyright 2012, Elsevier. Reproduced with permission,[117] Copyright 2010, Wiley-VCH. Reproduced with permission,[116] Copyright 2015, The Ceramic Society of Japan. Reproduced with permission,[122] Copyright 2019, Wiley-VCH. Reproduced with permission,[123] Copyright 2016, Wiley-VCH.

to $Z^{1.7}$ (Z is the relative atomic number.). As a result, the bright–bright–dark ordering dots can be clearly observed in the HAADF-STEM images of Li_2MnO_3 (Fig. 3c).[117] It should be pointed out that the $LiMn_2$ planes can easily rotate 120° along the $[001]_{C2/m}$ zone axis and result in high densities of stacking faults (Fig. 3d).[116] The above features provide the basis for distinguishing the nature of the pristine structures of LMROs.[118] The structures of some layered Li-rich oxides may be different to that of Li_2MnO_3, For example, the Mo_3 triangle and Li^+ distributed randomly in the TM layers of Li_2MoO_3,[119,120] but most layered oxides, such as Li_2RuO_3 and Li_2IrO_3, are iso-structural to Li_2MnO_3 and LMROs. In regard to the DLROs, they also have the rock-salt structure (space group: $Fm\bar{3}m$, Fig. 3e) as compared to the LLROs.[121,122] The difference is that all cations of pristine DLROs are randomly distributed in oxygen octahedral sites, as shown in the illustration in Fig. 3f and the HAADF-STEM image in Fig. 3g.[122] Consequently, significant differences exist in their redox activities and phase transformations between LLROs and DLROs due to their distinct structural features, which will be reviewed in the following sections.

A variety of Li_2TMO_3 (TM = Zr *etc.*) compounds[124] have been studied since the 1980s due to their potential applications as Li^+ ion conductors. Recently, inspired by their possible anionic redox reactivity and high capacity, the fervor for these compounds has come back, because of the concept of applying them as electrode materials.[50] Moreover, by partially substituting the Li and TM elements in Li_2TMO_3 (TM = Mn,[42] Ti,[58,125] Zr,[124,125] Ir,[126] Ru,[127–129] *etc.*), Li_3TMO_4 (TM = Ir,[130] Nb[105] *etc.*) and Li_4TMO_5 (TM = Mo,[131,132] W,[132] *etc.*), and Li_5TMO_6 (TM = Re[133]) oxides, a great number of new materials with high capacity have been designed and synthesized which provide the possibility of resolving the challenges of LROs. Transition metals that are utilized in the parent hosts of different LROs are presented in Fig. 3h and the characteristic examples of previously reported LROs, including their structures, initial discharge capacities, cycling stabilities, and redox centers are summarized in Table 1. As we can see, several LROs, like layered $LiRu_{1-x}Ni_xO_2$, disordered $Li_4Mn_2O_5$, *etc.* exhibit a high capacity of over 300 mA h g^{-1},[134–136] but their cycling stabilities are still far from satisfactory. Therefore, further works are needed to unravel the underlying degradation mechanisms involved in cycling. To complete the library and accelerate the development of cation disordered oxides, Ceder's group proposed a computational methodology (Monte-Carlo simulation) to identify layered and cation-disordered oxides based on ternary oxides with the formula unit $LiA_{0.5}B_{0.5}O_2$,[123] and the result is presented in Fig. 3i. The brighter color and smaller circle suggest that the structure is more stable and the cations are more ordered. For example, $LiMn_{0.5}Ni_{0.5}O_2$ tends to adopt a low-energy cation ordering structure, in good agreement with experimental results. Although no obvious regularities could be obtained from their results, this method might pave the way for predicting the pristine structures of LROs.

2.3 Pristine structures of LMROs

In this review, LMROs refer to layered lithium-rich Mn-rich oxides with the chemical compositions of $Li[Li_xNi_yCo_zMn_{1-x-y-z}]O_2$. LMROs have been considered to be the most promising LROs, due to their relatively low cost, high average working potential, and better cycling stability, as compared to their cation disordered counterparts. Although the structure-evolution and charge-compensation mechanisms of LMROs have been investigated for over two decades, they are still under considerable debate to describe their pristine structures as either a two-phase nano-domain ($xLi_2MnO_3\cdot(1-x)LiNi_xCo_yMn_zO_2$) or a single-phase solid solution ($Li_{1+x}Ni_yCo_zMn_{1-x-y-z}O_2$). Because of the same rock-salt structure and similar layer spacings of Li/TM-layers, the crystal structures of monoclinic Li_2MnO_3 ($C2/m$) and trigonal $LiNi_xCo_yMn_zO_2$ ($R\bar{3}m$) are highly compatible, thus providing the foundation for both the nano-domain and solid-solution structures.

X-ray diffraction (XRD) is incapable of discriminating the nano-domain and solid-solution structures. As shown in the XRD patterns of $Li_{1.2}Ni_{0.2}Mn_{0.6}O_2$ (Fig. 4a), all diffraction peaks can be indexed to a monoclinic ($C2/m$) phase. Meanwhile, they can also be indexed to the trigonal ($R\bar{3}m$) structure, except for superlattice peaks located between 20° and30°.[160] One of the earliest solid-solution structures has been reported in $Li[Li_{x/3}Mn_{2x/3}Co_{1-x}]O_2$ by Numata *et al.*,[161] due to the similar structure between $LiCoO_2$ and Li_2MnO_3. In 2001, Lu *et al.* found that the lattice constants, *i.e.* a, c, and the c/a ratio, of $Li_{1+x}Ni_{1/3-2x/3}Mn_{2/3-x/3}O_2$ samples vary smoothly with the Li content (x), suggesting the character of the solid-solution structure of $Li_{1+x}Ni_{1/3-2x/3}Mn_{2/3-x/3}O_2$.[42] However, in 2004, although a similar phenomenon was observed in the $xLi_2TiO_3\cdot(1-x)$-$LiNi_{0.5}Mn_{0.5}O_2$ series,[125] ^{6}Li magic angle spinning (MAS) solid-state nuclear magnetic resonance (ss-NMR) data suggest that the Li_2TiO_3 domains exist in the $xLi_2TiO_3\cdot(1-x)LiNi_{0.5}$-$Mn_{0.5}O_2$ samples, providing the first evidence for the concept of a two-phase nanodomain.[125] In the same year, Grey's group revealed the short-range ordering of $Li(OMn)_6$ in $Li[Li_{(1-2x)/3}$-$Ni_xMn_{(2-x)/3}]O_2$ electrodes by the ss-NMR technique.[162] As shown in Fig. 4b, Li resonances can be classified into two kinds of signals, *e.g.* Li^+ in the Li layers (~700 ppm) and in the TM layers (~1400 ppm). For the latter, the resonances located at 1560, 1365 and 1150 ppm correspond to the Li^+ located in the $Li(OMn)_6$, $Li(OMn)_5(ONi)$ and $Li(OMn)_4(ONi)_2$ environments, respectively. A stronger resonance at 1560 ppm than at 1365 ppm suggests that the Li^+ ions in the TM layers prefer to be surrounded by Mn^{4+} rather than Ni^{2+} ions.[162] In 2005, based on electron diffraction (ED) and synchrotron XRD analysis, Meng *et al.*[163] proposed the in-plane $\sqrt{3}\boldsymbol{a}_{hex.}\times\sqrt{3}\boldsymbol{a}_{hex.}$ ordering model with a particular occupancy of Li^+, Ni^{2+}, and Mn^{4+} ions in the TM layers for $Li[Ni_xLi_{1/3-2x/3}Mn_{2/3-x/3}]O_2$. Combined with ss-NMR results,[162] these two papers provided clues for the exploration of sublattice structures at the TM layers of $Li_{1+x}Ni_{1/3-2x/3}Mn_{2/3-x/3}O_2$ oxides. The cation ordering phenomenon was also observed by Raman spectroscopy. As shown in Fig. 4c, Koga *et al.*[164] found that the Raman spectrum of $Li_{1.2}Mn_{0.54}Ni_{0.13}Co_{0.13}O_2$ is not a simple combination of Li_2MnO_3 and $LiMn_{1/3}Ni_{1/3}Co_{1/3}O_2$ domains, but has extended cation ordering within the *TM* layers along the c axis.

ND is an ideal technique to gain insights into the initial structures of LROs, owing to its distinctive advantages, such as

Table 1 Characteristics of Li-rich oxides. (Note: if it is not specified, the cycling performance was investigated at the same voltage range/current densities with the discharge capacity; pre-lithiation additives are marked with "a".)

Materials	Structures	1st dis-capacity (mA h g^{-1})	Cycle performance		
		Capacity (current density, voltage range)	Capacity retention	Redox center	Year
		Li-rich 3d oxides			
$Li[Cr_{1/6}Li_{5/18}Mn_{5/9}]O_2$	Layered	230 (5 mA g^{-1}, 2.0–4.8 V)	—	Cr, O	2002[80]
Li_2CuO_2[a]	Layered (*Immm*)	240 (C/16, 1.8–4.5 V)	—	Cu	2003[137]
$Li_{1.9}Cr_{0.3}Mn_{0.8}O_3$	Layered	250 (11.98 mA g^{-1}, 2.0–4.8 V)	—	—	2008[138]
Li_2MnO_3	Layered (*C*2/*m*)	200 (C/10, 2–5 V)	54%, 33 cycles	Mn, O	2014[139]
$Li_{1.2}Fe_{0.4}Ti_{0.4}O_2$	Disordered	~130 (C/60, 2.2–4.5 V)	—	Fe, O	2015[106]
Li_6CoO_4[a]	Antifluorite (*P*42/*nmc*)	—	—	Co, O	2015[140]
$Li_{1.2}Ni_{0.2}Mn_{0.6}O_2$	Layered	240 (C/10, 2.0–4.8 V)	100%, 100 cycles	Ni, O	2015[141]
Li_2VO_2F	Disordered	~420 (C/60, 1.2–4.2 V)	~70%, C/5, 20 cycles	V	2015[142]
$Li_{1.144}Ni_{0.136}Mn_{0.544}Co_{0.136}O_2$	Layered	301 (25 mA g^{-1}, 2.0–4.8 V)	99%, 125 mA g^{-1}, 100 cycles	Mn, Ni, Co, O	2016[143]
$Li_4Mn_2O_5$	Disordered	355 (C/20, 1.2–4.8 V)	—	Mn, O	2016[144]
Li_5FeO_4[a]	Antifluorite (*Pbca*)	—	—	Fe, O	2017[145,146]
$Li_2Mn_{0.95}O_{2.05}F_{0.95}$	Disordered	~275 (C/10, 2.0–4.8 V)	~60%, 50 cycles	Mn, O	2018[134]
		Li-Rich 4d 5d oxides			
Li_2SnO_3	Layered (*C*2/*c*)	—	—	—	1982[124]
Li_2ZrO_3	Layered (*C*2/*c*)	—	—	—	1982[124]
Li_4MoO_5	Layered	—	—	—	1989[132]
Li_4WO_5	Layered	—	—	—	1989[132]
$Li_2Ru_{1-y}Mn_yO_2$	Layered (*C*2/*c* or *C*2/*m*)	250 (0.2C, 2.0–4.6 V)	84%, 40 cycles	Ru, Mn, O	2013[129]
Li_4NiTeO_6	Layered (*C*2/*m*)	~110 (2–5 V)	90%, 100 cycles	Ni	2013[147]
$Li_{1.211}Mo_{0.467}Cr_{0.3}O_2$	Layered	~280 (C/20, 1.5–4.3 V)	—	—	2014[69]
$Li_2Ru_{0.75}Ti_{0.25}O_2$	Layered (*C*2/*m*)	~240 (0.2C, 2.0–4.6 V)	62%, 100 cycles, 2.0–4.6 V	Ru, Ti, O	2015[128]
$Li_2Ru_{0.75}Ti_{0.25}O_2$	Layered (*C*2/*m*)	100 (0.2C, 2.0–3.8 V)	100%, 80 cycles, 2.0–3.8 V	Ru, Ti	2015[128]
$Li_2Ru_{0.75}Sn_{0.25}O_2$	Layered (*C*2/*m*)	~225 (0.2C, 2.0–4.6 V)	85%, 100 cycles, 2.0–4.6 V	Ru, O	2015[128]
$Li_2Ru_{0.75}Sn_{0.25}O_2$	Layered (*C*2/*m*)	~115 (0.2C, 2.0–4.0 V)	100%, 80 cycles, 2.0–4.0 V	Ru	2015[128]
$Li_{4.27}Fe_{0.56}TeO_6$	Layered (*C*2/*m*)	~174 (C/50, 2.0–4.6 V)	—	O	2015[148]
Li_4FeSbO_6	Layered (*C*2/*m*)[149]	~220 (0.05C, 2.0–5.0 V)	Poor	Fe, O	2015[150]
Li_2IrO_3	Layered	~161 (C/10, 2.5–4.6)	—	Ir, O	2015[108]
$Li_{1/2}Ni_{1/3}Ti_{1/3}Mo_{2/15}O_2$	Disordered	225 (20 mA g^{-1}, 1.5–4.5 V)	75%, 20 cycles	Ni, O	2015[151]
$Li_{1.3}Nb_{0.3}Mn_{0.4}O_2$	Disordered	~250 (10 mA g^{-1}, 1.5–4.8 V)	—	Mn, O	2015[105]
$Li_{1.3}Nb_{0.3}Fe_{0.4}O_2$	Disordered	~250 (10 mA g^{-1}, 1.5–4.8 V)	—	—	2015[105]
$Li_{1.3}Nb_{0.43}Co_{0.27}O_2$	Disordered	~300 (10 mA g^{-1}, 1.5–4.8 V)	—	—	2015[105]
$Li_{1.3}Nb_{0.43}Ni_{0.27}O_2$	Disordered	~275 (10 mA g^{-1}, 1.5–4.8 V)	—	—	2015[105]
$Li_{1.3}Nb_{0.3}Mn_{0.4}O_2$	Disordered	~240 (10 mA g^{-1}, 1.5–4.8 V, 50 °C)	—	Mn, O	2016[152]
$Li_{1.3}Nb_{0.3}V_{0.4}O_2$	Disordered	~190 (10 mA g^{-1}, 1.5–4.8 V, 50 °C)	—	V	2016[152]
$Li_{1.42}Fe_{0.92}Mo_{0.29}O_2$	Layered (*C*2/*m*)	205 (20 mA g^{-1}, 1.5–4.8 V)	Poor	—	2016[153]
Li_4NiMoO_6	Layered (*C*2/*m*)	~220 (10 mA g^{-1}, 1.5–4.5 V)	Poor	—	2016[131]
Li_5ReO_6[a]	Layered	—	—	O	2016[133]
β-Li_2IrO_3	3D ordered	~190 (2.0–4.8)	~85%, 30 cycles	Ir, O	2017[126]
Li_3IrO_4	Layered	340 (C/10, 1.5–4 V)	—	Ir, O	2017[130]
Li_3NbO_4	$I\bar{4}3m$	Inactive	—	—	2017[49]
$Li_{4/3}Mo_{2/3}O_2$	Disordered	320 (10 mA g^{-1}, 1–4.4 V)	—	Mo	2017[135]
$Li_{9/7}Nb_{2/7}Mo_{3/7}O_2$	Disordered	280 (10 mA g^{-1}, 1–4.4 V)	—	Mo	2017[135]
$Li_{6/5}Ti_{2/5}Mo_{2/5}O_2$	Disordered	270 (10 mA g^{-1}, 1–4.4 V)	—	Mo	2017[135]
$Li_2Mn_{2/3}Nb_{1/3}O_2F$	Disordered	277 (20 mA g^{-1}, 1.5–4.8 V)	~75%, 25 cycles	Mn, O	2018[154]
$Li_{4.15}Ni_{0.85}WO_6$	Layered	~200 (1–5 V)	~80%, 10 cycles	Ni, O	2019[155]
$Li_{1.3}Ta_{0.3}Mn_{0.4}O_2$	Disordered	250 (10 mA g^{-1}, 1.5–4.8 V)	—	Mn, O	2019[156]
$LiRu_{1-x}Ni_xO_2$	Disordered	410 (50 mA g^{-1}, 1.35–4.6 V)	—	Ru, Ni, O	2019[136]
$Li_{1.2}Ni_{0.2}Ru_{0.6}O_2$	Layered	214 (5 mA g^{-1}, 2.0–4.8 V)	86%, 25 cycles	Ni, Ru	2019[157]
Li_2RuO_3	Layered (*C*2/*c*)	270	—	Ru, O	2019[158]
$Li_{1.2}Ti_{0.35}Ni_{0.35}Nb_{0.1}O_{1.8}F_{0.2}$	Disordered	277 (20 mA g^{-1}, 1.5–4.8 V)	—	Ni, O	2019[122]
$Li_{1.2}Mn_{0.4+x}Ti_{0.4-x}O_2$	Disordered	322 (30 mA g^{-1}, 1.5–4.8 V)	80%, 50 cycles, 300 mA g^{-1}	Mn, O	2020[159]

the high sensitivity of neutrons to light elements (Li, O, *etc.*) and the large scattering contrast between neighboring TM elements (*e.g.*, Ni, Co, and Mn).[166] However, from the ND Rietveld refinement results of the $Li_{1.2}Mn_{0.54}Ni_{0.13}Co_{0.13}O_2$ sample, Koga *et al.* obtained the same reliability factors (R_{wp} = 11.6%) based on the *C*2/*m* and $R\bar{3}m$ structures.[164] Moreover, Mohanty *et al.*[167] experienced the same, *i.e.*, they obtained an R_{wp} value of 5.05% based on both single-phase ($R\bar{3}m$) and two-phase (*C*2/*m* + $R\bar{3}m$) models, when carrying out the ND Rietveld refinement. These results come to a consensus of the existence of local structural and cation ordering at the TM layers. However, spectroscopic techniques such as XRD,

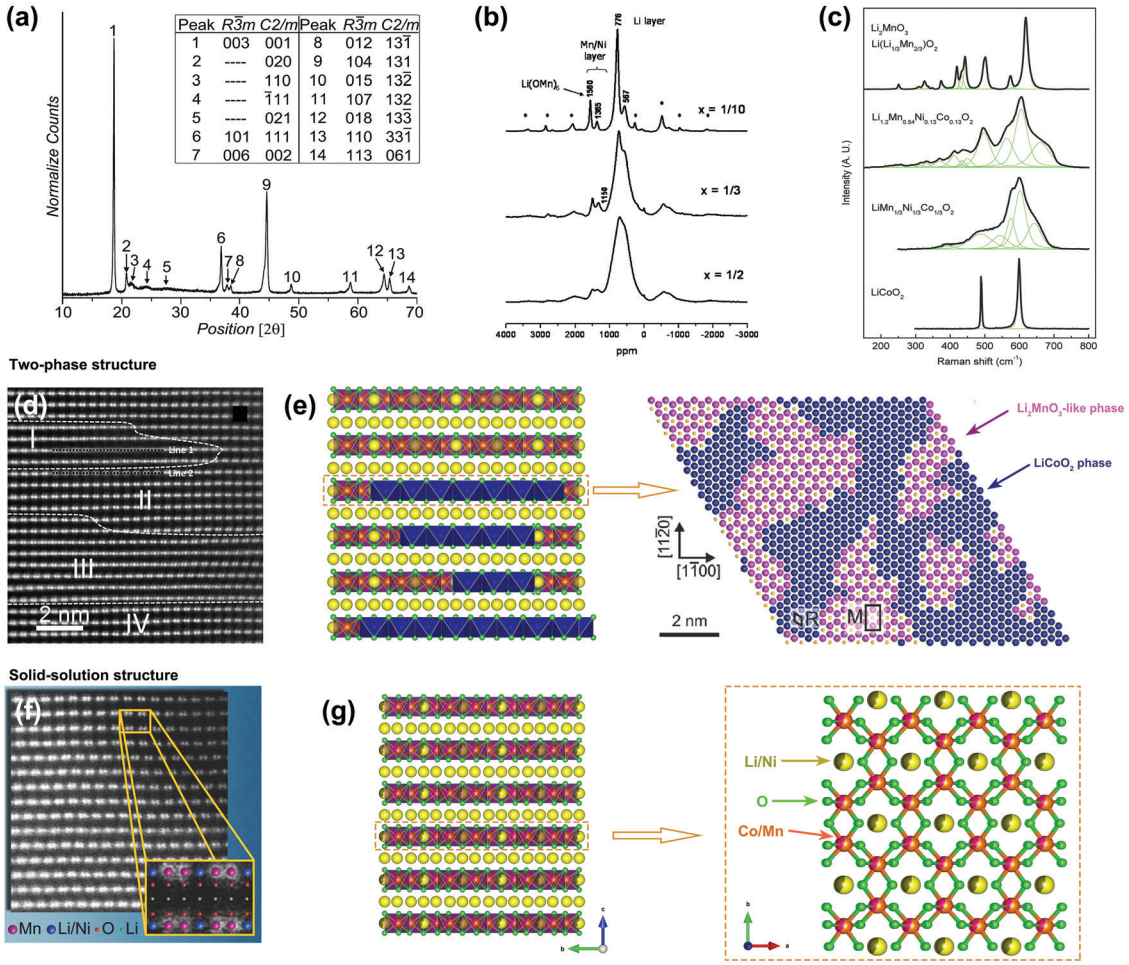

Fig. 4 Pristine structure of LLROs. (a) XRD pattern of $Li_{1.2}Ni_{0.2}Mn_{0.6}O_2$.[160] (b) ^{6}Li ss-NMR spectra of $Li[Li_{(1-2x)/3}Ni_xMn_{(2-x)/3}]O_2$ samples.[162] (c) Comparison of Raman spectra among $Li_{1.2}Mn_{0.54}Ni_{0.13}Co_{0.13}O_2$, Li_2MnO_3, $LiMn_{1/3}Ni_{1/3}Co_{1/3}O_2$, and $LiCoO_2$.[164] (d) HAADF-STEM image[118] and (e) schematic illustration[165] of the two-phase nanodomain structure. (f) HAADF-STEM image[160] and (g) schematic illustration of the one-phase solid-solution structure. Reproduced with permission,[160,165] Copyright 2011, American Chemical Society. Reproduced with permission,[162] Copyright 2004, IOP Publishing. Reproduced with permission,[164] Copyright 2012, American Chemical Society. Reproduced with permission,[118] Copyright 2014, Wiley-VCH.

Raman, NMR, and ND could not give a clear and satisfactory answer to the debate between the solid-solution or nanodomain structures.

STEM is an effective technique to observe the local cation arrangement of LMROs. Along three specific directions of $[100]_{C2/m}$, $[110]_{C2/m}$ and $[1\bar{1}0]_{C2/m}$, the ordered Li–TM–TM arrangement (dark-bright-bright dots in HAADF-STEM images) within the TM layers corresponds to the Li_2MnO_3-like (lithium-rich) phase, while the continuous bright dots are associated with the NCM structure.[116] Besides, the selected area electron diffraction (SAED) patterns of Li_2MnO_3-like and NCM structures differ greatly, as clarified in previous articles.[160,168,169] Therefore, the STEM and SAED techniques could give direct evidence to close this debate. The atomic-scale observation of a two-phase structure in pristine $Li_{1.2}Mn_{0.567}Ni_{0.166}Co_{0.067}O_2$ was reported in 2013 by Zhou's group.[169] Yu *et al.*[118] also confirmed the two-phase structure of $Li_{1.2}Ni_{0.15}Co_{0.1}Mn_{0.55}O_2$ by HAADF-STEM. As shown in Fig. 4d, the dot–dot-black contrast areas (II and IV) and continuous-dots-contrast areas (I and III) correspond to the lithium-rich and NCM phases, respectively. The sizes of these nanodomains are 2–4 nm. The two-phase nanodomain structure seems to prevail in materials with high Co content, such as $Li_{1.2}Co_{0.4}Mn_{0.4}O_2$. Based on the combination of XRD, extended X-ray absorption fine structure (EXAFS), SAED, and HAADF-STEM results, Bareno *et al.*[165] found that Mn^{4+} and Co^{3+} ions in the $Li_{1.2}Co_{0.4}Mn_{0.4}O_2$ material tend to be located in Li_2MnO_3-like and $LiCoO_2$-like local environments, respectively, with length scales of $\geq$2–3 nm for each domain, as shown in Fig. 4e.

The earliest direct evidence for the solid-solution structures of LMROs might be the HAADF-STEM image of $Li_{1.2}Ni_{0.17}Co_{0.07}Mn_{0.56}O_2$ obtained by Ohsawa's group in 2010.[170] It shows a clear one-phase structure with high concentration of stacking faults. Then, the HAADF-STEM images and SAED analysis reported by Jarvis *et al.*,[160] Gu *et al.*,[171] and Genevois *et al.*[168] uncovered the one-phase solid-solution feature of LMROs. As shown in Fig. 4f, the HAADF-STEM image[160] reveals a homogeneous Li_2MnO_3-like structure with Li^+ and Ni^{2+} being located at the Li site in

the TM layers. Based on the results obtained from studies on the $Li_{1.2}(Ni_{0.13}Mn_{0.54}Co_{0.13})O_2$ material[172] and a series of LMROs with different Li/TM ratios[173] (*i.e.* $Li_{1.15}Ni_{0.1748}Mn_{0.496}Co_{0.18}O_2$, $Li_{1.1}Ni_{0.227}Mn_{0.438}Co_{0.235}O_2$, and $Li_{1.079}Ni_{0.248}Mn_{0.411}Co_{0.263}O_2$), Shukla *et al.* demonstrated that pristine LMROs do not have a two-phase structure that consists of Li_2MnO_3-like and NCM-like nanodomains. Importantly, similar to the model proposed by Boulineau *et al.*,[174] Shukla *et al.*[173] further proposed that faint reflections and streaks in SAED patterns originated from the massive stacking faults rather than the long-range $\sqrt{3}\boldsymbol{a}_{hex.} \times \sqrt{3}\boldsymbol{a}_{hex.}$ cation ordering. Long-range ordering *vs.* stacking faults will be another tricky problem that needs to be resolved in the near future.

The above discussions clearly demonstrate the complicated structures of pristine LMROs. Ideally, as shown in Fig. 4g, high-valence cations (Co^{3+} and Mn^{4+}) and low-valence cations (Li^+ and Ni^{2+}) tend to be located at the Mn^{4+} and Li^+ sites in the TM layers of the Li_2MnO_3-like structure, respectively. This cation ordered structure might be able to optimize the charge distribution and to minimize the structural strains.[164] Therefore, it is more favorable to form a perfect honeycomb structure if the atomic ratio of high-valence cations and low-valence cations on the TM layer is 2 : 1.[175] Moreover, other parameters, especially synthesis methods,[168,176] annealing temperature,[90,164] and TM types,[125] are equally, if not more, important than stoichiometry,[67,168,175] to determine the pristine structures of LLROs.

3. The reaction mechanisms of LROs

3.1 Products of lattice oxygen oxidation

It has been widely accepted so far that oxygen redox reactions are responsible for the excess capacity beyond cation redox in LROs. However, the corresponding detailed mechanisms have been debated in the literature, especially the formation of the products of lattice oxygen oxidation.

In 2013, by using $Li_2Ru_{1-y}Sn_yO_3$ as model materials, Tarascon's group[68] confirmed the existence of lattice oxygen redox reactions in LROs. As shown in the X-ray photoelectron spectroscopy (XPS) spectra of $Li_2Ru_{1-y}Sn_yO_3$ electrodes at different charge/discharge states (Fig. 5a), a new peak located at ~530.5 eV appeared in the curve of the one being charged to 4.6 V, which was identified to be the O_2^{2-} species or to under-coordinated oxygen species originating from the oxidation of lattice oxygen. Besides, electron paramagnetic resonance (EPR, Fig. 5a) spectroscopy and DFT calculations have been conducted to confirm the existence of peroxo/superoxo-like

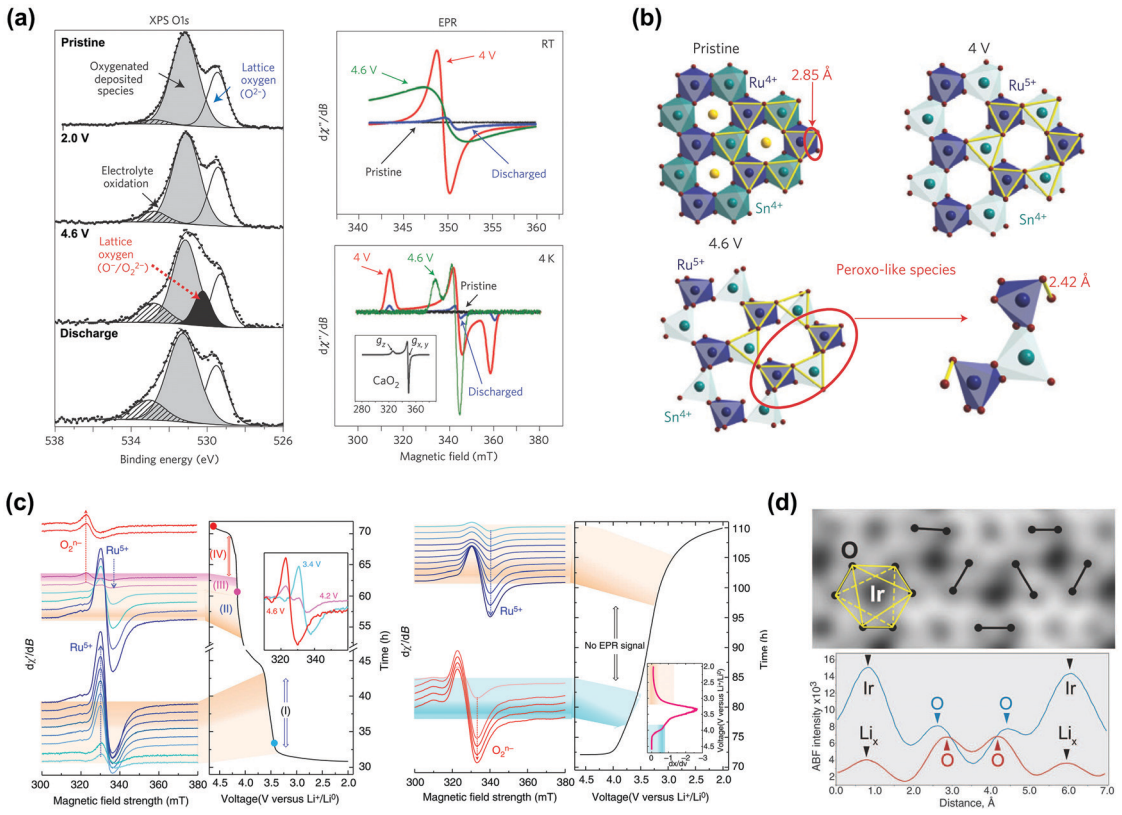

Fig. 5 Products of lattice oxygen oxidation reactions in LROs (I). (a) O 1s XPS and X-band EPR spectra of $Li_2Ru_{0.5}Sn_{0.5}O_3$ recorded at different charge/discharge states.[68] (b) Schematic illustration of peroxo-like species in the charged $Li_2Ru_{0.5}Sn_{0.5}O_3$.[68] (c) X-band EPR spectra of the $Li_2Ru_{0.75}Sn_{0.25}O_3$ electrodes during charge and discharge processes.[110] (d) ABS-STEM image of the $Li_{0.5}IrO_3$ sample showing O–O pairs with short projected distances.[108] Reproduced with permission,[68] Copyright 2013, Nature Publishing group. Reproduced with permission,[110] Copyright 2015, Nature Publishing group. Reproduced with permission,[108] Copyright 2015, AAAS.

species. They further proposed that Sn^{4+} can improve the flexibility of the TM–O bond (Fig. 5b), thus minimizing oxygen release and improving the reversibility of oxygen redox reactions. Since then, XPS has been widely used to confirm the lattice oxygen redox reactions.[128,177,178] However, the identification of oxygen redox by only XPS is not very convincing, since it is a surface-sensitive technique with a probe depth of only 5–10 nm for oxides. In 2015, Tarascon's group[110] utilized an *operando* EPR technique to investigate oxygen redox reactions in $Li_2Ru_{0.75}Sn_{0.25}O_2$ and proved the formation of reversible O_2^{n-} species (Fig. 5c). In the same year, the O–O dimers (shortened O–O bonds) were visualized first by annular bright field STEM (ABF-STEM) in the charged Li_2IrO_3 electrode, as shown in Fig. 5d.[108] The observed bond length of the O–O dimer arising from the oxidation of lattice oxygen is ~2.5 Å, which is much longer than that in Li_2O_2 (1.5 Å), and thus it was named "peroxo-like" species in this work. In 2016, Saubanère *et al.*[104] compared the stability of O_2^{n-} species in Li_2RuO_3 and Li_2MnO_3 and found that the covalency between TM and oxygen makes a great difference to the stability of oxidized oxygen species. Specifically, O_2^{n-} species in the charged Li_2RuO_3 are much stable than those in Li_2MnO_3 due to the higher covalency of Ru–O as opposed to the Mn–O bond. In conclusion, Tarascon and his co-workers believed that the peroxo/superoxo-like species does exist as the products of lattice oxygen reactions as they observed in the 4d- and 5d-TM based LROs. These O_2^{n-} species have also been identified by X-ray absorption spectroscopy (XAS) characterization in LMROs by some researchers.[179,180]

For example, Oishi *et al.*[180] studied the reversibility of oxygen redox reactions in Li_2MnO_3 by using O K-edge and Mn L-edge XAS. They compared the difference between O K-edge spectra at the pristine and voltage plateau states (4.5 V), and the difference between O K-edge spectra at the pristine and 4.8 V charged states. The result revealed that enhanced peaks in both total electron yield (TEY) and partial fluorescence yield (PFY) modes have similar shapes and locations to Li_2O_2 and KO_2 references, and the peroxide and superoxide species were therefore proposed as the products of lattice oxygen oxidation during the charge process of Li_2MnO_3.[180]

However, other researchers suggest that the nature of the oxidized O^{2-} product in LMROs is O^-/O^{n-} (the oxygen ions with electron holes) rather than the true O_2^{2-} (O–O 1.45 Å) species. In 2016, by combining XAS and isotope DEMS, Bruce's group[70] showed that electron–hole states on O atoms coordinated by Li^+/Mn^{4+} are formed in the charged $Li_{1.2}Ni_{0.13}Co_{0.13}Mn_{0.54}O_2$ electrode (Fig. 6a). Furthermore, the absence of O–O peroxo vibrations in their Raman spectra indicates that the true O_2^{2-} species are not formed in LMROs. O^-/O^{n-}, a product of oxygen redox reactions, has also been identified in the charged Co-free $Li[Li_{0.2}Ni_{0.2}Mn_{0.6}]O_2$ electrode.[181] Based on scanning transmission X-ray microscopy (STXM), XAS, and mapping of resonant inelastic X-ray scattering (mRIXS) results, Gent *et al.*[73] proposed that the lattice oxygen redox reaction is not a rigid O^{2-}/O^- redox couple, but more likely a dynamic process of $[O^{2-} + TM] \rightarrow [O^- + TM_{mig}] + e^-$. The reversibility of the bulk oxygen redox reaction after long-term cycling (500 cycles, Fig. 6b)

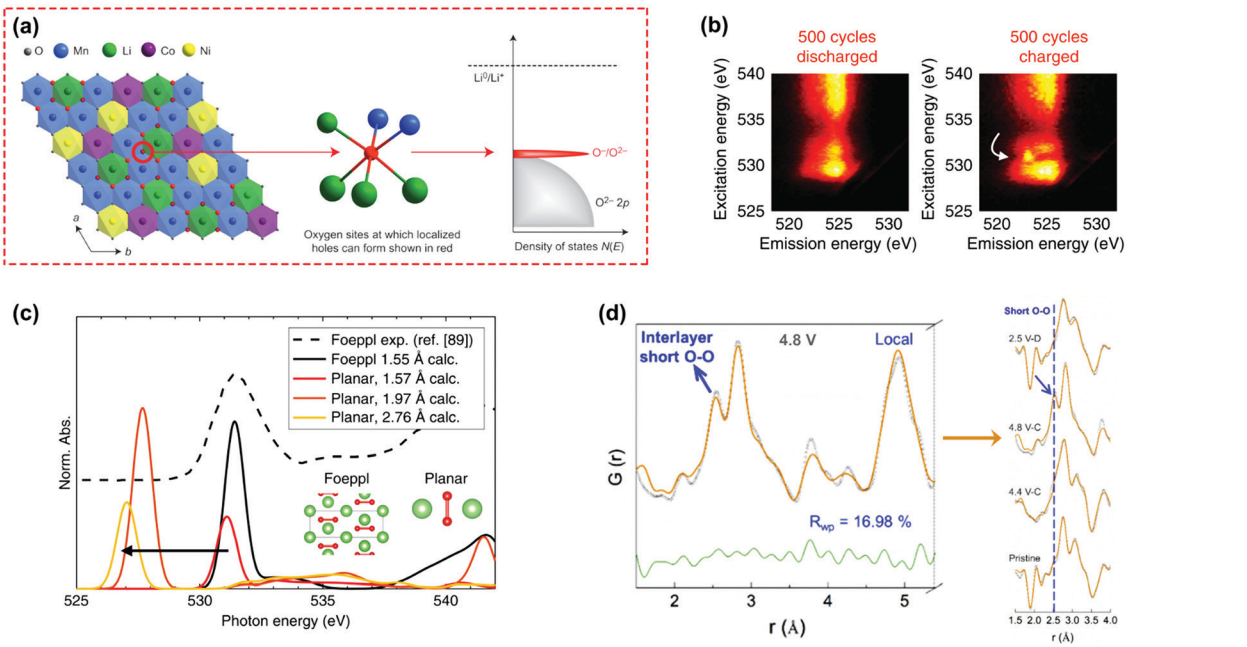

Fig. 6 Products of lattice oxygen oxidation reactions in LROs (II). (a) Schematic illustration of the O^-/O^{2-} redox couple in the $Li_{1.2}Ni_{0.13}Co_{0.13}Mn_{0.54}O_2$ material.[70] (b) mRIXS of $Li_{1.17}Ni_{0.21}Mn_{0.54}Co_{0.08}O_2$ at the 501st cycle at discharge and charge states. The contrasting feature indicated by a white arrow shows that oxygen redox is reversible even after 500 cycles.[73] (c) *Ab initio* XAS of Li_2O_2 as a function of various O–O bond lengths and the comparison with the experimental results.[73] (d) Comparison of *ex situ* nPDF results of $Li_{1.2}Ni_{0.13}Mn_{0.54}Co_{0.13}O_2$ collected at different charge/discharge states showing shortened O–O pairs upon lattice oxygen redox.[175] Reproduced with permission,[70] Copyright 2016, Nature Publishing group. Reproduced with permission,[73] Copyright 2017, Nature Publishing group. Reproduced with permission,[175] Copyright 2020, Elsevier.

in the $Li_{1.17}Ni_{0.21}Co_{0.08}Mn_{0.54}O_2$ electrode has been confirmed first in this work. Moreover, as shown in Fig. 6c, their *ab initio* calculations show that the XAS features at 530.8 eV cannot be assigned to the O–O dimers (O_2^{n-}), because the calculated O–O dimers residing at this energy have much shorter bond lengths of 1.55–1.57 Å than the observed ones (~1.9 Å and even higher).

Some researchers suggested that the actual oxygen redox products of O^-/O^{n-} or O_2^{2-}/O_2^{n-} (O–O dimer) species are conditionally dependent. In 2016, Ceder's group[71] proposed the unhybridized Li–O–Li configuration as the theoretical support for oxygen redox reactions in LROs. Their results revealed that the coalescence of electron holes to form peroxo-like species occurs when the oxygen is bonded to a lower amount of metal ions.[71] Islam and his co-worker[182] investigated the lithium extraction mechanisms in Li_2MnO_3 by *ab initio* simulations. The results indicated that the unstable localized holes on oxygen (O^-) are formed at the beginning of delithiation, then transformed into peroxo or superoxide species and furthermore into O_2 gas with the continual lithium extraction. Therefore, they proposed that preventing oxygen dimerization is a key factor in stabilizing the O^- species and improving the reversibility of anionic redox reactions.

In recent years, the emergence of novel spectroscopic techniques has provided new insights into the oxygen redox reactions, such as *in situ* Raman[183,184] and pair distribution function (PDF) analysis.[122,175] Zhou's group[183] observed the peroxo O–O stretch in *in situ* Raman spectra during the charge and discharge processes of $Li_{1.2}Ni_{0.2}Mn_{0.6}O_2$ and the O–O bond length was calculated to be ~1.3 Å. A similar phenomenon was also observed in the study of the $Li_2Ni_{1/3}Ru_{2/3}O_3$ electrode.[184] Ceder's group[185] compared the electrochemical and structural behaviors between Li_2IrO_3 and $Li_2Ir_{1-y}Sn_yO_3$ by combining the bulk-sensitive spectroscopic probes (XAS and mRIXS) with first-principles calculations. They demonstrated that the formation of 1.4 Å O–O dimers requires the presence of neighboring cation vacancies. Zhao *et al.*[175] first observed the shortening of the O–O bond during lattice oxygen oxidation in $Li_{1.2}Ni_{0.13}Mn_{0.54}Co_{0.13}O_2$ by neutron pair distribution function analysis (nPDF). As displayed in Fig. 6d, the increase of the interlayer short O–O signal located at ~2.55 Å can be clearly observed during the charge process from 4.4 V to 4.8 V, which is similar to the peroxo-like O–O dimer formation (~2.45 Å) in 5d Li_2IrO_3[108] but much longer than the real peroxo bonds of ~1.5 Å. In contrast, the shortening of the O–O bond was not observed by STEM and nPDF in the cation disordered $Li_{1.2}Ti_{0.35}Ni_{0.35}Nb_{0.1}O_{1.8}F_{0.2}$,[122] even though lattice oxygen redox was recognized from the mRIXS image of the 4.8 V charged electrode. Nevertheless, the existence of O^- has been disputed by Radin *et al.*,[76] not only because the notion of the O^- ion is unprecedented, but also due to the lack of direct evidence. For example, the spectroscopic features regarded as the signature of O^{2-}/O^- redox can also be interpreted by other mechanisms, such as the formation of molecular O_2. This theoretical perspective strongly challenged the discussions based on RIXS spectroscopic results. Therefore, a reliable theoretical interpretation of the spectroscopic features reported in the literature, as well as more direct experimental evidence, is critical for identifying the products of lattice-oxygen oxidation reactions. At this time, the direct calculation to reproduce the mRIXS results remains missing, which is a grand challenge to the fundamental physics of the RIXS process, but holds the key to revealing the true fundamental nature or driving force of the oxygen redox reactions.

A critical aspect of the oxygen redox reaction is its extent and the nature of the resulting oxidized species. The shortening of the O–O bonds has been observed in charged 3d-, 4d- and 5d-based LROs and most of these bonds are longer than the peroxo O–O bonds in Li_2O_2.[68,108,175] The exact products of oxygen redox reactions in various lithium-rich materials and the boundary between the electron holes (O^-/O^{n-}) and O–O dimers (O_2^{2-}/O_2^{n-}) are still debatable. Although researchers have demonstrated the possibility of O–O dimer formation with a bond length of 1.3–1.4 Å in some LROs by DFT calculations[182,185] and the existence of peroxo/superoxide products was observed by the *in situ* Raman technique,[183] more solid experimental evidence for the O_2^{2-}/O_2^{n-} species in the bulk of electrodes is highly needed. *In situ* Raman is still unable to acquire a unified picture of the structure–performance relationship between the lattice oxygen redox reactions and electrochemical performance of LROs, due to the limitation of the accuracy and spatial resolution of the existing characterization techniques and due to the complexity of the LRO systems, such as differences in their structures (layer and cation disordered), TM species, stoichiometry, particle sizes, and the depth of the oxygen redox reactions (surface and bulk). With the fast development of the state-of-the-art characterization techniques, such as mRIXS, *in situ* Raman, PDF, STEM, ss-NMR, *etc.*, the above problems will be most probably clarified in the near future.

3.2 Oxygen vacancies

Oxygen loss and oxygen vacancies created by oxygen loss are the greatest challenges encountered by LROs.[66,70,186,187] As early as 2002, Dahn's group[79] proposed the irreversible oxygen loss in $Li[Ni_xLi_{(1/3-2x/3)}Mn_{(2/3-x/3)}]O_2$ at the activation plateau during the initial charge process, based on the Rietveld refinement of *in situ* XRD and differential capacity measurements. The first observation of O_2 release in LROs, from the DEMS measurement of the charged $Li_{1.2}Ni_{0.2}Mn_{0.6}O_2$ electrode (Fig. 7a), can be traced back to 2006 by Bruce's group.[66] It is apparent that O_2 loss and oxygen vacancies are closely related to each other and oxygen vacancies are therefore investigated by the structural and chemical analysis of LROs, with techniques such as *in situ*/*ex situ* XRD and O K-edge EELS.[188,189] In 2012, Okamoto[190] studied the influence of oxygen vacancies on Li extraction in Li_2MnO_3 by DFT calculations (Fig. 7b). His results suggested that with the increase in the content of oxygen vacancies, the redox potential of full-delithiated Li_2MnO_3 decreases and the contribution of Mn to the charge compensation with the lithium extraction increases. Besides, excess oxygen vacancies could lead to a sharp shrinking of the cell volume and damage the structure of Li_2MnO_3.[190] Based on the results of XRD, electron energy loss spectroscopy (EELS), and STEM characterization,

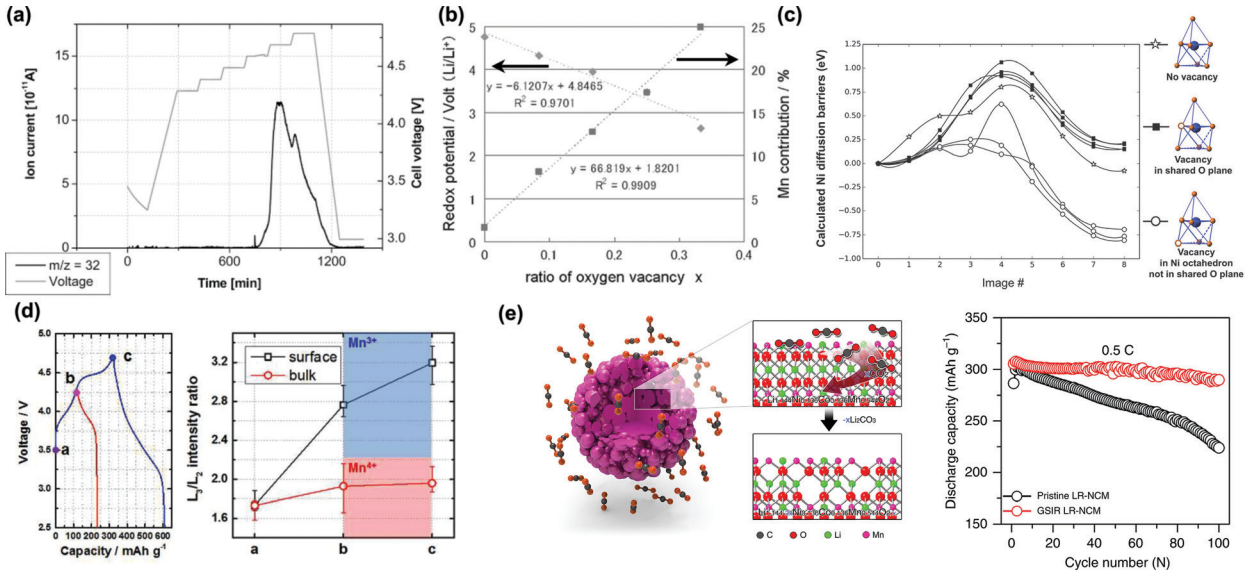

Fig. 7 Oxygen vacancies in LROs. (a) The first evidence of O_2 release from a charged $Li_{1.2}Ni_{0.2}Mn_{0.6}O_2$ electrode obtained by DEMS.[66] (b) DFT calculation results showing that the redox potential of Li_2MnO_3 decreases with an increase of oxygen vacancies.[190] (c) Calculated Ni diffusion barriers along with different locations of oxygen vacancies in $Li_{20/28}Ni_{1/4}Mn_{7/12}O_2$.[189] (d) Mn L_3/L_2 ratio from the EELS spectra of the bulk and surface of $0.4Li_2MnO_3{-}0.6LiNi_{1/3}Co_{1/3}Mn_{1/3}O_2$ samples at different charge states.[191] (e) Schematic of oxygen vacancies in the surface layer introduced by gas/solid interface reaction (GSIR) and cycling performance of the pristine and GSIR $Li_{1.144}Ni_{0.136}Co_{0.136}Mn_{0.544}O_2$.[143] Reproduced with permission,[66] Copyright 2006, American Chemical Society. Reproduced with permission,[190] Copyright 2011, IOP Publishing. Reproduced with permission,[189] Copyright 2014, Royal Society of Chemistry. Reproduced with permission,[191] Copyright 2017, Royal Society of Chemistry. Reproduced with permission,[143] Copyright 2015, Wiley-VCH.

Meng's group[188] found that the oxygen vacancies in the $Li[Li_{1/5}Ni_{1/5}Mn_{3/5}]O_2$ electrode introduce stacking faults, cation mixing, and an undesired new phase, which leads to degraded electrochemical performances. In another work of Meng,[189] they studied the relationship between oxygen vacancies and cation migration in $Li[Li_{1/6}Ni_{1/4}Mn_{7/12}]O_2$ and suggested that when the oxygen vacancies are located at the octahedral sites but not in the shared plane, the diffusion barrier of both Ni (Fig. 7c) and Mn is low and the corresponding migration from the TM layer to Li layer is facilitated, thus leading to the generation of spinel-like phases. Moreover, oxygen vacancies in the lattice could lead to the change in the oxidation state of the TM ions and the formation of pores. In 2017, Shim *et al.*[191] found an unexpected Mn reduction during the first charging process of the $0.4Li_2MnO_3{-}0.6LiNi_{1/3}Co_{1/3}Mn_{1/3}O_2$ electrode through EELS (Fig. 7d) and XAS. They suggested that the presence of Mn^{3+} and $Mn^{2+/3+}$ ions might originate from LS transition that is created by oxygen deficiency. In addition, when being charged to 4.7 V *vs.* Li/Li^+, the formation of porous morphologies due to the removal of lattice oxygen has been observed in the particles.[191] Similar results have also been obtained by Yu and his co-workers.[187] In 2019, Yan *et al.*[192] confirmed that the nanopores in the bulk lattice were formed due to the migration of oxygen vacancies from the surface into the bulk, which, according to their theoretical calculations, was mediated by oxidized oxygen ions rather than O^{2-}. Thus, the O_2 release and the oxygen vacancies left in the lattice during electrochemical delithiation are pernicious to structural stability and electrochemical performance.

Interestingly, it was reported that the oxygen vacancies produced on the surface during the materials preparation process are beneficial for the stability of LMROs. In 2016, Meng's group[143] introduced an oxygen vacancy layer ($\sim$20 nm) on the surface of $Li_{1.144}Ni_{0.136}Co_{0.136}Mn_{0.544}O_2$ particles by a gas/solid interfacial reaction and obtained a stable electrode with a high discharge capacity of 301 mA h g^{-1} and a capacity retention of over 99% after 100 cycles, as shown in Fig. 7e. The theoretical calculation and DEMS results suggested that this oxygen vacancy layer facilitates Li diffusion from the Li layers to TM layers in the bulk at the last stage of discharge and suppresses the O_2 release near the surface, thus resulting in significant improvement of electrochemical performance.

In summary, the formation of oxygen vacancies has been widely recognized as the result of the O_2 release in LROs, but it is still facing several challenges to gain in-depth knowledge. First, methods for characterizing oxygen vacancies are limited to XRD, ND or EELS, and the accurate and localized knowledge of these methods are scarce. Second, the distribution of the oxygen vacancies in particles is less discussed, *i.e.*, whether they exist in the bulk or just at the particle surface remains unknown. Third, since key structural information and effective characterization techniques are still lacking, the theoretical calculation is utilized as the primary method to estimate the effects of oxygen vacancies on the structural evolution and electrochemical performance. In particular, how to construct a qualified structural mode during calculation and how to verify these valuable results should be taken into consideration.

3.3 Structural evolution of LLROs

As discussed in Section 2.1, research interest in LLROs has been aroused by the discovery of the "electrochemical activation plateau" at ~4.5 V (*vs.* Li/Li$^+$) in 2001.[42] Fig. 8a shows the initial charge/discharge curve of $Li_{1.2}Ni_{0.13}Co_{0.13}Mn_{0.54}O_2$, which is a typical LMRO material.[70] Below 4.5 V, a smooth slope can be observed in the charge profile and the charges of extracted Li$^+$ are mainly compensated by the oxidation of TM ions. Then a voltage plateau appears, at which the charge voltage further increases to 4.5–4.6 V and the lattice oxygen redox is activated, which participates in the charge compensation of LMROs and provides excess capacity beyond cation redox. However, the high voltage causes the overoxidation of lattice oxygen and the decomposition of the typical used mixed organic carbonate solvent electrolyte, resulting in the O_2 and CO_2 release, as shown in Fig. 8a.[70] Indeed, O^{2-} overoxidation is the primary challenge of LROs since it leads to low initial coulombic efficiency (ICE), severe structural and interfacial breakdown, and serious safety concerns. In addition, this plateau only appears at the initial charge process, and the curves of the initial discharge process and the following cycles are smoother and show only one slope. This observation indicates that the structural transformation in the first and following cycles might be different. In the following sections, the complicated structural evolution of LLROs will be discussed, including the extraction of Li from the TM layers, lattice parameter evolution, TM migration, LS transition and the densification phase.

3.3.1 Extraction of Li$^+$ from the TM layers. As introduced in Section 2.3, the cation ordering reflections located at 20–30° in a XRD pattern are usually attributed to the honeycomb structure of the TM layers.[84,167,188] As shown in Fig. 8b,[73] the XRD patterns of the $Li_{1.17}Ni_{0.21}Co_{0.08}Mn_{0.54}O_2$ electrode at different charge/discharge states reveal that the intensities of these peaks decrease at the plateau of the initial charge process, suggesting the irreversible loss of the in-plane cation ordering and the de-intercalation of excess Li ions from the TM layers. Most often, the superlattice peaks in the XRD patterns disappear at the end of the plateau, but they are observed to be well maintained during the whole charge/discharge processes in the synchrotron XRD patterns of the $Li_{1.2}Ni_{0.2}Mn_{0.6}O_2$ electrode, as shown in Fig. 8c.[188] Thus, debates still exist about at which potential the excess Li$^+$ is extracted from the TM layers and whether this extraction reaction is reversible. In 2004, based on the NMR spectra of $Li[Li_{1/9}Mn_{5/9}Ni_{1/3}]O_2$, Grey *et al.*[194] found that the Li$^+$ ions are extracted from the TM layers before the plateau during charge and they return during discharge. After 20 cycles, the signals corresponding to the Li$^+$ ions in the TM layers are extremely weak, indicating that this process is partially reversible. In 2009, based on the ^{6}Li MAS NMR spectra

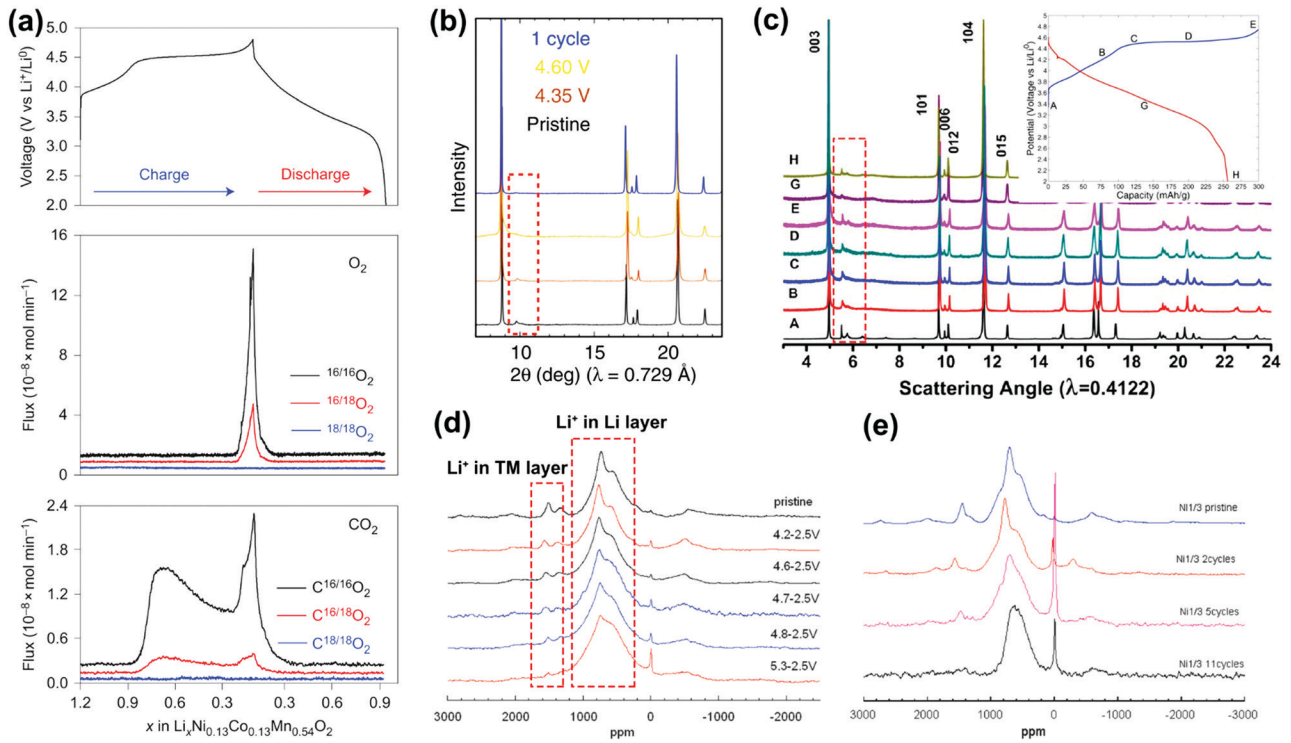

Fig. 8 Extraction and the following insertion of Li$^+$ in TM layers of LMROs. (a) The initial charge/discharge curve and the corresponding gas release of the $Li_{1.2}Ni_{0.13}Co_{0.13}Mn_{0.54}O_2$ electrode.[70] XRD patterns of $Li_{1.17}Ni_{0.21}Co_{0.08}Mn_{0.54}O_2$[73] (b) and of $Li_{1.2}Ni_{0.2}Mn_{0.6}O_2$[182] (c) at different charge/discharge states. ^{6}Li MAS NMR spectra of the discharged samples recorded (d) at the 1st cycle with different charge cut-off voltages and (e) after different cycle numbers within the voltage window of 2.5–4.6 V.[193] Reproduced with permission,[70] Copyright 2016, Nature Publishing group. Reproduced with permission,[73] Copyright 2017, Nature Publishing group. Reproduced with permission,[182] Copyright 2018, Wiley-VCH. Reproduced with permission,[193] Copyright 2009, American Chemical Society.

of the pristine $Li[Li_{1/9}Ni_{1/3}Mn_{5/9}]O_2$ electrode and electrodes at the pristine state and at the end of the 2nd, 5th and 11th cycles, Grey's group further confirmed that Li cannot intercalate back to the TM layers after several cycles, as shown in Fig. 8d and e.[193] However, in the same year, by investigating the initial discharge capacities of Li_2MnO_3 at different states of charge, Yu *et al.*[195] proposed that Li^+ is extracted from both Li and TM layers simultaneously and no Li^+ ions re-enter into the TM layers during discharge. The poor reversibility of (de)intercalation of Li^+ (from) in the TM layers was also confirmed by *operando* neutron diffraction by Liu *et al.*[166] in 2016. Their results indicated that little or no Li^+ is extracted from the TM layers before the plateau and very few Li^+ intercalates back into the TM layers after being charged to high voltages. Importantly, they proposed that the Li^+ ions migrate to the tetrahedral sites during the plateau and prevent the migrated Li^+ ions from returning to the TM layers. From the above discussions, we can conclude that most of the Li^+ ions in the TM layers may be extracted at the plateau and the reversibility of de-intercalation of these Li^+ ions in the TM layers is poor.

3.3.2 The evolution of lattice parameters. *In situ* XRD is a powerful tool to investigate the structure evolution of electrodes during the charge/discharge process. Up to now, this technique has been applied to many LLROs, such as $Li[Ni_xLi_{1/3-2x/3}Mn_{2/3-x/3}]O_2$,[79] $Li[Li_{0.23}(Ni_{0.2}Mn_{0.8})_{0.77}]O_2$,[196] $Li[Li_{1/9}Ni_{3/9}Mn_{5/9}]O_2$,[197] $Li_{1.2}Mn_{0.61}Ni_{0.18}Mg_{0.01}O_2$,[198] and $Li_{1.2}Co_{0.1}Mn_{0.55}Ni_{0.15}O_2$.[199] In 2002, Lu *et al.*[79] investigated the structural changes of $Li[Ni_xLi_{1/3-2x/3}Mn_{2/3-x/3}]O_2$ samples at $x = 5/12$ and 1/6 by *in situ* XRD and provided the evolution of *a*, *c* and *V* parameters. As shown in Fig. 9a, at $x = 1/6$ in $Li[Ni_xLi_{1/3-2x/3}Mn_{2/3-x/3}]O_2$, *a* decreases and *c* increases at the slope section of the initial charge due to the oxidation of the TM ions and the increased repulsion between neighboring TMO_2 slabs, respectively. At the plateau, *a* is stable, while *c* remains constant in the first half of the plateau and then decreases rapidly in the later half. At $x = 5/12$, *a* remains stable and *c* decreases during the course of the plateau. During the discharge process, both *a* and *c* smoothly increase. At the 2nd cycle, *a* and *c* decrease during the charge process and increase during the discharge process, revealing that the structural evolution of LLROs during the anionic redox reactions in the 1st cycle is different from that in the following cycles. Lu *et al.*[79,80] ascribed the usual *c* changes at the plateau to the loss of lattice oxygen and the extreme extraction of Li^+. Similar *in situ* XRD results have been observed for other LMROs. For example, Simonin *et al.*[200] found that both *a* and *c* remain constant at the plateau of the initial charge process. Mohanty *et al.*[199] also observed that during the charge plateau, the change in *c* is very small at the first half of the plateau but then *c* decreases significantly at the second half of the plateau. A similar trend in structural evolution was further observed by *in situ* EXAFS and *operando* ND. Both *in situ* XAS results of $Li_{1.2}Ni_{0.17}Mn_{0.56}Co_{0.07}O_2$[201] (Fig. 9b) and *operando* XAS results of $Li_{1.2}Mn_{0.54}Ni_{0.13}Co_{0.13}O_2$[91] revealed that,

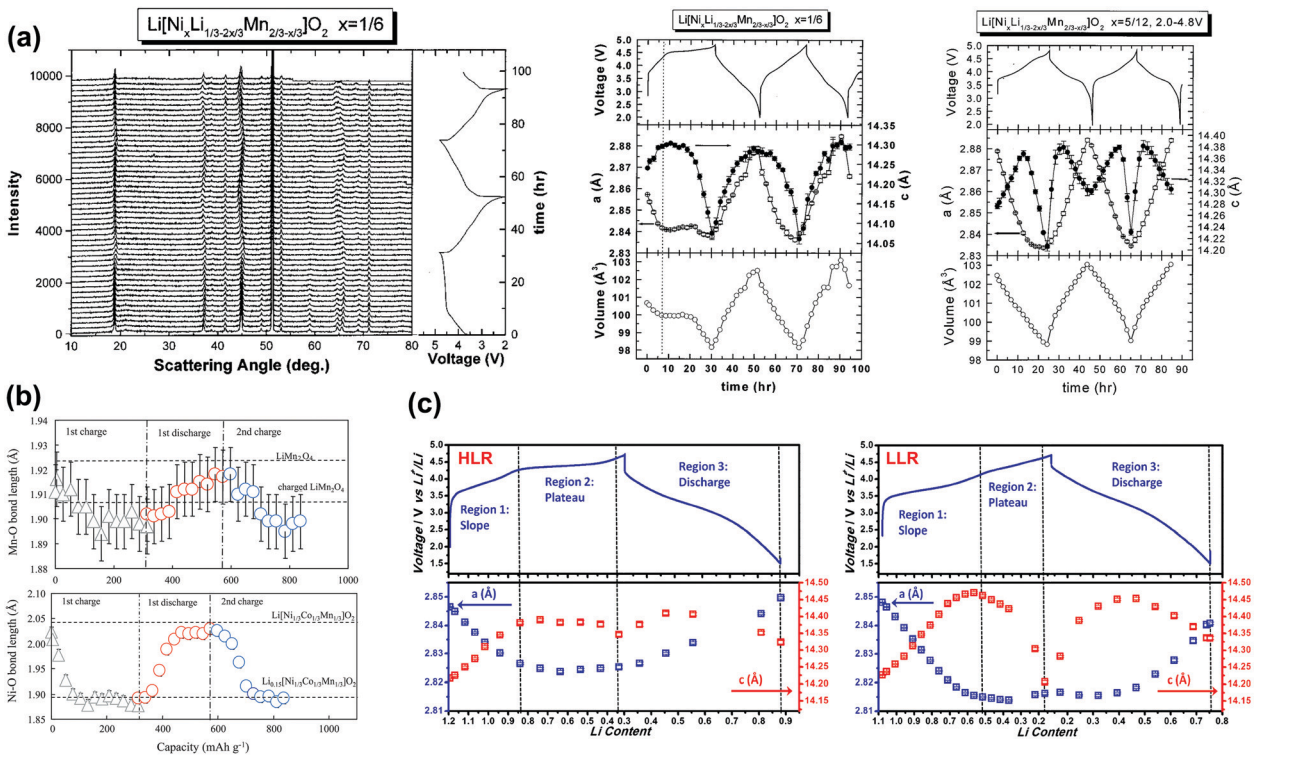

Fig. 9 The evolution of lattice parameters of LMROs. (a) *In situ* XRD patterns and the change in *a* and *c* lattice dimensions, and the cell volume of $Li_{x/3+1/3}Ni_xMn_{2/3-x/3}O_2$ with $x = 1/6$ and 5/12 along cycling.[79] (b) Evolution of Ni–O and Mn–O bonds in the initial cycle of $Li_{1.2}Ni_{0.17}Mn_{0.56}Co_{0.07}O_2$ revealed by *in situ* XAS.[201] (c) Evolution of *a* and *c* in the initial cycle of LMROs with high-lithium content (HLR) and low-lithium content (LLR) obtained by the *operando* ND technique.[166] Reproduced with permission,[79] Copyright 2002, IOP Publishing. Reproduced with permission,[201] Copyright 2011, Elsevier. Reproduced with permission,[166] Copyright 2016, Wiley-VCH.

during the initial charge process, all Ni–O, Mn–O, and Co–O bonds change little at the plateau, thus suggesting that the valence states of the TM ions at the plateau remain stable. However, it is difficult to explain why the ionic radius of lattice oxygen remains constant during the oxygen redox reactions. *Operando* ND results (Fig. 9c) of Liu *et al.*[166] demonstrated that, for LMROs with high-lithium content (HLR, *e.g.* $Li_{1.2}Ni_{0.15}Co_{0.1}Mn_{0.55}O_2$ in this work), *c* remains almost constant between the lithium content of 0.85 and 0.45 per formula unit and decreases slightly at the end of the plateau (at a lithium content of ~0.35), while for LMROs with low-lithium content (LLR, *e.g.* $Li_{1.08}Ni_{0.25}Co_{0.25}Mn_{0.41}O_2$), *c* decreases rapidly during the charge plateau. Liu *et al.* suggested that the less severe or delayed contraction of *c* in HLR may originate from their higher degree of oxygen redox activities than in LLR.[166] We speculate that the extraction of Li^+ from the TM layers, TM migration, and the local structural changes during oxygen redox reactions could be the main causes for the unusual *c* evolution in the first cycle of LMROs;/ however, the detailed mechanisms and their relationship with the performance need to be further explored.

3.3.3 TM migration and LS transition. The migration of the TM ions at highly delithiated states has been widely recognized in LLROs. The reaction is partially reversible in the bulk of particles. For LLROs, due to the partial reversibility of the (de)intercalation of Li^+ in the TM layers and the overoxidation of partial lattice oxygen, Li^+ and oxygen vacancies are left in the lattice at the electrochemical activation plateau, which facilitates the migration of the TM ions.[167,188,189] Besides, the species of oxidized lattice oxygen also influences TM migration. Based on DFT calculations, Chen *et al.*[182] proposed that oxygen dimerization could promote Mn migration from the TM layers to Li layers. In 2008, Tran *et al.*[84] proposed the migration of cations from slabs (TM layers) to interslabs (Li layers) during the charge plateau by using magnetic measurements and Rietveld refinement of XRD patterns. In general, the migration of the TM ions in the first cycle is recognized to be partially reversible. Gent *et al.*[73] found that the TM ions located in the Li layers increase from 2.8% to 9.0% during the charge process and return to 4.7% at the end of discharge based on the Rietveld refinement results of XRD (Fig. 10a). Besides, their DFT calculations suggested that the coupling between TM migration and O redox reactions leads to voltage hysteresis (Fig. 10b). Genevois *et al.*[168] studied the structural changes during the plateau of $Li_{1.20}Mn_{0.54}Ni_{0.13}Co_{0.13}O_2$ by HAADF-STEM. As shown in Fig. 10c,[168] the cation ordering (bright–bright–dark dots) in the TM layers is well maintained after the 1st cycle without the plateau, while the dark dots in both TM and Li layers become brighter after the 1st cycle with the plateau, indicating that the TM ions not only migrate to the Li vacancies within the TM layers but also migrate from the TM layers to Li layers when cycling at a high voltage plateau, and both migration pathways show low reversibility. The migration of the TM ions from the TM layers to Li layers and the returning back of the migrated TM ions to the TM layers, with good reversibility, have also been observed.[127,188] By comparing the HAADF-STEM images of layered $Li_2Ru_{0.5}Mn_{0.5}O_3$ electrodes at the pristine state, charged

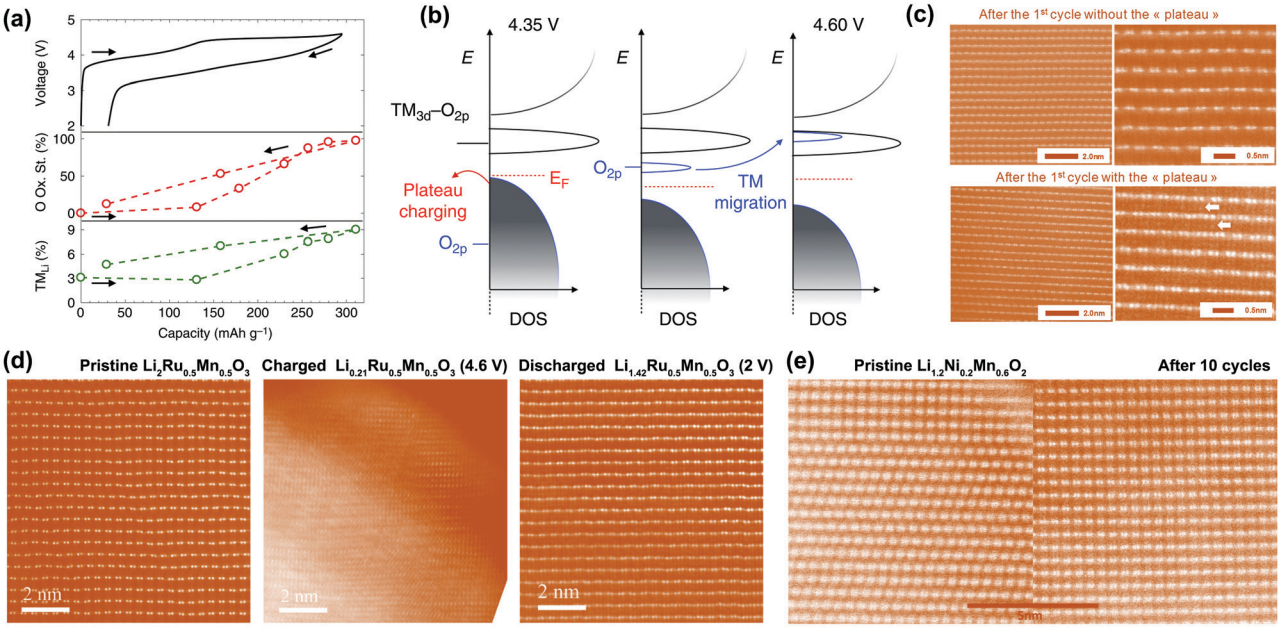

Fig. 10 TM migration in LLROs. (a) Relationship between the O fractional oxidation state and the migrated TM fraction, which indicates a link between voltage hysteresis and TM migration.[73] (b) Schematic illustration of the influence of TM migration on the electronic structure.[73] (c) HAADF-STEM images of $Li_{1.20}Mn_{0.54}Ni_{0.13}Co_{0.13}O_2$ in the discharge states with and without using the plateau at 4.5 V, suggesting that TM migration is closely related to the plateau.[168] (d) HAADF-STEM images of $Li_2Ru_{0.5}Mn_{0.5}O_3$ at different charge/discharge states.[127] (e) HAADF-STEM images of $Li_{1.2}Ni_{0.2}Mn_{0.8}O_2$ electrodes in the pristine state and after 10 cycles.[188] Reproduced with permission,[73] Copyright 2017, Nature Publishing group. Reproduced with permission,[168] Copyright 2014, American Chemical Society. Reproduced with permission,[127] Copyright 2017, American Chemical Society. Reproduced with permission,[188] Copyright 2013, American Chemical Society.

state (4.6 V) and discharged state (2.0 V) of layered $Li_2Ru_{0.5}Mn_{0.5}O_3$, Lyu *et al.*[127] found that the TM–TM–Li cation ordering in both Li and TM planes disappears at the charged state and re-emerges after the reinsertion of the Li ions (Fig. 10d), suggesting that most of the migrated TM ions move back to the original sites at the end of discharge. This is also supported by the HAADF-STEM results of $Li_{1.2}Ni_{0.2}Mn_{0.6}O_2$. Fell *et al.*[188] observed that the cation ordered structure of $Li_{1.2}Ni_{0.2}Mn_{0.6}O_2$ can be well maintained after 10 cycles (Fig. 10e). Interestingly, they found that the stacking sequence along the *c*-axis of the cycled material is more uniform as compared to the pristine one and attributed this phenomenon to the influence of the formation of oxygen vacancies.

The migration of TM ions at the surface is more severe than in the bulk, which leads to the LS transition near the surface.[202,203] Boulineau *et al.*[204] investigated the structural transitions of $Li_{1.2}Mn_{0.61}Ni_{0.18}Mg_{0.01}O_2$ at both the surface and bulk during cycling. As shown in Fig. 11a, the distribution of the Ni and Mn ions in the pristine sample is homogeneous. After 50 cycles, both the segregation of the Mn–Ni ions and the formation of a defect spinel-like phase can be observed near the particle surface. They proposed that the higher mobility of the Mn than the Ni ions results in such segregation because the Li vacancies in the TM layers are surrounded by the Mn rather than the Ni ions.[204] They further observed that although the TM ions migrate to the Li site in both TM layers and Li layers, the cation ordering structure is still preserved. Importantly, they found that the spinel-like phases are formed at the surface of particles with 2–3 nm thickness during the first cycle and no more extension of this phase could be observed after 50 cycles (Fig. 11b),[204] which may suggest that the spinel phase at the surface is not the main cause of voltage decay. The migration of the Ni ions from the bulk to the surface along with cycling was also observed in $Li_{1.2}Ni_{0.2}Mn_{0.6}O_2$ (Fig. 11c-d). By using HAADF-STEM and EDS mapping, Yan *et al.*[205] found that the structural evolution near the surface follows the sequence of $C2/m \rightarrow I41 \rightarrow$ spinel. A Ni-rich surface reconstruction layer (2–6 nm) is formed in the cycled $Li_{1.2}Ni_{0.2}Mn_{0.6}O_2$ electrode. Moreover, they confirmed that the electrode degrades upon reaction with the electrolyte and consequently the surface facet is terminated with a pure cation or anion, such as $(20\bar{2})$, which is more stable than the surface with the mixed cation and anion.[205] However, Gu *et al.*[206] found that the spinel phase extended from the surface to the bulk in $Li_{1.2}Ni_{0.2}Mn_{0.6}O_2$ during cycling, which considerably contributed to capacity fading and rate capability reduction. In addition, they proposed that the observed cracks (Fig. 11e) and pores of LROs should be attributed to LS transition and the removal of lattice oxygen. The STEM and EELS results obtained by Hu *et al.*[187] confirmed the formation of pores during synthesis. The observed increase in the size and number of pores during cycling is an indicator of electrode damage due to oxygen release. Moreover, thick layers and very thin layers of the spinel/rock-salt structure are observed in the exposed and concealed/partially exposed pores,

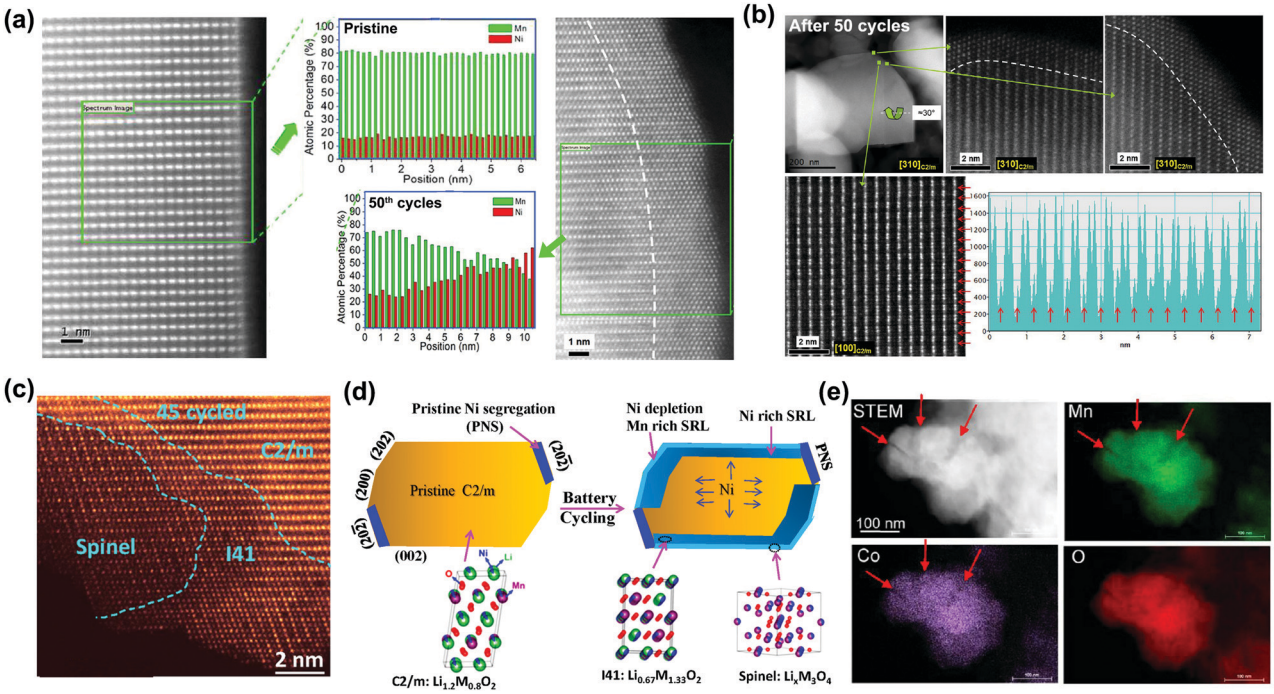

Fig. 11 Layered to spinel-like phase (LS) transition. (a) HAADF-STEM images and chemical maps of $Li_{1.2}Mn_{0.61}Ni_{0.18}Mg_{0.01}O_2$ in the pristine state and after 50 cycles showing the migration of TM ions.[204] (b) HAADF-STEM images of cycled $Li_{1.2}Mn_{0.61}Ni_{0.18}Mg_{0.01}O_2$ at the surface and bulk.[204] (c) HAADF-STEM image of $Li_{1.2}Ni_{0.2}Mn_{0.6}O_2$ after 45 cycles, showing the appearance of both spinel-like structure and *I*41 structure.[205] (d) Schematic diagram of surface layer evolution on $Li_{1.2}Ni_{0.2}Mn_{0.6}O_2$ during cycling.[205] (e) STEM and EDS mapping of $Li_{1.2}Ni_{0.1}Mn_{0.525}Co_{0.175}O_2$ after 60 cycles, showing the formation of particle cracks.[206] Reproduced with permission,[204] Copyright 2013, American Chemical Society. Reproduced with permission,[205] Copyright 2015, American Chemical Society. Reproduced with permission,[206] Copyright 2013, American Chemical Society.

respectively, which suggests that most of the spinel-like phases form at the surface of the particles. Similarly, Yan *et al.*[192] observed the spinel-like structure near the nanopores within the bulk $Li_{1.2}Mn_{0.6}Ni_{0.2}O_2$ electrode after 300 cycles. In conclusion, the fundamental understanding of structural evolution (*e.g.* TM migration, LS transition, and the formation of cracks and pores), along with the Li vacancies and oxygen vacancies formed during the plateau, is crucial for further enhancing the electrochemical performance of LLROs.

3.3.4 Densification mechanism. In 2006, based on the hypothesis that oxygen is released at the surface, Armstrong *et al.*[66] proposed two possible models to describe the detailed oxygen loss phenomenon in $Li_{1.2}Ni_{0.2}Mn_{0.6}O_2$, *i.e.*, (i) the diffusion of lattice oxygen from the bulk to the surface and thus leaving oxygen vacancies in the bulk and (ii) the migration of the TM ions from the surface to the bulk at the empty Li octahedral sites in the TM layers, resulting in densification near the surface. They found that the latter model results in a better refinement of the '4.8 V' ND pattern and proposed it as the nascent densification mechanism. Two years later, Tran *et al.*[84] verified the above two models for the charged $Li_{1.12}(Ni_{0.425}Mn_{0.425}Co_{0.15})_{0.88}O_2$ sample by XRD Rietveld refinement and confirmed the reliability of the densification mechanism. In 2013, Koga *et al.*[90] investigated the structural changes of $Li_{1.20}Mn_{0.54}Co_{0.13}Ni_{0.13}O_2$ during cycling by XRD and proposed the 'two-phase' mechanism. As shown in Fig. 12a,[90] a new peak located at ~18.8° appears in the XRD pattern of the electrode obtained at the end of charge (4.8 V), which has been ascribed to a densified layer based on the further Rietveld refinement results. Combined with their later work focusing on the reversible oxygen participation,[89] the final 'two-phase' mechanism comes into being: the over-oxidation of lattice oxygen in the outer part of the particles leads to oxygen release and the appearance of a new densification layer, while the bulk of particles undergo a reversible lattice oxygen redox process without major changes in the structure.[168] Moreover, as shown in Fig. 12b, Koga *et al.* found that the densified layer (marked as phase 2 in the XRD patterns) gradually increases with cycling.[90]

The particle size is crucial for the extent of densified layers in LROs. For example, Koga *et al.*[90] found that the proportion of the densified phase (phase 2) in the $Li_{1.2}Mn_{0.54}Co_{0.13}Ni_{0.13}O_2$ material at 4.8 V decreases with the increasing synthesis temperatures (Fig. 12a). In addition, they also observed in SEM images that the sizes of primary particles synthesized at higher temperatures are significantly larger than those prepared at lower temperatures, indicating that the proportion of the densified phase might be closely related to the particle size. Dahn's group[196] further investigated the effect of the particle size on the two-phase behavior of LMROs by *in situ* XRD experiments. As can be clearly observed in Fig. 12c, for big particles (~10 μm), both original and new (003) signals appear at the end of charge (4.8 V), corresponding to bulk and surface

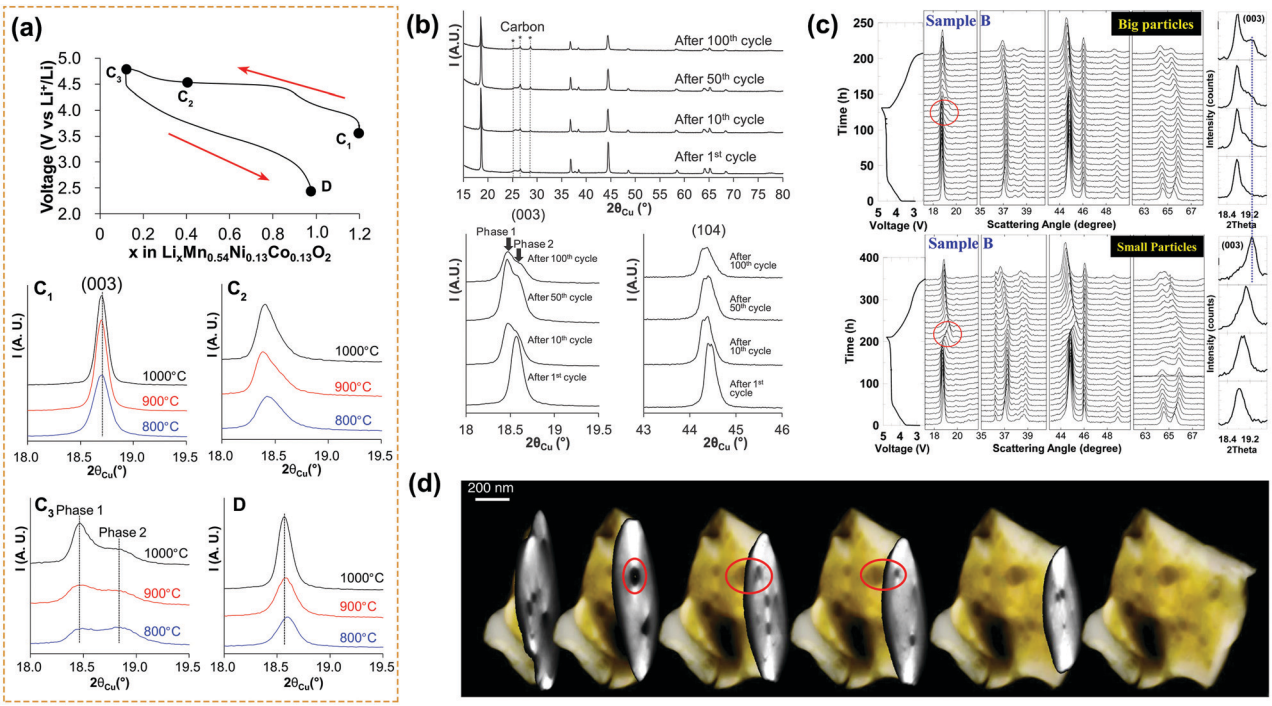

Fig. 12 The densification mechanism of LLROs. (a) Changes in the XRD patterns within 18–19.5° in the first cycle of $Li_{1.2}Ni_{0.13}Co_{0.13}Mn_{0.54}O_2$ synthesized at 800 °C, 900 °C and 1000 °C indicate a two-phase mechanism.[90] (b) XRD patterns of $Li_{1.2}Ni_{0.13}Co_{0.13}Mn_{0.54}O_2$ at the 1st, 10th, 50th, and 100th cycles suggest that the densified layer increases with cycling.[90] (c) *In situ* XRD patterns of LMROs with different particle sizes showing that the extent of the densified layer is related to the particle size.[196] (d) 3D electron tomography reconstruction of $Li_{1.2}Ni_{0.15}Co_{0.1}Mn_{0.55}O_2$ after 15 cycles showing generated pores in the LMRO electrode.[187] Reproduced with permission,[90] Copyright 2013, Elsevier. Reproduced with permission,[196] Copyright 2015, American Chemical Society. Reproduced with permission,[187] Copyright 2018, Nature Publishing group.

phases, respectively. While no splitting of the (003) reflections could be observed during the whole initial charge and discharge processes in the material with small particles (<1 μm), indicating that when the size is small enough, the material behaves as a densified phase throughout the entire particle.[196] Moreover, the generated cracks and pores during cycling might lead to an extension of the densified layer from the surface to the bulk. In 2018, Hu *et al.*[187] found a large number of pores surrounded by a thin shell of Mn^{2+} built-up in the bulk of the cycled $Li_{1.2}Ni_{0.15}Co_{0.1}Mn_{0.55}O_2$ electrode (Fig. 12d). The authors proposed that these pores are formed due to oxygen release and related lattice densification, suggesting that the densification exists at both the surface and bulk of LROs.

Although the 'two-phase' mechanism has been identified in a variety of LROs and widely accepted by many researchers,[70,90,187,196] several puzzles exist regarding experimental evidence and fundamental understanding. First, the thickness of the densified layer remains unknown. Second, Koga *et al.*[90] proposed this mechanism based on XRD results shown in Fig. 12a, however, it is very hard to explain the disappearance of the peak for the densified phase at the end of discharge (2.5 V) since the transformation between the pristine and densified phases should be irreversible. Third, the new phase formed during cycling is different from that appearing at the end of the first charge, but its true nature is not clarified yet. Consequently, the relationship between the densified layer and electrochemical performance has not been fully identified yet.

3.4 Structural evolution of DLROs

Although it is believed that the cation-disordered materials are highly tolerant to structural stress and strain and thus have good structural stability,[122,207] up to now, most of them still suffer from poor cycling performance.[208,209] Given that the TM ions and Li^+ ions are randomly located at the same sites, the structural changes of DLROs such as TM migration are difficult to trace as opposed to those of LLROs. In recent years, researchers have tried to clarify the capacity degradation mechanisms of DLROs and reached a consensus that the capacity decay might be closely related to the formation of a surface densified layer caused by the oxygen loss,[151,207,210] although experimental evidence is still very limited.

Very similar to LMROs, oxygen release is a serious challenge faced by DLROs. Fig. 13a shows the DEMS evidence for gas evolution of the $Li_{1.15}Ni_{0.375}Ti_{0.375}Mo_{0.1}O_2$[211] material in the first cycle. It can be observed that a large amount of O_2 is generated at ~4.35–4.80 V at the initial charge process. In contrast to the poor cycling stability of these DLROs with severe oxygen loss, those cation-disorder oxides without or less oxygen loss during cycling, such as $Li_{1.3}Nb_{0.3}V_{0.4}O_2$[212] and $Li_{1.2}Mn_{0.65}Nb_{0.15}O_{1.9}F_{0.1}$,[213] usually exhibit better cycling performance. Therefore, the oxygen loss

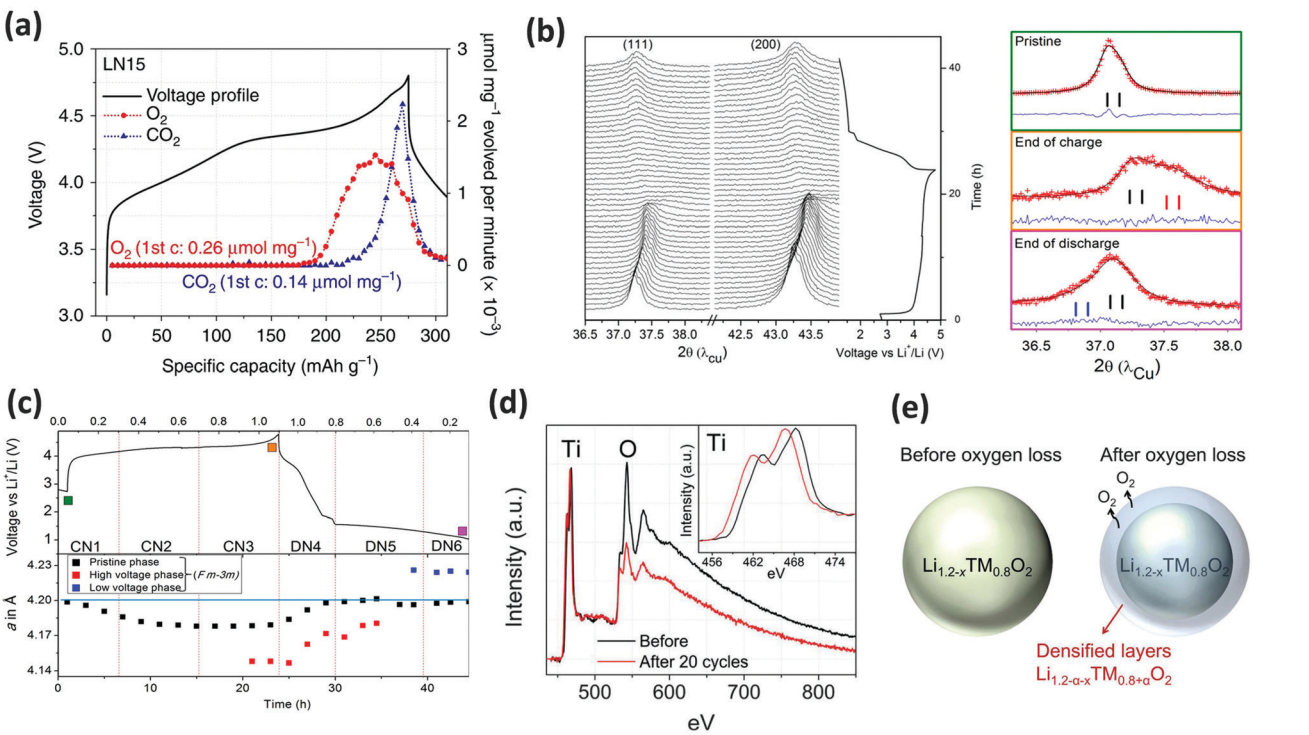

Fig. 13 Degradation mechanisms of the electrochemical performances of DLROs. (a) DEMS results of $Li_{1.15}Ni_{0.375}Ti_{0.375}Mo_{0.1}O_2$, showing O_2 and CO_2 release along cycling.[211] (b) *In situ* XRD patterns and (c) corresponding Rietveld refinement results of cation-disordered $Li_{1.3}Ni_{0.27}Ta_{0.43}O_2$, demonstrating the formation of a densified layer during the initial charge/discharge processes.[214] (d) EELS of Ti L-edge and O K-edge in $Li_{1.2}Ni_{1/3}Ti_{1/3}Mo_{2/15}O_2$ before cycling and after 20 cycles.[151] (e) Illustration of the formation of densified layers in DLROs.[151] Reproduced with permission,[211] Copyright 2017, Nature Publishing group. Reproduced with permission,[214] Copyright 2019, American Chemical Society. Reproduced with permission,[151] Copyright 2015, Royal Society of Chemistry.

is believed to be one of the critical factors associated with capacity decay.

The formation of the densified layer in DLROs is similar to that in LLROs. Specifically, the oxygen vacancies are formed near the surface of particles due to the oxygen release, and they destabilize the local metal-coordination structure, cause the migration of transition metal ions, and finally result in the formation of densified layers. Importantly, Ceder *et al.*[151] confirmed through theoretical calculations that these densified layers are more thermodynamically stable than the oxygen vacancies in cation-disordered $Li_{1.2}Ni_{1/3}Ti_{1/3}Mo_{2/15}O_2$. Fig. 13b and c shows the structural evolution of a typical cation-disordered oxide $Li_{1.3}Ni_{0.27}Ta_{0.43}O_2$ along with its *in situ* XRD patterns.[214] During the charge/discharge process, the general cubic phase structure is maintained with the changes in peak intensity and the peak position. At the end of charge, the appearance of shoulder peaks indicates that a new cubic phase that may correspond to a densified phase emerges with the release of oxygen. Ceder *et al.* investigated the oxygen loss in $Li_{1.2}Ni_{1/3}Ti_{1/3}Mo_{2/15}O_2$ by EELS.[151] As shown in Fig. 13d, the ratio of O/Ti signal intensities in $Li_{1.2}Ni_{1/3}Ti_{1/3}Mo_{2/15}O_2$ decreases by $\sim$39% after 20 cycles.[151] According to the lattice densitification mechanisms, this EELS results indicate that the chemical composition near the surface of the particles changes from $Li_{1.2-x}TM_{0.8}O_2$ to $Li_{0.7-x}TM_{1.3}O_2$, as illustrated in Fig. 13e.[151]

It has been recognized that the electrochemical activity of DLROs relies on their percolating network of 0-TM channels,[69] which could only be formed at high Li/TM ratios. However, the above results (Fig. 13d-e) unveiled that the Li/TM ratio in the densified layers is much lower than that in the pristine electrode, thus increasing the diffusion resistance of the lithium ions and resulting in rapid electrode degradation.[151] Chen *et al.*[210] pointed out that the same process also exists in $Li_{1.3}Nb_{0.3}Mn_{0.4}O_2$ and that the densified layer gradually expands from the surface into the bulk of particles with cycling. Although the densified layer has been widely accepted as one of the main results of structural transformation, it is still doubtful whether it plays a major role in capacity/voltage decay. Other possible factors, including parasitic reactions at the electrode surface,[152,215] dissolution of transition metal ions,[69,134] Mn^{3+} Jahn–Teller distortion,[213] *etc.*, may also contribute greatly to the capacity/voltage decay in DLROs. Thus, more powerful techniques, such as HAADF/ABF STEM, ss-NMR, *etc.* are urgently needed to recognize the structural and chemical evolution and further to clarify the underlying mechanisms of DLROs during charge/discharge cycling.

3.5 Electrochemical performance of LROs

3.5.1 Modifications and electrochemical performances of LLROs. Very recently, Ceder and his co-workers have reviewed the electrochemistry of the disordered lithium-rich oxides (DLROs) and oxyfluorides.[51] Herein, we will briefly review the modifications and electrochemical performance of LLROs in this section.

LLROs face several challenges. First, as discussed in the previous sections, the LLRO structure suffers from irreversible structural degradation processes, such as TM migration, LS transition, and structural densification. Second, to activate the oxygen redox of LLROs, it is a prerequisite to have a high charge cut-off potential (4.6–4.8 V *vs.* Li/Li^+) that goes beyond the electrochemical stability window of carbonate-based organic electrolytes. For this reason, the LLRO electrodes undergo pernicious side reactions at the electrode/electrolyte interface, including the decomposition of the electrolyte, the formation of thick cathode electrolyte interphase (CEI) layers,[216] electrode corrosion due to contact with acidic electrolyte species (such as HF),[217] and the dissolution of transition metal ions. Moreover, the irreversible oxygen reactions such as oxygen gas release and radical oxygen evolution[218] exacerbate these parasitic reactions. As a consequence, four electrochemical barriers, *i.e.* low ICE, capacity decay during cycling, poor rate capability, and fast voltage fade, are well acknowledged for LLRO electrodes.

In the last decade, a great number of studies have been carried out on the the modification of LLRO materials with the aim of improving their electrochemical performance. As shown in Table 2, different elements and radicals, such as Mg,[219,220] Al,[221,222] Na,[223] Ba,[224] Ti,[225] Zn,[226] Zr,[227,228] K,[229] Sn,[230] Ca,[231] Y,[232,233] La,[234] B,[235,236] F,[237,238] Cl,[239] B–O,[240] PO_4^{3-},[241] *etc.*, have been introduced into the framework of LLROs. An effective substitution element can play one or more roles during the electrochemical process: (i) stabilizing the host framework, (ii) preventing TM migration, (iii) expanding Li layer spacing, and (iv) stabilizing the O radical. Up to now, both TM site substitution and surface substitution/doping have positive effects on improving ICE, cycling stability, and rate capability. However, some discussions regarding substitution/doping effects are still open, for example, whether substitution/doping with ions that have a large ionic radius (*e.g.* K^+) or high electronegativity (*e.g.* F^-) can hamper the migration of TM ions and thus mitigate voltage fade. In the near future, it is not only of great significance to mitigate structural transformation and to improve Li^+ (de)intercalation kinetics, but equally important to manipulate the electronic structure, tune redox behavior and reduce undesired irreversible oxygen reactions by adopting appropriate substitution/doping elements. To resolve interfacial problems, as summarized in Table 3, a great variety of materials have been utilized to modify the surface of LLROs, such as oxides,[242–247] fluorides,[245,248–250] phosphates,[251–256] silicates,[257] carbon,[258–260] polymers,[261] and so on. The main function of such a protective coating layer is to avoid the direct contact between the active material and electrolyte, thus reducing parasitic electrolyte oxidation and TM dissolution. It has also been observed in LLROs that the coating layers can delay the structural transitions near the surface, especially LS transition.[262] Therefore, such a coating usually leads to a longer cycle life. New electrolyte formulations and electrolyte additives, measures that are applied to resolve interfacial problems,[263,264] can also be applied to increase the cycling stability of LLROs. As shown in Table 4, a substantial number of electrolyte additives have been used as CEI-formers for LLROs, including borates,[265–268] sulfones,[269] sultones,[270] phosphites,[271,272] phosphates,[273–275] *etc.* Moreover, phosphates[275–277] can also serve as oxygen-scavengers

Table 2 Representatives of reported effective substitution/doping strategies for Li-rich oxides

Electrodes	Elements	Functions	1st dis-capacity (mA h g^{-1})	Cycling performance	Year
$Li_{1.2}Mn_{0.6-x}Ni_{0.2}Co_{0.13}Ti_xO_2$	Ti	Suppressing the oxidation of O^{2-}	—	—	2011[225]
$Li_{1.2}Mn_{0.54}Ni_{0.13}Co_{0.13}O_{1.95}F_{0.05}$	F	Stabilizing host framework	277 (C/5, 2.0–4.8 V)	88.1%, C/5, 50 cycles	2013[237]
$Li_{1.2}Mn_{0.6-x}Ni_{0.2}Y_xO_2$	Y	Expanding Li layer spacing	281 (C/10, 2.0–4.8 V)	85%, 40 cycles	2013[232]
$Li_{1.2-x}Mg_xMn_{0.54}Ni_{0.13}Co_{0.13}O_2$	Mg	Expanding Li layer spacing	~250 (C/10, 2.0–4.8 V)	76%, 100 cycles	2014[219]
$Li[Li_{0.2}Ni_{0.13}Co_{0.13}Mn_{0.54}]_{1-x}Mg_xO_2$	Mg	Expanding Li layer spacing	275 (40 mA g^{-1}, 2.0–4.8 V)	92.4%, 50 cycles	2014[220]
$Li_{1.2}Ni_{0.13}Mn_{0.54}Co_{0.13}$-$(BO_4)_{0.015}(BO_3)_{0.015}O_{1.925}$	BO_4, BO_3	Manipulating electronic structure	319 (C/10, 2.0–4.8 V)	89%, 300 cycles	2014[240]
$Li_{1.2}Mn_{0.6-x}Ru_xNi_{0.2}O_2$	Ru	Stabilizing the O radicals	—	—	2014[279]
$Li_{1.2}Ni_{0.13}Co_{0.13}Mn_{0.54}O_2$	K	Mitigating phase transition	315 (20 mA g^{-1}, 2.0–4.8 V)	85%, 110 cycles	2014[229]
$Li_{1.16}Mn_{0.59}Ni_{0.21}Sn_{0.03}O_2$	Sn	Expanding Li layer spacing	294 (5 mA g^{-1}, 2.0–4.8 V)	100% (100 mA g^{-1}, 125 mA h g^{-1}), 100 cycles	2015[280]
$Li_{1.2}Mn_{0.57}Ni_{0.17}Al_{0.06}O_2$	Al	Mitigating phase transition	~271 (25 mA g^{-1}, 2.0–4.8 V, 45 °C)	91%, 50 cycles	2015[221]
$Li_{1.2}Ni_{0.2}Mn_{0.6-x}Mo_xO_2$	Mo	Expanding Li layer spacing	245 (C/10, 2.0–4.8 V)	93.2%, 204 cycles	2015[281]
$Li_{1.2}Ni_{0.08}Co_{0.28}Mn_{0.54}Mo_{0.046}O_2$	Mo	Expanding Li layer spacing	296 (20 mA g^{-1}, 2.0–4.8 V)	~91%, 200 mA g^{-1}, 100 cycles	2015[282]
$Li_{1.2}Ni_{0.13}Co_{0.13}Mn_{0.54}O_2$	Zr	Stabilizing host framework	256 (12.5 mA g^{-1}, 2.0–4.6 V)	95%, 25 mA g^{-1}, 100 cycles	2015[227]
$Li_{1.2}Ni_{0.13}Co_{0.13}Mn_{0.54}O_2$	Zn	Stabilizing host framework	212.8 (C/20, 2.5–4.8 V)	83.5%, 1C, 100 cycles	2015[226]
$Li_{1.2}Ba_{0.005}Ni_{0.195}Mn_{0.6}O_2$	Ba	Stabilizing the O radicals	200 (25 mA g^{-1}, 2.0–4.8 V)	—	2015[224]
$Li_{1.2}Mn_{0.59}Ni_{0.19}B_{0.01}O_2$	B	—	250 (C/10, 2.0–4.8 V)	94%, 100 cycles	2015[235]
$Li_{1.2}Ni_{0.196}Mn_{0.595}Sn_{0.009}O_2$	Sn	Stabilizing host framework	212 (C/5, 2.0–4.8 V)	96.2%, 50 cycles	2015[230]
$Li_{1.2}Ni_{0.2}Mn_{0.6-x}Nb_xO_2$	Nb	Stabilizing host framework	254 (C/10, 2.0–4.8 V)	92.3%, 100 cycles	2015[283]
$Li_{1.21}K_{0.02}Mn_{0.616}Ni_{0.152}O_2$	K	Expanding Li layer spacing	299 (C/10, 2.0–4.8 V)	94%, C/2, 100 cycles	2016[284]
$Li_{1.2}Ni_{0.13}Co_{0.13}Mn_{0.54}O_2$	B	Stabilizing host framework	238 (60 mA g^{-1}, 2.0–4.8 V)	94%, 60 mA g^{-1}, 100 cycles	2016[285]
$Li_{1.2-x}Ti_xMn_{0.54}Co_{0.13}Ni_{0.13}O_2$	Ti	Enhancing conductivity	320 (C/5, 2.0–4.8 V)	71%, 300 cycles	2016[286]
$Li_{1.2}Ni_{0.16}Mn_{0.51}Al_{0.05}Co_{0.08}O_2$	Al	Stabilizing host framework	210 (C/10, 2.0–4.6 V)	96%, 100 cycles	2016[287]
$Li_{1.2}Mn_{0.515}Co_{0.075}Ni_{0.115}V_{0.015}O_2$	V	Stabilizing host framework	253 (C/10, 2.0–4.8 V)	90%, 1C, 50 cycles	2016[288]
$Li[Li_{0.2}Mn_{0.54}Ni_{0.13}Co_{0.13}]_{1-x}B_xO_2$	B	Suppressing structural transitions	253 (C/10, 2.0–4.6 V)	89.9%, C/5, 50 cycles	2016[236]
$0.6Li_2MnO_3{\cdot}0.4LiNi_{5/12}Co_{1/6}Mn_{5/12}O_2$	Zr	—	260 (20 mA g^{-1}, 2.0–4.8 V)	84%, 100 cycles	2016[228]
$Li[Li_{0.2}Mn_{0.54}Ni_{0.13}Co_{0.13}]_{1-x}Mo_xO_2$	Mo	Expanding Li layer spacing	276 (C/5, 2.0–4.8 V)	91%, 50 cycles	2016[289]
$Li_{1.2}Ni_{0.2-X/2}Mn_{0.6-X/2}Y_XO_2$	Y	Stabilizing the host framework	253 (C/10, 2.0–4.6 V)	92.7%, 50 cycles	2016[233]
$Li_{1.2}Ni_{0.13}Co_{0.13}Mn_{0.54-x}La_xO_2$	La	Stabilizing the host framework	286 (C/10, 2.0–4.6 V)	93.2%, 1C, 100 cycles	2016[234]
$Li_{1.2}Ni_{0.13}Co_{0.13}Mn_{0.54}O_2$	Na	Stabilizing the host framework	228 (C/10, 5th, 2.0–4.7 V)	233 mA h g^{-1}, C/5, 100 cycles	2016[223]
$Li_{1.99}Ni_{0.13}Co_{0.13}Mn_{0.54}Ca_{0.005}O_2$	Ca	Expanding Li layer spacing	273 (C/5, 2.0–4.8 V)	87%, 100 cycles	2017[231]
$Li_{1.14}Ni_{0.136}Co_{0.10}Al_{0.03}Mn_{0.544}O_2$	Al	Stabilizing the host framework	212 (C/10, 2.0–4.8 V)	94.7%, 100 cycles	2017[222]
$Li_{1.2}Ni_{0.13}Co_{0.13-x}Mn_{0.54}Al_2O_{2(1-y)}F_{2y}$	Al, F	Enhancing structural stability	220 (C/2, 2.0–4.8 V)	88.2%, C/2, 150 cycles	2017[290]
$Li_{1.11}Ni_{0.89}O_{2-y}Cl_y$	Cl	Tuning redox behavior	—	—	2017[239]
$Li[Li_{0.2}Mn_{0.56}Ni_{0.16}Co_{0.08}]_{1-x}Te_xO_2$	Te	Enhancing structural stability	271.6 (C/10, 2.5–4.6 V)	84.3%, C/2, 100 cycles	2017[291]
$Li_{1.2}Ni_{0.13}Co_{0.13}Mn_{0.54-x}Cr_xO_2$	Cr	Suppressing structural transitions	230 (C/10, 2.0–4.8 V)	93.7%, 50 cycles	2017[292]
$Li_{1.2}Ni_{0.13}Co_{0.13}Mn_{0.54-x}Fe_xO_2$	Fe	Suppressing structural transitions	230 (C/10, 2.0–4.8 V)	90%, 50 cycles	2017[292]
$Li_{1.17}Na_{0.03}Ni_{0.13}Co_{0.13}Mn_{0.53}P_{0.01}O_2$	Na, PO_4^{3-}	Expanding Li layer spacing	255 (C/10, 2.0–4.8 V)	93.8%, 1C (182 mA h g^{-1}), 100 cycles	2018[241]
$Li_{1.2}Mn_{0.52}Ni_{0.13}Co_{0.13}La_{0.02}O_2@CaF_2$	La	—	275.1 (C/20, 2.0–4.8 V)	93.9%, C/2, 100 cycles	2018[293]
$Li_{1.13}Ni_{0.3}Mn_{0.57}O_2$	W (1 vol%)	—	284 (C/20, 2.0–4.8 V)	66%, 100 cycles	2018[294]
$Li_{1.2}Mn_{0.54-x}Nb_xNi_{0.13}Co_{0.13}O_{2-6x}F_{6x}$	Nb, F	Suppressing structural changes	269 (C/10, 2.0–4.8 V)	94%, 1C, 100 cycles	2018[295]
$Li_{7/6}Ni_{1/6}Co_{1/6}Mn_{1/2}O_{1.95}F_{0.05}$	F	Improving thermal stability	~255 (C/10, 2.0–4.6 V)	—	2018[238]
$Li_{1.2}(Mn_{0.54}Ni_{0.13}Co_{0.13})_{1-x}Cr_xO_2$	Cr	Stabilizing the O radicals	~260 (C/20, 2.0–4.6 V)	91%, 1C (175 mA h g^{-1}), 200 cycles	2018[296]
$Li_{1.2}Ni_{0.2}Mn_{0.6}O_2$	Mo, Co	Mitigating oxygen release	297 (12.5 mA g^{-1}, 2.0–4.8 V)	86.5%, 25 mA g^{-1}, 50 cycles	2018[297]
$Li_{1.2}Mn_{0.52}Ni_{0.13}Co_{0.13}Mn_{0.01}Al_{0.01}O_2$	Mg, Al	Expanding Li layer spacing	271.9 (C/20, 2.0–4.8 V)	81%, C/10, 100 cycles	2019[298]
$Li_{1.2}Mn_{0.54}Ni_{0.13}Co_{0.13}O_2$	Sn, K	Expanding Li layer spacing	278 (C/2, 2.0–4.6 V)	70%, 100 cycles	2019[299]
$Li_{1.2}Mn_{0.54}Ni_{0.13}Co_{0.13-x}Yb_xO_2$	Yb	Expanding Li layer spacing	295 (C/10, 2.0–4.8 V)	87%, C/5, 100 cycles	2019[300]
Li-rich Li–Ni–Mn–Co–O	P	Expanding Li layer spacing	296 (C/10, 2.0–4.8 V)	73%, 1C (247 mA h g^{-1}), 500 cycles	2019[301]

Table 2 (*continued*)

Electrodes	Elements	Functions	1st dis-capacity (mA h g^{-1})	Cycling performance	Year
$Li_{1.18}Mn_{0.52}Co_{0.13}Ni_{0.13}La_{0.02}Mg_{0.02}O_2$	Mg, La	Preventing TM migration	296 (C/10, 2.0–4.8 V)	86.1%, C/2, 150 cycles	2019[302]
$Li_{1.2}Ni_{0.13}Co_{0.13}Mn_{0.54-x}Re_x-[(BO_4)_{0.75y}(BO_3)]_{0.25y}O_{2-3.75y}$	Re, B	Stabilizing the O redox	202 (400 mA g^{-1}, 2.0–4.8 V)	81%, 300 cycles	2019[303]
$Li_{1.2}Ni_{0.2}Mn_{0.6}O_2Cd_{0.03}S_{0.03}$	Cd, S	Expanding Li layer spacing	268 (C/10, 2.0–4.8 V)	90.6%, 80 cycles	2019[304]

to remove the generated O_2 and radical oxygen atom produced by the over-oxidation of lattice oxygen. Overall, to enable a long life for LLROs, a suitable electrolyte system should satisfy the following requirements:[26] (i) a wide electrochemical stability window to ensure its electrochemical and chemical stability during battery operation, (ii) the capability to form a uniform, effective and robust solid electrolyte interphase (SEI)[278] and CEI on the surface of both positive and negative electrodes, and (iii) the capability to eliminate the by-products of oxygen redox reactions (*e.g.* O_2).

The electrochemical performance of LLROs can be greatly improved by substitution/doping, coating and electrolyte-modulation strategies. However, it is rarely reported that the voltage fade of LLROs can be greatly eliminated by these conventional modification methods. Most of the articles have not quantified the voltage fade before and after modification. In addition, voltage fade is a result of various bulk-structure transformations. These modification methods, especially coating and electrolyte modulation, would have limited effects on delaying the voltage decay as they are more or less surface related strategies.

3.5.2 Voltage fade in LLROs. Up to now, cycling stability has no longer been a major concern for the practical applications of LLROs. Many reports have shown significant improvements in the cycling stability through various strategies. For example, by coating $Li_{1.2}Ni_{0.15}Co_{0.1}Mn_{0.55}O_2$ with AlF_3, Zheng *et al.*[262] enhanced the capacity retention from 80.9% (uncoated sample) to ~100% (coated sample) at the 100th cycle. Qiu *et al.*[347] obtained ~100% capacity retention after 100 cycles from the $Li_{1.144}Ni_{0.136}Co_{0.136}Mn_{0.544}O_2$ electrode by creating oxygen vacancies on the particle surface. However, although all these reports present almost no capacity fading for LLROs, the voltage decay is unfortunately remarkable. As shown in Fig. 14a, the $Li_{1.2}Ni_{0.2}Mn_{0.6}O_2$ material synthesized by a hydrothermal assisted method[141] delivers a high capacity retention of ~100% after 100 cycles at C/10, but the continual shift of both charge and discharge profiles to the lower voltage regions with cycling can be clearly viewed. This shows a typical voltage fade phenomenon of LMROs, which results in the diminution of energy density. At present, voltage fade becomes the primary challenge faced by LROs.[54,55,348]

As discussed in the above sections, the migration of the TM ions leads to LS transition. Both TM migration (especially from the TM layers to the tetrahedral sites in the Li layers) and spinel-like phase formation have been listed as the main reasons for capacity and voltage fade.[54,141] Mohanty *et al.*[167] investigated the cation migration pathways of $Li_{1.2}Mn_{0.55}Ni_{0.15}Co_{0.1}O_2$ by ND. The refined pattern fitted well with the experimental ND data by employing three-phase models of trigonal, monoclinic and spinel phases. Based on the Rietveld refinement results of ND, they proposed that the spinel phases are formed through the migration of the Li and Mn ions from octahedral sites in the TM layers to tetrahedral sites and octahedral sites in the Li layers, respectively. Importantly, the alteration of the Mn and Li sites might ease the movement of the Li ions, lower the operating voltage of the cell and thus lead to voltage fade. Apparently, in that report, LS transition was regarded as a bulk feature of the LLROs rather than being restrained only at the surface. Therefore, substitution with alkali atoms and reduction of the manganese content were proposed as potential solutions to minimize voltage fade.[167] By using aberration-corrected STEM, Zheng *et al.*[141] investigated the structural changes of the $Li_{1.2}Ni_{0.2}Mn_{0.6}O_2$ electrode with cycling and provided a possible mechanism for voltage fade. As illustrated in Fig. 14b, the layered structure transformed into a defect spinel structure and then converted to a disordered rock-salt structure with extended cycling. During this process, some of the 16c octahedral sites were occupied by the migrated TM ions, thus blocking reversible Li insertion/deinsertion and lowering the redox potential of LMROs.[141] In 2018, based on a comprehensive XAS investigation of $Li_{1.2}Ni_{0.15}Co_{0.1}Mn_{0.55}O_2$, Hu *et al.*[187] observed the continuous reduction of the average valence state of the TM ions during cycling (Fig. 14c), which resulted from oxygen release and led to the activation of the lower-voltage Mn^{3+}/Mn^{4+} and Co^{2+}/Co^{3+} redox couples. Besides, the significant amounts of pores and the surrounding build-up of Mn^{2+}/Mn^{3+} in the bulk contribute to valence changes (Fig. 14d). Recently, by studying the oxygen redox inactive $Li_{1.2}Ni_{0.2}Ru_{0.6}O_2$ electrode, Li *et al.*[157] have found that the microstructural evolution mainly originated from TM migration as a direct cause of the voltage fade phenomenon. It should be pointed out that the voltage fade in $Li_{1.2}Ni_{0.2}Ru_{0.6}O_2$ is much lower than in materials involving oxygen redox, which might indicate that oxygen related factors, such as O_2 release, are closely related to voltage fade. Therefore, voltage decay/fade can be mainly attributed to TM migration, LS transition, and O_2 release.

Effective strategies to achieve the complete elimination of voltage fade are still lacking. Surface/interface/interphase concerned methods, *i.e.* active material surface modification and film forming electrolyte additives, have attracted just some interest. For example, Zheng *et al.*[262] showed that AlF_3 coated $Li_{1.2}Ni_{0.15}Co_{0.1}Mn_{0.55}O_2$ exhibits a reduced voltage fade of 10.1% as opposed to 12.3% for the uncoated samples after 100 cycles. Bloom *et al.*[349] investigated the effects of coatings,

Table 3 Representatives of reported effective coating strategies for Li-rich oxides

Electrodes	Coating layer	Thickness (mass)	1st dis-capacity (mA h g^{-1})	Cycling performance	Year
$Li_{1.05}Ni_{0.4}Co_{0.15}Mn_{0.4}O_2$	Various oxides	10 nm	—	—	2007[242]
$Li_{1.2}Ni_{0.13}Co_{0.13}Mn_{0.54}O_2$	AlF_3	—	267 (C/10, 2.0–4.8 V)	87.9%, 0.5C, 80 cycles	2008[248]
$Li_{1.2}Ni_{0.13}Co_{0.13}Mn_{0.54}O_2$	TiO_2	3 mol%	250 (18 mA g^{-1}, 2.0–4.8 V)	87%, 90 mA g^{-1}, 90 cycles	2008[305]
$Li_{1.2}Ni_{0.2}Mn_{0.6}O_2$	MnO_x	20 nm	298 (20 mA g^{-1}, 2.0–4.8 V)	89%, 20 mA g^{-1}, 30 cycles	2011[306]
$Li_{1.048}Mn_{0.381}Ni_{0.286}Co_{0.286}O_2$	C	5–8 nm	203.2 (C/10, 2.5–4.5 V)	94%, 100 cycles	2012[258]
$Li_{1.2}Ni_{0.13}Co_{0.13}Mn_{0.54}O_2$	ZrO_2	1 wt%	253 (C/10, 2.0–4.8 V)	207 mA h g^{-1}, C/2, 50 cycles	2013[243]
$Li_{1.2}Mn_{0.525}Ni_{0.175}Co_{0.1}O_2$	LiPON	<10 nm	275 (C/10, 2.0–4.9 V)	~85%, 350 cycles	2013[307]
$Li_{1.2}Ni_{0.13}Co_{0.13}Mn_{0.54}O_2$	Al_2O_3	3 wt%	250 (20 mA g^{-1}, 2.0–4.6 V)	92%, 100 mA g^{-1}, 100 cycles	2013[308]
$Li_{1.2}Ni_{0.13}Co_{0.13}Mn_{0.54}O_2$	$FePO_4$	5–10 nm	271 (C/20, 2.0–4.8 V)	95%, C/2, 100 cycles	2013[251]
$Li_{1.17}Ni_{0.2}Co_{0.05}Mn_{0.58}O_2$	$Li_3V_2(PO_4)_3$	3–4 nm	~320 (30 mA g^{-1}, 2.0–4.8 V)	90.1%, 60 mA g^{-1}, 50 cycles	2014[252]
$0.3Li_2MnO_3{\cdot}0.7LiNi_{5/12}Co_{5/21}Mn_{11/21}O_2$	ZnO	8 nm	316 (C/10)	81%, 50 cycles	2014[309]
$Li_{1.2}Ni_{0.15}Co_{0.1}Mn_{0.55}O_2$	AlF_3	10 nm	~250 (C/10, 2.0–4.8 V)	~100%, C/3, 100 cycles	2014[262]
$Li_{1.2}Mn_{0.54}Ni_{0.13}Co_{0.13}O_2$	Polyimide (PI)	—	269 (20 mA g^{-1}, 2.0–4.8 V)	90.6%, 50 cycles	2014[261]
$Li_{1.2}Mn_{0.54}Ni_{0.13}Co_{0.13}O_2$	CeF_3	10 nm	223 (C/10, 2.0–4.6 V)	91.7%, 50 cycles	2014[310]
$Li_{1.2}Ni_{0.2}Mn_{0.6}O_2$	$Li_{1+X}Mn_2O_4$	1–2 nm	295 (C/10, 2.0–4.8 V)	94.7%, 50 cycles	2014[311]
$Li_{1.2}Ni_{0.13}Co_{0.13}Mn_{0.54}O_2$	LiF & Spinel	1 nm	~265 (30 mA g^{-1}, 2.0–4.6 V)	89.1%, 150 mA g^{-1}, 200 cycles	2014[249]
$Li_{1.2}Fe_{0.1}Ni_{0.15}Mn_{0.55}O_2$	AlF_3	3 nm	250 (0.1C, 2.0–4.8 V)	87.9%, 50 cycles	2014[245]
$Li_{1.2}Fe_{0.1}Ni_{0.15}Mn_{0.55}O_2$	Al_2O_3	15 nm	272 (0.1C, 2.0–4.8 V)	84.2%, 50 cycles	2014[245]
$Li_{1.17}Mn_{0.48}Ni_{0.23}Co_{0.12}O_2$	MgO	2 wt%	260 (C/10, 2.0–4.8 V)	99.5%, 10 cycles	2014[244]
$Li_{1.2}Ni_{0.13}Co_{0.13}Mn_{0.54}O_2$	MnO_x	3% wt%	308 (0.1C, 2.0–4.8 V)	81%, 0.1C, 20 cylces	2014[247]
$Li_{1.2}Ni_{0.2}Mn_{0.6}O_2$	NH_4F, Al_2O_3	3 mol%, 1 mol%	287 (C/20, 2.0–4.8)	—	2015[312]
$Li_{1.17}Ni_{0.17}Co_{0.17}Mn_{0.5}O_2$	$LiMgPO_4$	2–3 nm	255 (C/10, 2.0–4.7 V)	72%, 1C, 250 cycles, 60 °C	2015[253]
$Li_{1.13}Ni_{0.30}Mn_{0.57}O_2$	Li_2SiO_3	10–30 nm	202 (20 mA g^{-1}, 2.0–4.8 V)	90%, 100 mA g^{-1}, 100 cycles	2015[313]
$Li_{1.2}Ni_{0.13}Co_{0.13}Mn_{0.54}O_2$	Li_3PO_4@C	3–7 nm	266 (30 mA g^{-1}, 2.0–4.6 V)	87%, 150 mA g^{-1}, 200 cycles	2015[259]
$0.5Li_2MnO_3{\cdot}0.5LiNi_{0.5}Co_{0.2}Mn_{0.3}O_2$	Al_2O_3	—	244 (C/5, 2.0–4.8 V)	98.6%, 100 cycles	2015[314]
$Li_{1.2}Ni_{0.13}Co_{0.13}Mn_{0.54}O_2$	$LiFePO_4$	7 nm	282.8 (C/10, 2.0–4.8 V)	98%, 120 cycles	2015[254]
$Li_{1.2}Fe_{0.1}Ni_{0.15}Mn_{0.55}O_2$	$AlPO_4$	5 wt%	296.4 (0.1C, 2.0–4.8 V?)	74.4%, 50 cycles	2015[255]
$Li_{1.2}Ni_{0.13}Co_{0.13}Mn_{0.54}O_2$	Samaria doped ceria	2–3 nm	261 (25 mA g^{-1}, 2.0–4.8 V)	—	2015[315]
$Li_{1.13}Ni_{0.3}Mn_{0.57}O_2$	Li_3PO_4	2 nm	319 (C/20, 2.0–4.8 V)	74.2%, 1C, 60 cycles	2016[316]
$Li_{1.2}Ni_{0.2}Mn_{0.6}O_2$	Li_3PO_4	2–7 nm	240 (C/10, 2.0–4.8 V)	90%, 50 cycles, 60 °C	2016[317]
Li_2MnO_3	TiO_2	1–3 nm	188.8 (20 mA g^{-1}, 2.0–4.8 V)	79.2%, 60 cycles	2016[318]
$Li_{1.8}Ni_{0.15}Co_{0.15}Mn_{0.7}O_{2.675}$	Li_2SiO_3	2 nm	250 (C/10, 2.0–4.8 V)	160 mA h g^{-1}, 94.3%, 1C, 200 cycles	2016[257]
$Li_{1.2}Ni_{0.13}Co_{0.13}Mn_{0.54}O_2$	Li_3PO_4	5 nm	226 (C/5, 2.0–4.8 V)	78%, C/5, 100 cycles	2016[319]
$Li_{1.2}Ni_{0.13}Co_{0.13}Mn_{0.54}O_2$	Li_3PO_4	4 nm	284.7 (C/20, 2.0–4.8 V)	85%, C/2, 100 cycles	2016[320]
$Li_{1.2}Ni_{0.2}Mn_{0.6}O_2$	$ZnAl_2O_4$	1 wt%	254 (0.1C, 2.0–4.8 V)	98.6%, C/5, 50 cycles	2016[321]
$Li_{1.2}Ni_{0.13}Co_{0.13}Mn_{0.54}O_2$	SnO_2	4–8 nm	264 (C/10, 2.0–4.8 V)	89.9%, 1C, 200 cycles	2016[322]
$Li_{1.2}Ni_{0.2}Mn_{0.6}O_2$	$LiAlO_2$	5 nm	237.1 (3C/50, 2.0–4.8 V)	90.5%, C/2, 2.0–4.6 V, 100 cycles	2016[323]
$0.4Li_2MnO_3{\cdot}0.6LiNi_{0.417}Co_{0.167}Mn_{0.417}O_2$	$LiNi_{0.5}Mn_{1.5}O_2$	2 mol%	270 (C/10, 2.5–4.7 V)	86.2%,? C, 2.5–4.6 V, 150 cycles	2017[324]
$Li_{1.2}Mn_{0.54}Ni_{0.13}Co_{0.13}O_2$	$Li_xNi_{0.5}Mn_{1.5}O_2$	5.4 nm	264 (C/5, 2.0–4.8 V)	94%, 1C, 100 cycles	2017[325]
$Li_{1.13}Ni_{0.3}Mn_{0.57}O_2$	WO_3	1 vol%	284 (C/20, 2.0–4.8 V)	188 mA h g^{-1}, 1C, 100 cycles	2018[294]
$Li_{1.2}Ni_{0.133}Co_{0.133}Mn_{0.534}O_{1.8}F_{0.2}$	Al_2O_3	5–7 nm	220 (after activation, C/20, 2–4.6 V)	176 mA h g^{-1}, C/10, 100 cycles	2018[326]
$Li_{1.2}Ni_{0.2}Mn_{0.6}O_2$	$LiAlF_4$	5.2 nm	246 (C/10, 2.0–4.8 V)	92.8%, 100 cycles	2018[250]
$Li_{1.2}Ni_{0.2}Mn_{0.6}O_2$	$LaNiO_3$	5–10 nm	216 (C/10, 2.0–4.8 V)	94.3%, 200 cycles	2018[327]
$Li_{1.2}Mn_{0.52}Ni_{0.13}Co_{0.13}La_{0.02}O_2$	CaF_2	—	275.1 (C/20, 2.0–4.8 V)	93.9%, C/2, 100 cycles	2018[293]
$Li_{1.214}Mn_{0.530}Co_{0.128}Ni_{0.128}O_2$	$Li_4Mn_5O_{12}$	14 nm	276 (C/20, 2.0–4.7 V)	83.1%, C/5, 300 cycles	2018[328]
$Li_{1.2}Ni_{0.13}Co_{0.13}Mn_{0.54}O_2$	Al_2O_3	20 nm	244 (C/20, 2.0–4.8 V)	—	2018[329]
$Li_{1.2}Ni_{0.13}Co_{0.13}Mn_{0.54}O_2$	CeO_2	4 wt%	281.9 (C/20, 2.0–4.8 V)	81.3%, 50 cycles	2018[246]
$Li_{1.2}Ni_{0.13}Co_{0.13}Mn_{0.54}O_2$	YF_3	2–3 nm	273 (C/20, 2.0–4.8 V)	85%, C/2, 150 cycles	2019[330]
$Li_{1.2-x}Na_xNi_{0.13}Co_{0.13}Mn_{0.54}O_2$	$Na_{1-x}Li_xF$	2 nm	230 (C/2, 2.0–4.8 V)	92%, 100 cycles	2019[330]
$Li_{1.2}Mn_{0.54}Ni_{0.13}Co_{0.13}O_2$	LATP@CNTs	—	275 (C/20, 2.0–4.8 V)	86.2%, C/5, 100 cycles	2019[260]
$Li_{1.2}Ni_{0.13}Co_{0.13}Mn_{0.54}O_2$	$LaPO_4$	2 wt%	249.8 (C/10, 2.0–4.8 V)	83.2%, 1C, 200 cycles	2019[256]

including Al_2O_3, $LiAlO_x$, ZrO_2, $AlPO_4$ and LiPON, and electrolyte additives, including 3-hexylthiophene and lithium difluoro (oxalato)borate, on the elimination of the voltage fade in $0.5Li_2MnO_3{\cdot}0.5LiNi_{0.375}Mn_{0.375}Co_{0.25}O_2$ and suggested that these methods, especially LiPON coating, are very effective in improving capacity retention during cycling, but have a very limited or even no effect on voltage fade.

Other approaches, especially those aiming at the changes in the bulk of LLRO particles, have attracted more attention. By limiting the upper cut-off voltage and the amount of excess Li,

Table 4 Representatives of reported effective electrolyte additives for Li-rich oxides

Electrodes	Additives	Base electrolyte (1 M $LiPF_6$)	Functions	1st dis-capacity (mA h g^{-1})	Cycling performance	Year
$Li_{1+x}[Ni_{1/3}Co_{1/3}Mn_{1/3}]_{0.9}O_2$	TPFPB	1.2 M $LiPF_6$, EC : PC : DMC 1 : 1:3	Film-former	—	—	2006[265]
$Li_{1.1}Ni_{0.3}Mn_{0.3}Co_{0.3}O_2$// MCMB	LiBOB	1.2 M $LiPF_6$, EC : PC : DMC 1 : 1:3	Film-former	—	~84%, 100 cycles	2007[266]
$Li_{1.1}Ni_{0.3}Mn_{0.3}Co_{0.3}O_2$// MCMB	VEC		Film-former	—	~90%, 100 cycles	2007[266]
$Li_{1.1}Ni_{0.3}Mn_{0.3}Co_{0.3}O_2$// MCMB	LiDFOB		Film-former	—	~95%, 100 cycles	2007[266]
Li-Rich NMC//graphite	LiDFOB	1.2 M $LiPF_6$, EC : EMC 3 : 7	Film-former	200 (1C, 2.0–4.8 V)	92%, 100 cycles	2012[267]
$Li_{1.2}Mn_{0.56}Ni_{0.16}Co_{0.08}O_2$	HFiP	EC : DMC 1 : 1	Film-former	250 (18 mA g^{-1}, 2.0–4.6 V)	73.3%, 180 mA g^{-1}, 130 cycles	2012[274]
$Li_{1.2}Mn_{0.54}Ni_{0.13}Co_{0.13}O_2$	$Py_{14}TFSI$	EC : DMC 1 : 1	Film-former	~250 (C/10, 2.0–4.8 V)	84.4%, 1C, 150 cycles,	2012[331]
$Li_{1.2}Mn_{0.54}Ni_{0.13}Co_{0.13}O_2$	TMP	EC : DMC 1 : 1	Film-former	270 (C/10, 2.5–4.8 V)	82%, 0.5C, 100 cycles,	2013[332]
$Li_{1.167}Ni_{0.233}Co_{0.1}Mn_{0.467}$-$Mo_{0.033}O_2$	TEP/TPP/ EDP	EC : FEC : EMC : DMC 1 : 2:2 : 5	Oxygen scavenger	—	56%, 300 cycles	2013[276]
$Li_{1.2}Mn_{0.54}Ni_{0.13}Co_{0.13}O_2$	TMSP	EC : DMC 1 : 1	Film-former	247.7 (20 mA g^{-1}, 2.0–4.8 V)	91%, 50 cycles	2014[333]
$Li_{1.2}Mn_{0.54}Ni_{0.13}Co_{0.13}O_2$	TMSB	EC : EMC : DMC 3 : 5:2	Film-former	~270 (C/10)	74%, 0.5C, 200 cycles	2015[334]
Lithium-rich-NMC//graphite	TTFP	EC : DMC 1 : 1	Film-former; oxygen scavenger	192 (4th cycle, 1C, 2.0–4.6 V)	83%, 100 cycles	2015[275]
$Li_{1.17}Ni_{0.17}Mn_{0.5}Co_{0.17}O_2$	TMSP	EC : EMC : DMC 3 : 4:3	Film-former	~250 (C/10, 2.0–4.6 V)	77.1%, C/2, 90 cycles,	2015[273]
$Li_{1.17}Ni_{0.17}Mn_{0.5}Co_{0.17}O_2$// graphite	TMSP	EC : EMC : DMC 3 : 4:3	Film-former	~250 (C/10, 2.0–4.6 V)	87.1%, C/2, 100 cycles,	2015[273]
$Li_{1.2}Mn_{0.56}Ni_{0.16}Co_{0.08}O_2$	SUN	EC : DMC 1 : 1	Film-former	265 (C/10, 2.0–4.8 V)	77.4%, 180 mA g^{-1}, 200 cycles	2015[335]
Li-Rich NMC	PS	EC : DMC 1 : 1	Film-former	275 (C/10, 2.0–5.0 V)	88.4%, C/5, 240 cycles	2015[270]
$Li_{1.16}[Mn_{0.75}Ni_{0.25}]_{.884}O_2$	FEC	EC : DMC : DEC 1 : 1:1	Film-former	198 (C/2, 2.5–4.7 V)	92.5% 100 cycles	2015[336]
$Li_{1.2}Mn_{0.54}Ni_{0.13}Co_{0.13}O_2$	EGBE	EC : EMC 3 : 7	Film-former	~200 (C/2, 2.0–4.8 V)	89%, C/2, 150 cycles	2016[337]
$Li_{1.2}Mn_{0.54}Ni_{0.13}Co_{0.13}O_2$// graphite	TMSPi	EC : EMC : DEC 3 : 5:2	Film-former	209 (C/2, 2.0–4.8 V)	83%, 50 cycles	2016[271]
$Li_{1.2}Mn_{0.54}Ni_{0.13}Co_{0.13}O_2$	PVS	EC : EMC : DMC 3 : 5:2	Film-former	207 (C/2, 2.0–4.8 V)	80%, 240 cycles	2016[269]
$Li_{1.2}Mn_{0.54}Ni_{0.13}Co_{0.13}O_2$	DMAc	EC : EMC : DMC 3 : 5:2	Film-former	246 (C/2, 55 °C)	66.7%, 150 cycles	2016[338]
$Li_{1.16}Ni_{0.2}Co_{0.1}Mn_{0.54}O_2$	TPPi	EC : EMC 1 : 2	Film-former	~250 (C/10, 2.0–4.8 V)	91.2%, C/2, 90 cycles	2016[272]
$Li_{1.2}Mn_{0.56}Ni_{0.16}Co_{0.08}O_2$// graphite	PS/SB	EC : DMC 1 : 1	Film-former	~130 (full cell mass)	85%, 485 cyces	2016[339]
$0.5Li_2MnO_3{\cdot}0.5Li$-$Ni_{0.4}Co_{0.2}Mn_{0.4}O_2$	TMSOMs	EC : EMC 1 : 2	F^- scavenging	~230 (C/10, 2.0–4.6 V)	92.8%, 100 cycles	2016[340]
$Li_{1.17}Ni_{0.17}Mn_{0.5}Co_{0.17}O_2$	LiDFBP	EC : EMC : DMC 3 : 4:3	Film-former	~240 (C/10, 2.0–4.6 V)	99.5%, C/2, 100 cycles	2017[341]
$Li_{1.2}Mn_{0.54}Ni_{0.13}Co_{0.13}O_2$	HTN	EC : DMC 1 : 2	Film-former	~198 (C/2, 2.0–4.8 V)	92.3%, 150 cycles	2017[342]
$Li_{1.2}Mn_{0.54}Ni_{0.13}Co_{0.13}O_2$	TEP	EC : DMC 1 : 2	Film-former; Oxygen scavenger	213 (0.3C, 2.0–4.8 V)	82.6%, 100 cycles	2017[277]
$Li_{1.17}Ni_{0.17}Mn_{0.5}Co_{0.17}O_2$// SGC	LiFMDFB	1.3 M $LiPF_6$, EC : EMC : DMC 3 : 4:3	Film-former	—	85%, 100 cycles	2018[343]
$Li_{1.2}Ni_{0.2}Mn_{0.6}O_2$	bisTMSA	EC : DEC 1 : 1	Removing H_2O	237 (C/10, 2.0–4.8 V)	80%, 1C (171 mA h g^{-1}), 374 cycles	2018[344]
$Li_{1.2}Mn_{0.54}Ni_{0.13}Co_{0.13}O_2$	TPB	EC : EMC : DEC 3 : 5:2	Film-former	~230 (C/10, 2.0–4.8 V)	78%, C/2, 250 cycles	2018[268]
$Li_{1.16}Ni_{0.2}Co_{0.1}Mn_{0.54}O_2$	MDP	EMC : EC 1 : 2	Film-former	~290 (C/10, 50 °C, 2.0–4.8 V)	93.9%, 1C, 80 cycles	2018[345]
$Li_{1.2}Mn_{0.55}Ni_{0.15}Co_{0.1}O_2$	BTMSC	EC : EMC : DEC 3 : 5:2	Eliminating HF	250 (C/10, 2.0–4.8 V)	72%, C/2, 200 cycles	2019[346]

Croy *et al.*[350] observed that the voltage fade becomes worse with the increase of Li_2MnO_3 content. Coupling with the XAS data, they further proposed that maximizing Mn–Ni interactions, minimizing Mn–Mn interactions, limiting the excess Li content and the extent of electrochemical activation could be viable to improve the rate capability and mitigate the voltage fade phenomenon. Aurbach's group[287] demonstrated that substituting/doping $Li_{1.2}Ni_{0.16}Mn_{0.56}Co_{0.08}O_2$ with Al could reduce the voltage degradation from 0.15 V to 0.07 V (average discharge voltage, 100 cycles). Very recently, Kang and co-workers have confirmed that improving the reversibility of TM migration rather than inhibiting this process is also effective in eliminating voltage fade.[351] *Via* an ion exchange method, they prepared an O2-type layered $Li[Li_xNi_yMn_{1-x-y}]O_2$ (LLNMO) compound with the ABBA stacking sequence (Fig. 15a, top), which is different from the conventional O3-type LLNMO with ABCABC stacking (Fig. 15b, top). The connection between the neighboring LiO_6 octahedra and TMO_6 octahedra in the O2-type structure (Fig. 15a, bottom) differs from that in the O3-type structure (Fig. 15b, bottom), which leads to the high reversibility of TM migration in O2-type LLNMO (Fig. 15c and d) and results in the suppressed voltage fade in the O2-type LLNMO electrode (Fig. 15e). After 40 cycles,

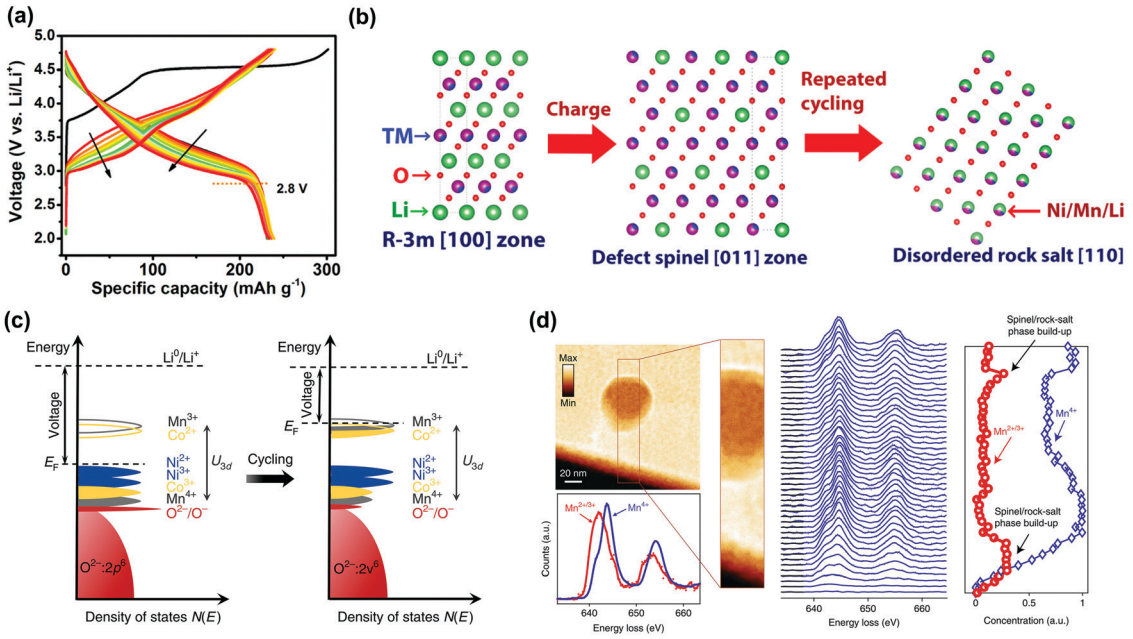

Fig. 14 Voltage fade in LMROs. (a) The evolution of the charge/discharge profile of $Li_{1.2}Ni_{0.2}Mn_{0.6}O_2$ in the voltage range of 2.0–4.8 V, clearly displaying the voltage fade phenomenon.[141] (b) Illustration of structural evolution of $Li_{1.2}Ni_{0.2}Mn_{0.6}O_2$ during cycling.[141] (c) The illustration of Fermi level changes of LMROs during cycling, showing that the evolution of redox couples is the direct cause of voltage fade.[187] (d) STEM-EELS mapping of a concealed pore in a cycled $Li_{1.2}Ni_{0.5}Co_{0.1}Mn_{0.55}O_2$ electrode indicating that a spinel-like phase appears in the bulk of the electrode.[187] Reproduced with permission,[141] Copyright 2015, Royal Society of Chemistry. Reproduced with permission,[187] Copyright 2018, Nature Publishing group.

the retention of energy density is increased from 71.8% for O3-type LLNMO to 82.5% for O2-type LLNMO. By a modified co-precipitation method, Zhang *et al.*[352] obtained the $Li_{1.2}Ni_{0.2}Mn_{0.6}O_2$ compound with dispersed spherical secondary particles, which exhibits substantially suppressed voltage fade as compared to the one obtained with the conventional co-precipitation method. He *et al.*[353] also prepared $Li_{1.2}Mn_{0.56}Ni_{0.16}Co_{0.08}O_2$ *via* a template assisted method; this material showed a porous morphology integrated with an *in situ* formed surface containing carbonaceous compounds. The voltage decay was only 0.084 V (100 cycle) when investigated in the voltage range of 2.0–4.8 V. Although the underlying mechanisms should be further explored and O2-structured LROs still exhibit low cycling stability, their work shows that adopting suitable synthesis methods might be promising to mitigate the voltage fade issue.

From the above analysis and discussion, it can be concluded that voltage decay/fade is closely related to structural changes in the bulk of the materials, and thus strategies such as stoichiometry optimization, element substitution/doping, structural design, and morphology tailoring show great promise in mitigating voltage decay.

3.5.3 Voltage fade in DLROs. For DLROs, voltage fade and capacity decay that have been discussed in Section 3.4 are two major challenges during cycling. As discussed in Section 3.5.2, the direct reason for voltage fade in LLROs is the transformation from high voltage redox couples to low voltage redox couples,[187] while the underlying mechanisms are very complex and involve many features, such as LS transition, TM migration, and continuous oxygen release. However, except for the densified layers (Fig. 13b), the structural evolution of DLROs is difficult to detect due to their complex structural characteristics, which brings difficulties in the mechanistic studies of voltage fade in DLROs. Kan *et al.*[209] observed that during the discharge process of $Li_{1.3}Nb_{0.3}Mn_{0.4}O_2$, the reaction peak located at ~3.2 V degrades rapidly, while the reduction reaction at ~2.2 V increases with cycling, indicating the occurrence of redox reactions involving different Mn species. Chen *et al.* further studied the change of the Mn valence-state in $Li_{1.3}Nb_{0.3}Mn_{0.4}O_2$ electrodes cycled in different voltage ranges.[210] They found no obvious increase of Mn^{2+} in discharged electrodes cycled five times compared to pristine when cycled within 1.5–4.2 V. However, when the upper cut-off voltage increased to 4.8 V, the amount of Mn^{2+} increased with cycling, which suggests that the Mn reduction during cycling is induced owing to the anionic reactions above 4.2 V. The reduction of the TM ions with cycling in anionic redox active DLROs has been clearly observed[210,354] and should obviously be related to the voltage fade phenomenon in DLROs. However, the intrinsic causes of the TM reduction and their detailed connection with electrochemical performances are rarely studied.

4. Oxygen redox in Na-cathodes

The first cathode materials for sodium ion batteries (NIBs) were reported in the early 1980s, shortly after those for LIBs.[355] However, because of their inferior electrochemical performance, NIBs received less attention as compared with their lithium counterparts. The fervor for developing NIBs has been revived

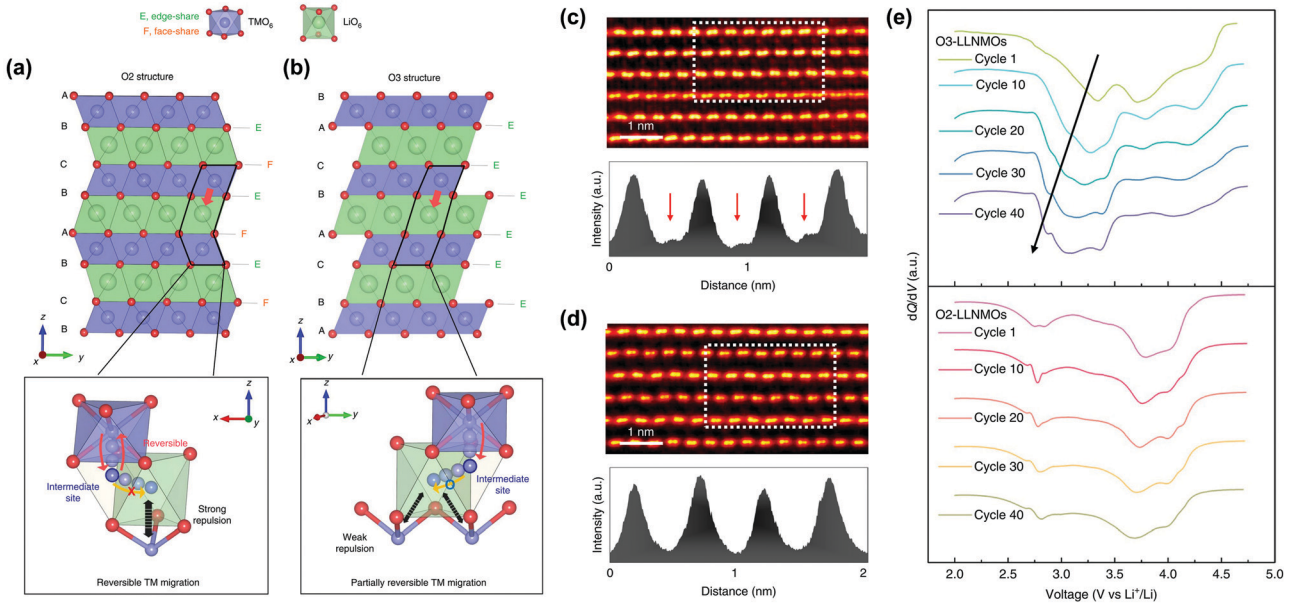

Fig. 15 Schematic illustration of crystal structures and TM migration paths of (a) O2-type LLNMO and (b) O3-type LLNMO. HAADF-STEM images of O2-LLNMO at (c) 4.8 V charged state and (d) 2.0 V discharged state. Bright dots appear in Li layers at 4.8 V and disappear at 2.0 V indicating the high reversibility of TM migration during the charge and discharge processes. (e) Comparison of discharge dQ/dV curves of O3-type (top) and O2-type (bottom) LLNMO electrodes along cycling.[351] Reproduced with permission,[351] Copyright 2020, Nature Publishing group.

owing to the higher natural abundance of sodium than lithium and the considerable achievements made in advanced NIB electrode materials, in particular cathode materials.[356–361] In comparison with Li^+, although the heavier weight and larger ionic radius of Na^+ (1.02 Å for Na^+ *vs.* 0.76 Å for Li^+) slow down Na^+ migration, the lower charge density of Na^+ leads to a weaker interaction between charge carriers and lattice oxygen, thus resulting in a higher mobility of Na^+ in layered oxides.[362,363] Therefore, some layered sodium oxides exhibit good rate capability in appropriate voltage ranges.[364,365] However, the higher standard reduction potential of Na (−2.71 V *vs.* SHE) than Li (−3.04 V *vs.* SHE) results in the lower operative potential of sodium ion cathodes than their Li counterparts.[366] Compared to their lithium counterparts, the layered sodium transition metal oxides ($Na_xTM_yO_2$, $x + y \leq 2$) show decreased specific capacity, versatile layered structures, and more irreversible phase changes during sodium insertion/extraction.[367] To address the low energy density and thus high cost per kWh caused by the above-mentioned factors and to increase the commercial viability of NIBs, high capacity sodium ion cathodes with both cationic and anionic redox reactions came into the radar. Up to now, anionic redox reactions have been found in an enormous number of $Na_xTM_yO_2$ materials, as shown in Table 5. Unlike layered lithium transition metal oxides, for which the anionic redox that provides extra capacities beyond the TM redox is usually triggered by the excess lithium ions, it is very interesting that all of the sodium ions can be extracted from $Na_xTM_yO_2$, no matter how much charges are compensated by TM redox reactions, which indicates the easy activation of the lattice oxygen redox reactions. Besides, the lattice oxygen redox in $Na_xTM_yO_2$ is more reversible than that in LLROs.[77]

Based on the stoichiometry of the chemical formula ($Na_xTM_yO_2$), anionic redox reactions have been found in both Na-rich ($x > 1$) and Na-poor ($x < 1$) oxides. It is still a mystery that most of the Na-rich oxides are based on 4d (such as Na_2RuO_3, Na_3RuO_3) and 5d (such as Na_2IrO_3) TM ions. One possible explanation is the large difference in ionic radii between Na^+ and other 3d TM ions. For example, the ionic radius of Na^+ (1.02 Å) is 1.92 times that of Mn^{4+} (0.53 Å), which leads to the strong tendency of the Na^+ ions to be located in the sodium layers instead of the TM layers. However, ratios of ionic radii between Na^+ and Ir^{4+} (0.63 Å, 1.62 times), Ru^{3+} (0.62 Å, 1.64 times), and Ru^{4+} (0.68 Å, 1.50 times) lie also too much above the critical value of 1.15 to form solid-solution structures. Therefore, the critical reasons that constrain the synthesis of 3d-based Na-rich oxides need to be further uncovered. Besides Na-rich oxides, the lattice oxygen redox is widely identified in Na-poor oxides containing 3d TMs, such as P2-type $Na_{0.67}Mg_{0.33}Mn_{0.67}O_2$[77] and $Na_{0.67}Zn_{0.2}Mn_{0.8}O_2$,[391] as shown in Table 5. In this section, the recent advances and reaction mechanisms of anionic redox in layered Na-rich and Na-poor materials will be reviewed.

4.1 Lattice oxygen redox in Na-rich oxides

Layered Na_2RuO_3 (space group: $R\bar{3}m$) is the first reported Na-rich oxide that can be used as the cathode for NIBs.[392] The capacity delivered by Na_2RuO_3 within 1.5–4.0 V is 147 mA h g^{-1}, which is only 7% higher than the theoretical capacity based on the Ru^{4+}/Ru^{5+} redox couple. Two years later, Rozier *et al.*[113] found that the $Na_2Ru_{1-y}Sn_yO_3$ series could (de)intercalate more Na^+ per formula unit than the amount of charge compensated by the Ru^{4+}/Ru^{5+} redox couple. They proposed the involvement of anionic (Ru^{4+}/Ru^{5+})

Table 5 List of reported layered sodium oxides with anionic redox reactions

Materials	Structures	1st dis-capacity (mA h g^{-1})	Cycle performance	Redox center	O_2 release	Year
Na-Rich oxides						
$Na_2Ru_{0.75}Sn_{0.25}O_3$	Layered	~142 (1.5–4.2 V)	~71%, 50 cycles	Ru, O	—	2015[113]
Na_2IrO_3	Layered ($C2/m$)	~133 (C/5, 1.5–4 V)	~45%, 50 cycles	Ir, O	Yes	2016[368]
Na_2RuO_3	Layered ($R\bar{3}m$)	~180 (30 mA g^{-1}, 1.5–4.0 V)	~87%, 50 cycles	Ru, O	—	2016[72]
Na_3RuO_4	Layered ($C2/m$)	~130 (50 mA g^{-1}, 1.5–4.0 V)	~46%, 50 cycles	O	—	2018[369]
$Na_{1.2}Mn_{0.4}Ir_{0.4}O_2$	Layered ($R\bar{3}m$)	~140 (20 mA g^{-1}, 1.5–4.4 V)	>60%, 100 mA g^{-1}, 50 cycles	Mn, O	No	2019[370]
Na-poor oxides						
$Na_{2/3}Mg_{0.28}Mn_{0.72}O_2$	Layered	~220 (10 mA g^{-1}, 1.5–4.4 V)	>68%, 30 cycles	Mn, O	—	2014[371]
$Na_{0.78}Li_{0.18}Ni_{0.25}$-$Mn_{0.583}O_w$	Layered	~240 (125 mA g^{-1}, 1.5–4.5 V)	190 mA h g^{-1}, 30 cycles	Mn, O	—	2015[372]
$Na_{0.6}Li_{0.2}Mn_{0.8}O_2$	Layered	~80 (0.1C, 3.5–4.5 V)	50%, ~10 cycles	O	—	2018[109]
$Na_{2/3}Mg_{0.28}Mn_{0.72}O_2$	Layered	~160 (10 mA g^{-1}, 1.5–4.5 V)	—	Mn, O	No	2018[74]
$Na_{2/3}Mn_{7/9}Zn_{2/9}O_2$	Layered ($P6_3/mmc$)	~195 (0.1C, 1.5–4.5 V)	>60%, 50 cycles	Mn, O	No	2018[373]
$Na_{0.5}Ni_{0.25}Mn_{0.75}O_2$	Layered ($R\bar{3}m$)	180 (20 mA g^{-1}, 1.5–4.6 V)	—	Ni, O	—	2018[374]
$Na_{4/7}Mn_{6/7}O_2$	Layered ($P\bar{1}$)	~200 (0.05C, 1.5–4.7V)	85%, 20 cycles	Mn, O	—	2018[375]
$Na_{4/7}Mn_{6/7}O_2$	Layered ($P\bar{1}$)	~220 (—, 1.5–4.4V)	68%, 20 cycles	Mn, O	—	2018[376]
$Na_{2/3}Ni_{1/3}Mn_{2/3}O_2$	Layered ($P6_3/mmc$)	228 (10 mA g^{-1}, 1.5–4.5 V)	40%, 100 cylces	Ni, surface Mn, O	No	2018[377] 2020[378,379]
$Na_{2/3}Mg_{1/3}Mn_{2/3}O_2$	Layered	168 (0.1C, 2.0–4.5 V)	~80%, 1C, 100 cycles	Mn, O	—	2019[77]
$Na_{0.653}Mn_{0.929}O_2$	Layered ($P6_3/mmc$)	~210 (0.1C, 1.5–4.3 V)	~86%, 60 cycles	Mn, O	—	2019[380]
$Na_{2/3}Mg_{1/3}Ti_{1/6}Mn_{1/2}O_2$	Layered ($P6_3/mmc$)	~230 (20 mA g^{-1}, 1.5–4.3 V)	~70%, 40 mA g^{-1}, 50 cycles	O	—	2019[381]
$Na_{0.72}Li_{0.24}Mn_{0.76}O_2$	Layered ($P6_3/mmc$)	~270 (10 mA g^{-1}, 1.5–4.5 V)	~55%, 30 cycles	O	—	2019[382]
$Na_{0.66}Li_{0.18}Fe_{0.12}Mn_{0.7}O_2$	Layered ($P6_3/mmc$)	~190 (10 mA g^{-1}, 1.5–4.5 V)	~87%, 80 cycles	Mn, Fe, O	—	2019[383]
$Na_{0.66}Li_{0.22}Ti_{0.15}Mn_{0.63}O_2$	Layered ($P6_3/mmc$)	228 (10 mA g^{-1}, 1.5–4.5 V)	83.6%, 50 mA g^{-1}, 100 cycles	Mn, O	Yes	2019[384]
$Na_{0.6}Mg_{0.2}Mn_{0.6}Co_{0.2}O_2$	Layered ($P6_3/mmc$)	214 (26 mA g^{-1}, 1.5–4.6 V)	87%, 100 cycles	Co, O	—	2019[385]
$Na_{2/3}Mg_{1/3}Mn_{2/3}O_2$	Layered ($R\bar{3}m$)	225 (7.5 mA g^{-1}, 1.6–4.4 V)	~65%, 15 mA g^{-1}, 30 cycles	Mn, O	—	2019[386]
$Na_{0.9}Ni_{0.5}Mn_{0.5}O_2$	Layered ($R3m$)	102 (100 mA g^{-1}, 1.5–4.5 V)	78%, 100 mA g^{-1}, 500 cycles	Ni, O	—	2019[387]
$Na_{0.66}Li_{0.22}Ru_{0.78}O_2$	Layered ($P6_3/mmc$)	158 (10 mA g^{-1}, 1.5–4.5 V)	91%, 50 mA g^{-1}, 500 cycles	Ru, O	—	2020[388]
$Na_{0.67}Ni_{0.33}Mn_{0.66}Sn_{0.01}O_2$	Layered ($P6_3/mmc$ & $R3m$)	245 (20 mA g^{-1}, 1.5–4.5 V)	73%, 200 mA g^{-1}, 50 cycles	Ni, Mn, O	—	2020[389]
$Na_{2/3}Mn_{0.72}Cu_{0.22}Mg_{0.06}O_2$	Layered ($P6_3/mmc$)	108 (17.4 mA g^{-1}, 2.0–4.5 V)	87.9%, 174 mA g^{-1}, 100 cycles	Mn, Cu, O	—	2020[390]

and cationic (O^{2-}/O^{n-}) redox mechanisms based on their XPS results.[113] Focusing on the discrepancy of anionic redox, Boisse *et al.* discovered the relationship between the local structure and anionic redox reactions of Na_2RuO_3, as shown in Fig. 16a.[72] For the honeycomb-ordered Na_2RuO_3, Na^+ is extracted from the TM layers prior to the Na layers and leaves $[\square_{1/3}Ru_{2/3}]$ ordering in the TM layers. The short O–O distance in the $[\square_{1/3}Ru_{2/3}]$ structure raises the energy level of the antibonding σ^* orbital of the O–O bond close to the Fermi level and thus triggers the oxygen redox reactions. In contrast, the O–O distance in the disordered Na_2RuO_3 is too long to activate anionic redox. Furthermore, after studying the charge compensation in Na_3RuO_4, Zhou's group[369] demonstrated that it is lattice oxygen redox that is responsible for the very high initial charge capacity of 321 mA h g^{-1} since Ru is already in the high valence state of 5+ in the pristine material. More importantly, they observed the superoxide signal at the very initial stage of the charge process by *in situ* Raman spectroscopy (Fig. 16b), indicating that the oxidation of lattice oxygen does not follow the rigid gradual steps of $O^{2-} \rightarrow O^- \rightarrow O_2^- \rightarrow O_2$. For Ru^{4+}-based materials, the oxidation of Ru^{4+} and lattice oxygen reactions are usually decoupled and appear in the low

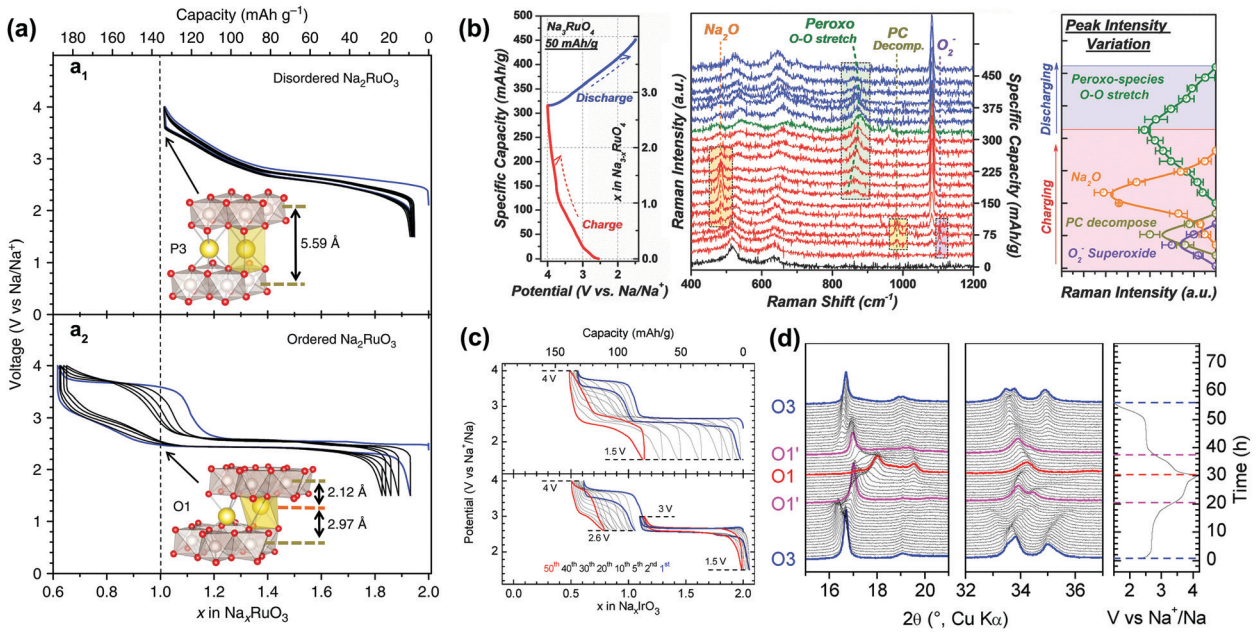

Fig. 16 Lattice oxygen redox in layered Na-rich transition metal oxides. (a) Charge/discharge curves of disordered (a_1) and ordered (a_2) Na_2RuO_3 in the voltage range of 1.5–4.0 V.[72] (b) *In situ* Raman spectra of Na_3RuO_4 during the initial cycle suggest the formation of peroxo-species.[369] (c) Charge/discharge curves of Na_2IrO_3 at different cycles within different voltage ranges of 1.5–4.0 V, 1.5–3.0 V and 2.6–4.0 V.[368] (d) *In situ* XRD patterns of Na_2IrO_3 in the voltage range of 1.5–4.3 V.[368] Reproduced with permission,[72] Copyright 2016, Nature Publishing group. Reproduced with permission,[369] Copyright 2018, Royal Society of Chemistry. Reproduced with permission,[368] Copyright 2016, American Chemical Society.

and high potential ranges, respectively. It is different in the case of Ir-based materials. The first charge plateau of Na_xIrO_3 with $2.0 > x > 1.0$ is related to the combination of $Ir^{4+/5+}$ and oxygen redox (Fig. 16c), while oxygen redox alone contributes to the charge-compensation of the second charge plateau ($1.0 > x > 0.5$).[368] Although Perez *et al.* proposed that the large delocalization of the 5d orbitals enables a greater overlap with O 2p orbitals as compared to 3d or 4d metals, which leads to strong covalent Ir–O bonds that block Ir migration and inhibit O_2 evolution, and the cycling stability of Na_2IrO_3 at 1.5–4.0 V is still limited due to the structural transition of O3–O1′, as shown in Fig. 16d.

4.2 Lattice oxygen redox in Na-poor oxides

3d TM-based $Na_xTM_yO_2$ materials have been widely investigated due to the successful application of their lithium counterparts. Up to now, lattice oxygen redox reactions have been identified in a wide range of layered Na-poor Mn-based $Na_xTM_yO_2$ ($x < 1$), as shown in Table 5.

Among them, Li substituted Na_xMnO_2 oxides show promise as cathodes for NIBs due to their high capacity and great stability. In 2014, Komaba's group reported that $Na_{5/6}Li_{1/4}Mn_{3/4}^{3.88+}O_2$ delivers a high reversible capacity of ~200 mA h g^{-1} in the voltage range of 1.5–4.4 V.[393] In the following year, Liu *et al.* prepared an O3-type $Na_{0.78}Li_{0.18}Ni_{0.25}Mn_{0.583}O_w$ ($0 < w < 2$) compound by an ion-exchange process, which delivers an even higher discharge capacity of 240 mA h g^{-1} in the voltage range of 1.5–4.5 V.[372] Later on, De la Llave *et al.* found that Li substituted $Na_{0.6}Li_{0.2}Mn_{0.8}^{4+}O_2$ exhibits not only a higher specific capacity of 190 mA h g^{-1} but also better cycling stability as compared to $Na_{0.6}MnO_2$ in the voltage range of 2.0–4.6 V.[394] More recently, as shown in Fig. 17a, Rong *et al.*[382] have reported an $Na_{0.72}Li_{0.24}Mn_{0.76}^{4+}O_2$ electrode which delivers the highest discharge capacity (~270 mA h g^{-1}, 1.5–4.4 V) and energy density (~700 W h g^{-1}, based on the mass of the positive electrode material) among the known $Na_xTM_yO_2$ oxides by then, although the cycling performance needs to be further improved (Fig. 17b). The high discharge capacity delivered by these kinds of electrodes should be attributed to the combination of the $Mn^{3+/4+}$ redox couple and lattice oxygen redox reactions, but the possibility of Li^+ extraction from the TM layers and the reversibility of the Li^+ (de)intercalation process are still unclear. To clarify these issues, the solid state nuclear magnetic resonance (ss-NMR) technique has been applied due to its high sensitivity to local environments and the capability of tracking the target ions in real time. As shown in Fig. 17c, the Li^+ at different local environments of the surface (0 ppm), Na layers (~750 ppm), TM layers (~1750 ppm), and TM layers with more distorted coordination (2100 ppm) can be well distinguished by ^{7}Li MAS ss-NMR.[395] According to the ^{7}Li spectra at different states and different cycles of $Na_{0.6}Li_{0.2}Mn_{0.8}O_2$ electrodes (Fig. 17c), it can be concluded that (i) during the charging process, the Li^+ ions in the TM layers move into the Na layers, (ii) the Li^+ ions can move out of the particles during cycling, and (iii) the Li^+ ions can return to the transition metal layer during discharge, but there is Li^+ loss, which is detrimental to structural stability.

From the results of oxygen K-edge sXAS and RIXS, Maitra *et al.*[74] confirmed the participation of the lattice oxygen redox in the charge compensation mechanism of $Na_{2/3}Mg_{0.28}Mn_{0.72}O_2$.

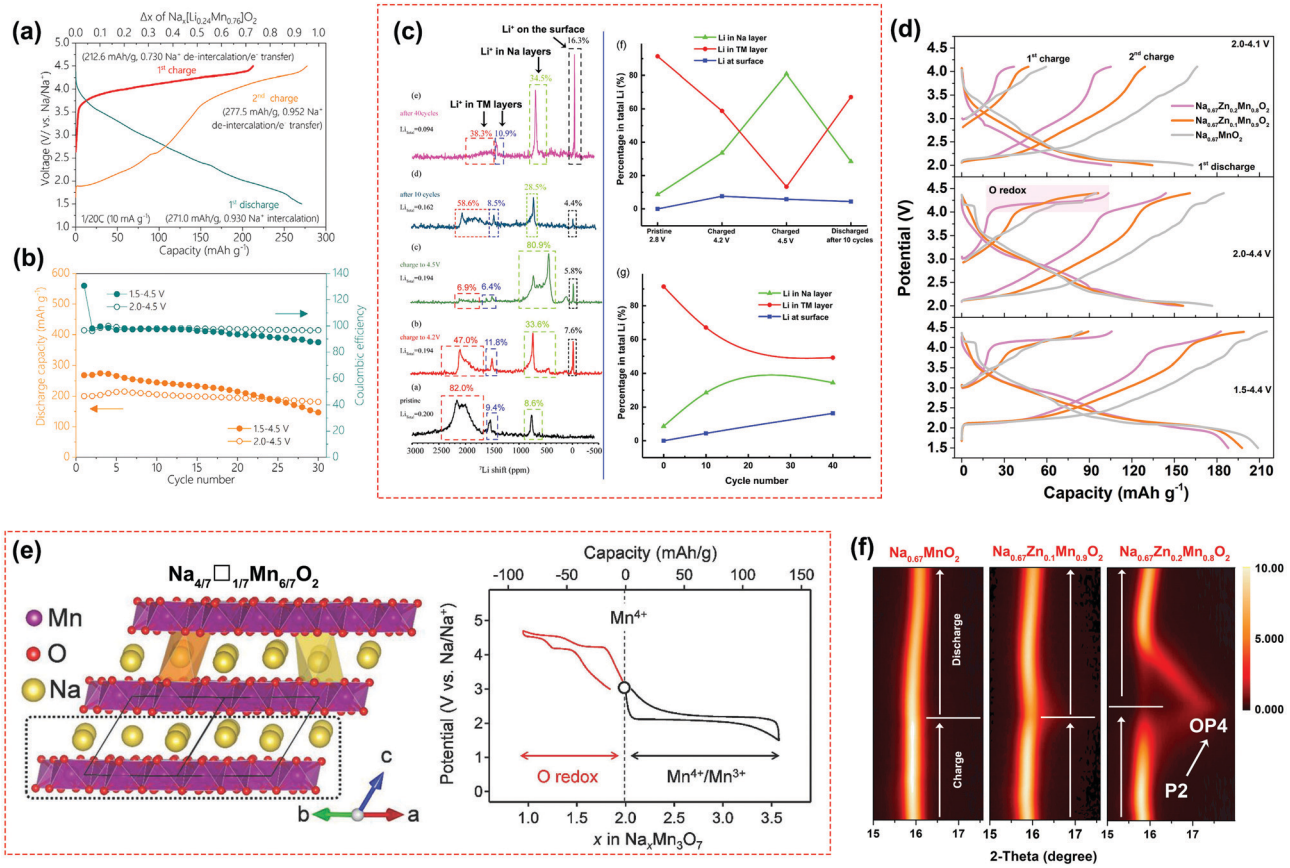

Fig. 17 Lattice oxygen redox in layered Na-poor transition metal oxides. (a) Charge/discharge curves and (b) cycling performance of the $Na_{0.72}Li_{0.24}Mn_{0.76}O_2$ electrode.[382] (c) ^{7}Li ss-NMR spectra of $Na_{0.6}Li_{0.2}Mn_{0.8}O_2$ during cycling show the extraction of Li^+ ions from TM layers.[395] (d) Charge/discharge curves of $Na_{0.67}Zn_xMn_{1-x}O_2$ electrodes in different voltage ranges clearly indicate that the capacity delivered by lattice oxygen redox increases with the increase of Zn content (x).[391] (e) Structure and charge-compensation mechanisms of $Na_{4/7}\square_{1/7}Mn_{6/7}O_2$.[375] (f) *In situ* XRD patterns of $Na_{0.67}Zn_xMn_{1-x}O_2$ (x = 0, 0.1, 0.2) electrodes with the evolution of (002) reflections in the first cycle.[391] Reproduced with permission,[382] Copyright 2019, Elsevier. Reproduced with permission,[395] Copyright 2018, Elsevier. Reproduced with permission,[391] Copyright 2020, Elsevier. Reproduced with permission,[375] Copyright 2018, Wiley-VCH.

More importantly, unlike most of the LROs, no oxygen release was observed in the charge and discharge processes of $Na_{0.67}Mg_{0.28}Mn_{0.72}O_2$ because no cations migrated from the TM layers and thus oxygen ions are always stabilized by the coordination environment of at least three cations.[74] Their results also suggested that excess alkali ions are not always necessary to activate the oxygen redox reaction, at least not in layered Mn-based $Na_xTM_yO_2$ oxides. Based on XPS results, Rozier's group reported that the oxygen redox activities in $Na_{2/3}Mn_{7/9}Zn_{2/9}O_2$ originated from the highly covalent $Zn^{2+}(3d^{10})$–O(2p) bonds.[373] Generally, with an increase in the amount of electrochemically inert elements, the reversible capacity of a Mn based $Na_xTM_yO_2$ material delivered within 2.0–4.0 V declined because of the decreased active Mn sites, while the oxygen redox reactions in the voltage range of ~4.0–4.5 V increased, as demonstrated for the Mg-substituted $Na_{0.67}Mg_xMn_{1-x}O_2$ and Zn-substituted $Na_{0.67}Zn_xMn_{1-x}O_2$ materials (Fig. 17d).[371,391,396] In other words, the lattice oxygen redox can be brought about by intentionally increasing the Mn valence state in the pristine component, *e.g.* by doping/substituting with low-valence-state elements or by introducing transition metal vacancies. Yamada's group[375] observed a highly reversible oxygen redox at ~4.1 V in $Na_{4/7}\square_{1/7}Mn_{6/7}O_2$ ($\square$ stands for Mn vacancies), whose XRD pattern indicated that the arrangement of $\square$-Mn forms a $\sqrt{7} \times \sqrt{7}$ superlattice, as shown in Fig. 17e. Nearly at the same time, Li *et al.*[376] reported similar results and demonstrated that the structural evolution of this material during charge and discharge is negligible.

Although the oxygen redox reactions in $Na_xTM_yO_2$ do provide extra capacities beyond TM redox, many challenges still hinder their practical application, such as parasitic side reactions at the surface and interface of the electrolyte, large potential/voltage hysteresis, and poor cycling stability. The oxygen redox reactions in $Na_xTM_yO_2$ especially in Na-poor oxides usually occur in the voltage range of 4.0–4.5 V *vs.* Na/Na^+ (4.3–4.8 V *vs.* Li/Li^+), and rational electrolyte additives and protective coating layers[391] are therefore urgently needed to passivate the interface between the electrode/electrolyte and decrease the decomposition of the organic electrolyte. Very recently, by comparing the electrochemistry, pristine structures, and structural evolution of $Na_{0.75}Li_{0.25}Mn_{0.75}O_2$ and $Na_{0.6}Li_{0.2}Mn_{0.8}O_2$, Bruce's group[397] demonstrated that

the voltage hysteresis is closely related to superstructures in the TM layers. They proved that the voltage hysteresis of honeycomb ordered $Na_{0.75}Li_{0.25}Mn_{0.75}O_2$ resulted from its structural instability (Mn migration), as opposed to ribbon ordered $Na_{0.6}Li_{0.2}Mn_{0.8}O_2$ whose voltage hysteresis in the first cycle was negligible and the structure during cycling remained relatively stable. However, the voltage hysteresis of ribbon ordered $Na_{0.6}Li_{0.2}Mn_{0.8}O_2$ still increased with cycling, and little information was provided on the design of materials with low voltage hysteresis. Furthermore, a large voltage hysteresis of oxygen redox reactions can be clearly observed in $Na_{0.67}Mg_{0.28}Mn_{0.72}O_2$[74] even under the circumstance that the structure of $Na_{0.67}Mg_{0.28}Mn_{0.72}O_2$ during charge is much more stable than the ribbon ordered $Na_{0.6}Li_{0.2}Mn_{0.8}O_2$. Therefore, it appears to be still a long future journey to resolve the origin of voltage hysteresis of lattice oxygen redox reactions in $Na_xTM_yO_2$ oxides. Irreversible phase transformations during the oxygen redox reactions often lead to poor cycling stability. For example, the formation of a Na-depleted ramsdellite phase with a short coherent length of 30 Å is observed for the deeply de-sodiated P2-$Na_{0.67}Fe_{0.5}Mn_{0.5}O_2$ material, and the poor reversibility of this phase change is responsible for capacity fade.[398] As shown in Fig. 17f, another example is the phase transition of P2–OP4 in the high voltage range, which is related to the oxygen redox reactions in Zn-substituted $Na_{0.67}MnO_2$ electrodes.[391] Specifically, this transition is absent in unsubstituted $Na_{0.67}MnO_2$ and gradually becomes severe with the increase of Zn content. It is important to point out that the contraction of the *c* lattice parameter due to the P2–OP4 phase transition might be an intrinsic feature associated with the oxygen redox reactions in many Na-poor oxides, such as $Na_{0.72}Li_{0.24}Mn_{0.76}O_2$[382] and $Na_{0.67}Mg_{0.28}Mn_{0.72}O_2$.[371]

Compared to LROs, the pristine structures and structural transitions during the charge/discharge of some Na-poor $Na_xTM_yO_2$ compounds are simpler. Therefore, Na-poor $Na_xTM_yO_2$ compounds can be used as models to reveal the intrinsic characteristics of anionic redox reactions. For example, based on $Na_{2/3}Mg_{0.28}Mn_{0.72}O_2$, Bruce's group first found that the oxygen redox reactions that deliver excess capacity beyond cation redox could be performed without excess alkali-metal ions.[74] Moreover, Yang's group quantified the reversibility of the cationic redox reaction in $Na_{2/3}Mg_{1/3}Mn_{2/3}O_2$ electrodes through mRIXS.[77] In combination with the results for the $Li_{1.17}Ni_{0.21}Co_{0.08}Mn_{0.54}O_2$ electrode reported in the same paper, they found that the lattice oxygen redox in both Li-ion and Na-ion systems exhibited high reversibility. Very recently, they have attempted to distinguish the oxygen activities in battery electrodes into two kinds,[218] *i.e.* lattice oxygen redox and irreversible oxygen activities (non-lattice oxygen redox); the latter includes O_2 release, radical oxygen evolution, and surface reactions. Through the quantification and comparison of oxygen redox in $Na_{0.6}Li_{0.2}Mn_{0.8}O_2$ and $Na_{2/3}Mg_{1/3}Mn_{2/3}O_2$, they proposed that lattice oxygen redox is highly reversible and the majority of capacity/voltage decay is aroused by non-lattice oxygen redox reactions.

Another important issue with the oxygen redox systems is the sluggish kinetics, which seems to be intrinsic to the oxygen redox activities and has been considered the most critical issue for practicability.[50] Strikingly, some Na-poor oxides with strong oxygen redox reactions, *e.g.*, $Na_{2/3}Ni_{1/3}Mn_{2/3}O_2$, display negligible voltage hysteresis and a highly reversible electrochemical profile that were found only in conventional systems reported earlier.[378,379] These investigations of oxygen redox and its electrochemical behaviors in layered sodium transition metal oxides, especially Na-poor oxides, provide unique candidates for comparative studies on understanding the reaction mechanisms and structure–performance relationship of LROs, which will enable the new design of advanced electrode materials with high capacity, stability, and kinetics.

5. Characterization techniques

Comprehensive understanding of the structural and chemical evolution of materials during electrochemical processes is of great significance for designing advanced electrode materials. There are three major scientific concerns in the research of LROs: (i) regulating the lattice oxygen redox to a certain extent; (ii) probing bulk and surface structural evolution during cycling; (iii) clarifying the relationship between structure/charge-transfer mechanisms and electrochemical performance. Characterization techniques are essential for the in-depth understanding of these issues.

The cycling stability of electrode materials is closely associated with the pristine structure and structural evolution during electrochemical processes. Many characterization techniques, both *ex situ* and *in situ*/*operando*, have been developed and successfully utilized to analyze the structural issues of electrode materials, such as XRD,[70] ND,[166] X-ray and neutron pair distribution function (XPDF and nPDF),[127] EXAFS,[91] Raman spectroscopy,[89] Mössbauer spectroscopy,[146] ss-NMR,[399] TEM,[168] *etc.* Besides, the charge compensation mechanism plays a key role in understanding the electrochemical behavior of battery electrodes during charge and discharge. The charge transfer process is usually performed by the charge-variable ions, such as TM ions in conventional layered cathode materials and both TM ions and lattice oxygen in LROs. The valence state of the TM ions can be determined by XPS,[108] XAS,[187] Mössbauer spectroscopy,[146] EELS,[188] *etc.* Moreover, the recently developed mRIXS[400] is effective in tracking oxygen redox. The principles, experimental set-ups, and applications of these characterization techniques have been reviewed previously, *e.g.* TEM (STEM/EELS),[45,401] synchrotron-based X-ray techniques (XAS/XRD/PDF/XPS/mRIXS),[111,401,402] and *in situ* techniques (XAS/XRD/PDF/SEM/TEM).[401,403] These previous reviews are highly recommended for our readers. In the following section, we will focus on the present features and future expectations regarding the application of these above-mentioned techniques in the study of LROs.

5.1 XRD, ND and PDF

XRD and ND are powerful and complementary characterization techniques to inspect the structures of well-crystallized electrode materials. They can provide information about purity,

space groups, crystallinity, Li/Ni mixing, oxygen vacancies, and cation orderings based on the positions and relative intensities of XRD/ND reflections. Compared to ND, XRD is more easily accessible because of the widespread lab-sources and *in situ*/*operando* XRD have been therefore widely used to probe structural transformations of LROs during cycling. Moreover, synchrotron-based XRD has high photon energy and extremely bright X-rays, thus having the advantages of high signal intensity, low noise, fast detection, and deep sample penetration. Due to these distinct characteristics, the *in situ* XRD set-up of the synchrotron-source is slightly different to that based on the lab-source (Fig. 18a).[402] Up to now, *in situ* XRD has been applied in the studies of various LROs and $Na_xTM_yO_2$ with anionic redox reactions during electrochemical cycling, such as $LiNi_xLi_{(1/3-x/3)}Mn_{(2/3-x/3)}O_2$,[79] Li_2MnO_3,[118] $Li_{1.2}Mn_{0.61}Ni_{0.18}Mg_{0.01}O_2$,[200] $Li_{1.2}Ni_{0.13}Mn_{0.54}Co_{0.13}O_2$,[70] $Li_{1.2}Co_{0.1}Mn_{0.55}Ni_{0.15}O_2$,[199] $Li_{1.2}Ni_{1/3}Ti_{1/3}Mo_{2/15}O_2$,[151] $Li_2Ru_{0.5}Mn_{0.5}O_2$,[127] Na_2IrO_3,[368] $Na_{0.67}Zn_xMn_{1-x}O_2$,[373,391] $Na_{0.72}Li_{0.24}Mn_{0.76}O_2$,[382] *etc.* It is well known that ND is a scattering technique with very high sensitivity to light elements (such as H, Li, Na, O, F, *etc.*) and to distinguish the neighboring elements (such as Ni, Co, and Mn). Therefore, ND could provide complementary structural information to XRD. However, the application of ND especially its *in situ*/*operando* technique is restricted by two factors: (i) long acquisition time (1–12 h) and a large sample amount (0.5–2 g) are needed due to the low intensity of the neutron beam; (ii) the neutron source and experiment time are very limited and thus precious. Up to now, only a few *operando* ND results have been reported on LROs. In 2013, Liu *et al.*[404] applied *in situ* ND to compare the structural changes between $LiNi_{1/3}Mn_{1/3}Co_{1/3}O_2$ and $Li_{1.2}Ni_{0.18}Mn_{0.53}Co_{0.1}O_2$ by lab-made pouch cells (Fig. 18b). They observed an irreversible volume expansion in $Li_{1.2}Ni_{0.18}Mn_{0.53}Co_{0.1}O_2$ after the first cycle. Three years later,[166] they further investigated the lithium dynamics in high Li-rich and low Li-rich layered oxides by *operando* ND and observed site-dependent lithium ion migration during charge/discharge processes.

A PDF pattern is obtained by Fourier transform of the total scattering from either X-ray (XPDF) or neutron beam (nPDF).[401–403] As shown in Fig. 18c,[405] a PDF pattern provides a probability of finding two atoms at given inter-atomic distances '*r*' and therefore it is able to provide information on bond lengths, coordination numbers, orderliness and particle sizes. Therefore, PDF is one of the handiest tools to probe the structures of electrode materials with high, low, or even no crystallinity, and has been used to investigate a large number of electrode materials, including those involving anionic redox reactions. For example, according to their *ex situ* nPDF results on $Li_xRu_{0.5}Mn_{0.5}O_2$, Lyu *et al.*[127] found that the Ru–Ru dimerization is well preserved with the initial charge/discharge processes, suggesting the stabilization function of the Mn cations in Ru-based

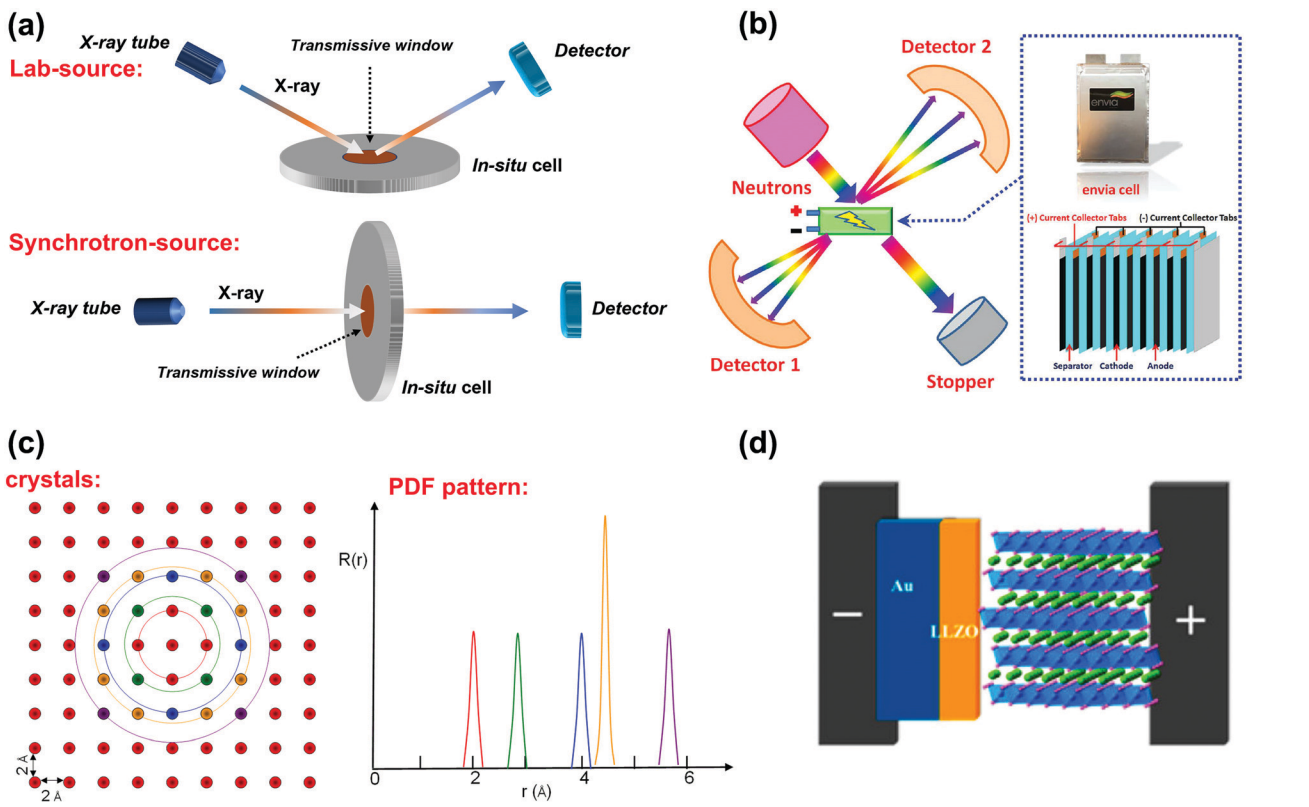

Fig. 18 (a) Schematic illustration of lab-source (top) and synchrotron (bottom) *in situ* XRD set-ups. (b) Schematic of an *operando* ND experimental set-up based on the HLR/Si pouch cell.[166] (c) The illustration of the PDF pattern.[405] (d) *In situ* TEM set-up for studying the $LiCoO_2$/LiPON interface.[406] Reproduced with permission,[166] Copyright 2016, Wiley-VCH. Reproduced with permission from Dr Y. Liao.[405] Reproduced with permission,[406] Copyright 2016, American Chemical Society.

LROs. Recently, Zhao *et al.*[175] have investigated the change in the O–O bond lengths of $Li_{1.2}Ni_{0.13}Mn_{0.54}Co_{0.13}O_2$ during the first cycle by *ex situ* nPDF and found that the local structural changes along with the lattice oxygen redox reaction are reversible. It is highly expected that the *in situ*/*operando* XPDF and nPDF techniques will provide more detailed information about the structural and chemical evolution of both LRO and $Na_xTM_yO_2$ materials, especially in regard to local changes, and thus provide an in-depth understanding of the mechanisms of anionic redox reactions.

5.2 TEM

Among various electrode characterization techniques, TEM, especially the state-of-the-art aberration-corrected TEM, provides most convincible evidence of morphological, structural and chemical informations on the nanometer and even atomic scale of materials and electrodes. In the recent decade, TEM has been widely utilized to understand the pristine structures, structural transitions, and chemical evolution (in combination with EELS) of LROs. For example, it provided direct evidence to settle the argument of solid-solution and two-phase nanodomain hypotheses for the pristine structure (Fig. 4), to identify the formation of spinel-layers and the migration of TM ions (Fig. 10), to visualize the O–O dimers[108] in the oxidized Li_2IrO_3 electrode, *etc.* Furthermore, the *in situ*/*operando* TEM techniques have been designed and widely utilized to study the lithiation/de-lithiation behavior of electrodes materials based on the conversion and alloy mechanisms, such as Si, Ge, Fe_3O_4, *etc.* There are also a few cases that employ them for the investigation of layered cathodes. For example, Wang *et al.*[406] studied the $LiCoO_2$/LiPON (electrode/electrolyte) interface by *in situ* STEM (Fig. 18d) and observed a disordered interfacial layer between $LiCoO_2$ and LiPON even before cycling. They suggested that this layer evolved to form highly oxidized Co ion species along with Li_2O and Li_2O_2 and that the increasing thickness of this layer along cycling leads to rapid capacity decay of the investigated solid-state battery. Gong *et al.*[407] found that single crystal $LiCoO_2$ transformed into nanosized polycrystals at high voltages by *in situ* TEM and proposed the lithium migration pathways before and after this polycrystallization process. Besides, the atomic-scale observation can be made using their chip-based *in situ* TEM holder.[407] With the fast development of the *in situ* TEM technology, the monitoring of the structural and chemical evolution during the lithium intercalation/de-intercalation processes of LROs is realized at the atomic scale.

5.3 ss-NMR

As a non-destructive and quantitative technique, ss-NMR spectroscopy is very sensitive to the local environments and physicochemical states of the target nucleus in both amorphous and well-crystallized substances. In addition to obtaining qualitative and quantitative information on local structures, ss-NMR also gives plenty of kinetic information, such as atom/ion diffusion and migration. Moreover, *in situ*/*operando* ss-NMR can track the intermediate structures and the structural evolution of metastable substances during the electrochemical processes. Therefore, the combination of ss-NMR and other structural probing technologies, such as XRD, XAS, and ND, can provide comprehensive understanding of the mechanisms of structural evolution, electrode degradation, and structure–performance relationships.

The theoretical basis of NMR is as follows (Fig. 19a). In an external magnetic field B_0, an atomic nucleus with non-zero spin-I exhibits a total of $(2I + 1)$ quantized eigenstates (*i.e.*, $-I$, $-I + 1$, ... $+ I$) along B_0. For instance, nuclei with spin-1/2 (such as ^1H) have two eigenstates $m = -1/2$ and $+1/2$, whose eigenvalues or energies can be plotted in the energy level diagram, as shown in the top of Fig. 19a. The energy level splitting of the spin in B_0 is known as the Zeeman splitting, corresponding to the precession of the spin, the so-called Larmor frequency. When a radio frequency (RF) pulse is applied in the direction that is perpendicular to B_0, the spin experiences two external magnetic fields, *i.e.* a static external field B_0 and an oscillating field from the RF pulse. When the oscillating frequency of the RF pulse is resonant with the Larmor frequency, the RF pulse permits the inter-state polarization transition between the lower- and higher-energy states. When the RF pulse is terminated, excessive polarization at a higher energy level excited by the RF pulse will transit back to the lower energy level according to the internal spin interactions such as chemical shifts. In the rotating frame at Larmor frequency, the RF pulse can be simply represented as a vector to rotate the spin magnetization. As demonstrated in the bottom of Fig. 19a, when the RF pulse is applied along the x-axis, it rotates the spin magnetization $+M_z$ from the equilibrium state along the z-axis to $-M_y$ along the y-axis for detection. The receiver coil will pick up the free-induced decay (FID) of $-M_y$, which contains information about the internal spin interactions. Different from solution NMR, wherein samples experience fast and irregular Brownian motion such that only isotropic spin interactions (*i.e.* the chemical shifts and spin–spin J-couplings) are subjected to NMR measurements, ss-NMR deals with relatively rigid samples in which the internal spin interactions are orientation dependent with respect to B_0 such that the observed NMR signals become very broad and even featureless. Magic-angle-spinning (MAS), *i.e.* by rotating the sample along an axis tilted by 54.74° from the external B_0 (Fig. 19b), is a useful technique to remove those orientational dependent spin interactions thus enabling the acquisition of solution-like high-resolution solid-state NMR spectra, as indicated in Fig. 19c.[408]

^6Li, ^7Li, and ^{23}Na ss-NMR have been widely used to investigate the local environment of LIB and NIB electrode materials. At the beginning of the 21st century, based on ^6Li ss-NMR results, Yoon *et al.*[197] confirmed the extraction of Li^+ from TM layers during the first charge process. Yang *et al.*[395] observed the migration of Li^+ from the TM layers to the Na layers in the first cycle of P2-$Na_xLi_yMn_{1-y}O_2$ by ^7Li MAS ss-NMR. Recently, by tracking the local-environment evolution of Li^+ ions *via* ^6Li ss-NMR, House *et al.*[397] have revealed that the local ordering in the TM layers of honeycomb ordered $Na_{0.75}Li_{0.25}Mn_{0.75}O_2$ is partially destroyed, while that of the ribbon ordered $Na_{0.6}Li_{0.2}Mn_{0.8}O_2$ is maintained during the first cycle (Fig. 19d). ss-NMR is also very sensitive to phase transformations. It is well known

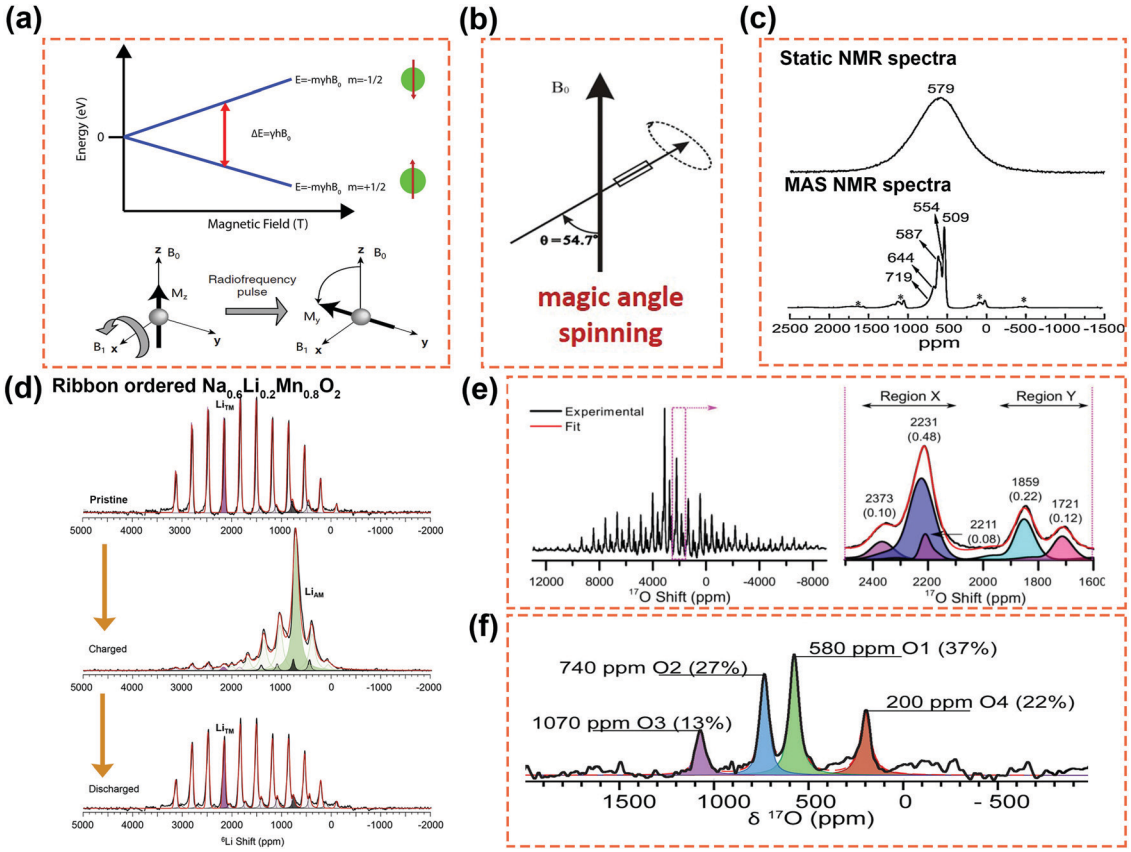

Fig. 19 (a) Schematic illustration of the nucleus spin (i = 1/2) which is related to the Zeeman splitting of the energy levels and the spin system is manipulated by RF pulses. (b) The schematic illustration of magic angle (54.7°) spinning. (c) The ^{7}Li static and MAS NMR spectra of the $Li_{1.08}Mn_{1.92}O_4$ powder sample show that the MAS NMR spectrum provides much more detailed information.[408] (d) The ^{6}Li spectra of ribbon ordered $Na_{0.6}[Li_{0.2}Mn_{0.8}]O_2$ at different charge/discharge states. Lithium ions migrate from TM to AM layers upon charging and diffuse back upon discharge.[397] (e) ^{17}O NMR spectrum of Li_2MnO_3 showing the spinning-sideband manifolds with isotropic resonances highlighted (magenta dashed box) and an expanded view of the isotropic resonances showing the two regions of ^{17}O shifts, X (2100 to 2450 ppm) and Y (1600 to 1950 ppm).[399] (f) ^{17}O MAS NMR spectrum of Li_2RuO_3 at room temperature.[409] Reproduced with permission,[408] Copyright 2013, Elsevier. Reproduced with permission,[397] Copyright 2020, Nature Publishing group. Reproduced with permission,[399] Copyright 2016, American Chemical Society. Reproduced with permission,[409] Copyright 2019, American Chemical Society.

that the Jahn–Teller effect associated with the Mn^{3+}/Mn^{4+} redox couple leads to the notorious P2–P2′ phase transition in the Mn-rich $Na_xTM_yO_2$ material. According to recent results,[365,391] this transformation can be unobservable in the *in situ* XRD patterns when the size of the P2′ phase is out of the detection range of XRD. However, ^{23}Na ss-NMR could provide very reliable information for the identification of new phases. ^{17}O ss-NMR is considered to be a powerful tool to detect the evolution of O ions during the electrochemical process. Grey's groups[399] obtained the ^{17}O NMR spectra of the paramagnetic material Li_2MnO_3 (Fig. 19e). Their hybrid DFT calculations suggested that the most intense isotropic resonances should be assigned to the 4i and 8j sites in the $C2/m$ structure, and the multiple O environments in each region are related to the stacking faults (*ca.* 10%). More recently, the local structures of the pristine Li_2RuO_3 have been investigated by variable temperature ^{7}Li and ^{17}O ss-NMR.[409] In that work, Reeves *et al.* analyzed the ^{17}O NMR spectra based on the simple bond pathway analysis and the effect of metal–metal bonding on the Ru–O overlap. Their results confirmed that Li_2RuO_3 contains four distinct O sites (Fig. 19f). Importantly, they found that the TM–TM interactions should not be ignored in the analysis of ^{17}O NMR spectra of 4d and 5d TM containing compounds, particularly the cathodes with anionic redox reactions.^{17}O ss-NMR is expected to be a promising technique to probe the anionic redox reactions directly. However, because of the strong influence of TM ions, variable bond lengths, low natural abundance of ^{17}O (0.037%), and the large quadrupole moment of the nucleus (I = 5/2), ^{17}O ss-NMR spectra usually exhibit large shifts and broad lines. In conclusion, ss-NMR is a powerful technique for structural characterization and can play a key role in identifying the pristine structure and electrochemically induced local structure transformations of layered lithium/sodium transition metal oxides. It is expected that advanced ss-NMR techniques such as *in situ* ss-NMR and ^{17}O ss-NMR will be developed to further promote the investigation of lattice oxygen redox reactions.

5.4 XPS

The XPS spectrum is obtained by irradiating a material with an X-ray beam, and then measuring the kinetic energy and the

number of electrons that escape from the material. Due to the shallow escape depth of electrons, the probe depth of XPS is limited to 5–10 nm for oxides through in-house laboratory sources of X-ray radiation (such as Al Kα radiation of 1.49 keV). Therefore, as a surface-sensitive quantitative spectroscopic technique, XPS has been widely utilized to investigate the surface composition and the chemical state of specific compounds near the surface of a probe, such as the formation of the SEI and CEI. For LROs, XPS was extended to probe lattice oxygen redox reactions. Tarascon and his co-workers quantified oxygen redox evolution *via* XPS measurement and revealed that the oxidized oxygen content increased during charge and decreased in the following discharge process in Ir-based, Ru-based and Mn-based LROs.[108,126,410] By comparing the XPS spectra of pristine, delithiated, and lithiated $Li_{1.14}Ni_{0.136}Co_{0.136}Mn_{0.544}O_2$, Li_2MnO_3, $LiNi_{0.5}Co_{0.2}Mn_{0.3}O_2$, and $LiCoO_2$ compounds, Han *et al.*[411] also confirmed that the former two species undergo reversible oxygen redox reactions. In recent years, synchrotron-based hard XPS with increased probe depth has also been used to explore lattice oxygen evolution. For example, Ogumi *et al.*[412] observed the formation of O^- ions in the charged $Li[Li_{0.25}Ni_{0.20}Mn_{0.55}]O_{1.93}$ electrode by synchrotron XPS. Assat *et al.* further identified[178] and quantified[413] anionic redox in $Li_{1.2}Ni_{0.13}Mn_{0.54}Co_{0.13}O_2$ based on synchrotron XPS results.

However, it is worth noting that, even with hard X-ray XPS, the probe depth is still limited to about 40 nm at 10.0 keV due to the principle limit of the shallow electron escape depth. This is obviously not the detection scale for the lattice oxygen redox reactions, especially considering that high voltage operations are often required for oxygen redox reactions and trigger parasitic surface reactions with chemical products coating the electrode surface. In addition, assignment of many XPS peaks in the O-K spectra could be easily complicated in a transition-metal system due to the many possible contributions. Indeed, a recent study by Piper *et al.* has directly concluded that the heavily used XPS feature, even with hard X-rays, for discussing oxygen redox reactions is actually from the near surface signals coming from reduced transition-metals and electrolyte decomposition products, showing ''no clear link to oxygen redox''.[414]

5.5 XAS: sXAS and hXAS

XAS is one of the most popular spectroscopic techniques for materials studies in both chemical states and local structural analysis. Naively, XAS could be categorized into three different energy ranges due to the very different instrumentation requirements. Soft XAS (sXAS) and hard XAS (hXAS) typically cover low and high energy ranges of 10–1500 and >3000 eV, respectively. A new domain of 1500–5000 eV has been recently defined as tender XAS (tXAS) with the energy range in the middle of the typical sXAS and hXAS, covering some important technological elements, *e.g.*, S, P, Ru, *etc.* XAS techniques are fundamentally based on electron excitations to unoccupied states by absorbing the incident X-ray photon energy. Therefore, the characteristic energy levels of the electron states of individual elements could be easily distinguished by the characteristic energy called an ''absorption edge''.[415] Most XAS experiments require synchrotron facilities with continuously tunable incident X-ray sources; however, recent developments in desktop X-ray sources have started to enable some of the hXAS experiments using a lab-based system. But in general, synchrotron-based experiments provided far better statistics and resolution by this time. Particularly, new developments in diffraction limited light sources, microscopic, and 3d tomography have greatly improved the spatial, temporal, and energy resolutions of XAS techniques.[415]

Relatively, hXAS is more popular in battery material studies, mainly due to the deep penetration depth of hard X-rays, leading to convenience in both sample handling and *in situ*/*operando* experiments. Almost all hXAS endstations at synchrotron facilities are equipped with *in situ*/*operando* electrochemical cell systems, and *in situ*/*operando* hXAS has become almost standard in today's battery research.[403,415] Information from hXAS could be obtained from different aspects based on X-ray absorption near-edge structure (XANES) and extended X-ray absorption fine structure (EXAFS) analysis. XANES is often used for measuring the TM valence states, and EXAFS is powerful for detecting the local chemical bond changes and coordination numbers.[118] For example, a recent study on the voltage fade and its association with oxygen activities in LRO electrodes was mostly based on the hXAS results.[187] Although hXAS cannot access the O-K edge around 525–550 eV, due to the technical advantages and convenience of hXAS, evaluation of the cationic redox reactions is often used as indirect evidence of oxygen redox reactions if they cannot compensate all charge transfer numbers observed in electrochemistry.[187]

Although hXAS has been a popular and powerful tool for various studies of LRO materials, the main edge feature of hXAS corresponds to the excitation to 4p states, not the 3d valence states for 3d TMs. This could lead to complications in measuring some important elements, *e.g.*, Mn. In addition, the direct probe for low-*Z* elements requires low energy range sXAS, *e.g.*, C, N, O, *etc.* Indeed, Mn–K has been found to display very different edge positions and lineshapes in K-edge hXAS XANEX spectra even with the same Mn valence value due to the effect of the environmental ligand changes.[416] In contrast, sXAS L-edges correspond to the direct excitation to the 3d valence states for 3d TMs. Such a direct correspondence leads to a high sensitivity of the spectral lineshape to the TM valence states, which could be quantified to obtain the oxidation state distributions in battery electrodes.[417] Further analysis of the TM-L of electrodes, often coupled with theoretical calculations, could also reveal the spin states that are directly associated with the electrochemical profile.[418,419]

As shown in Fig. 20a, sXAS covers the K-edge for low-*Z* elements and L-edge for 3d TMs, both of which are important for battery cathode materials.[417] Modern sXAS systems are always equipped with different detection channels to collect sXAS signals simultaneously by counting the number of both the electrons, *i.e.*, total electron yield (TEY), and photons, *i.e.*, total fluorescence yield (TFY), emitted from the samples after soft X-ray photon absorption. TEY and TFY offer two different probe depths of about 10 nm and 100–300 nm depending on the photon energies, respectively.[420] The combined TEY and

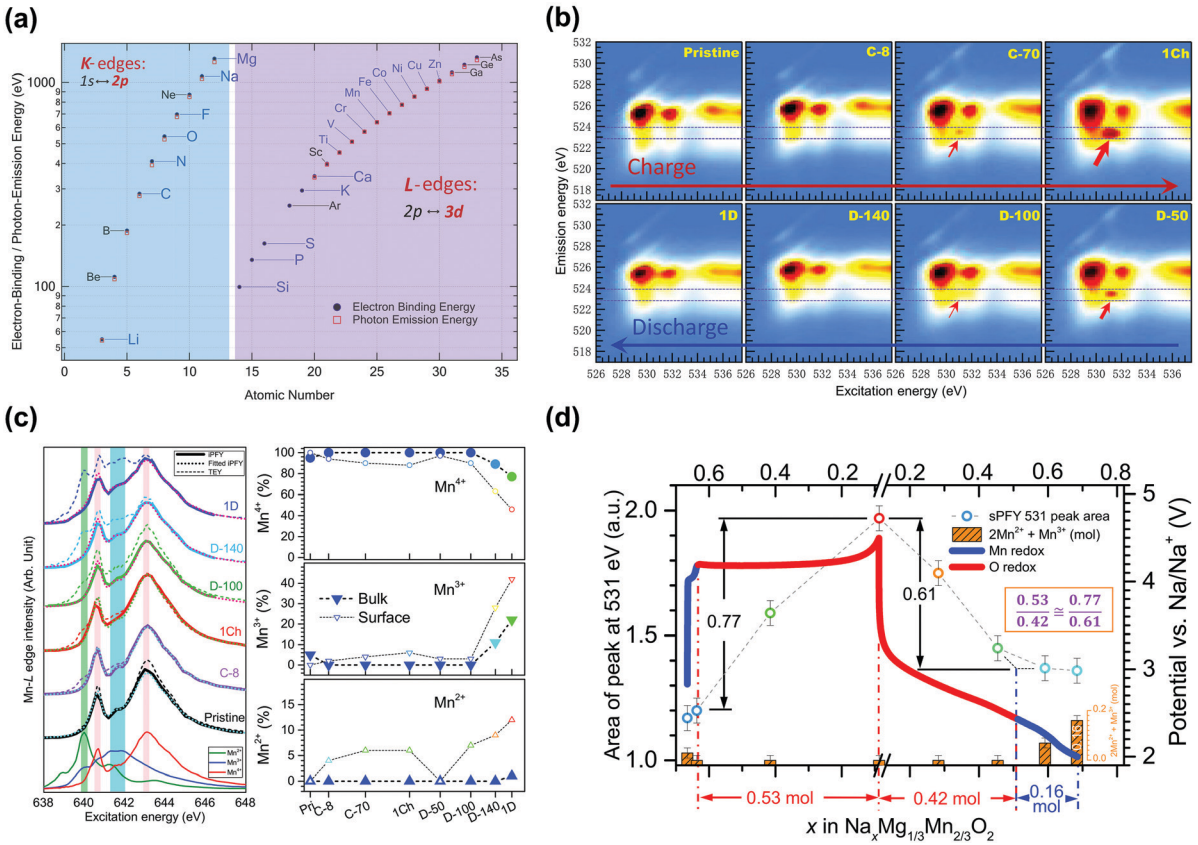

Fig. 20 (a) Coverage of elements and the corresponding excitations that are accessible by soft XAS and RIXS spectroscopy.[417] (b) O K-edge mRIXS of $Na_{2/3}Mg_{1/3}Mn_{2/3}O_2$ electrodes at different states of charge or discharge during the initial cycle.[77] (c) Mn L-edge iPFY extracted from mRIXS results (solid lines), a relatively bulk sensitive probe, contrasting the surface signals from TEY spectra (dashed lines). Both the bulk and surface Mn states could be quantified at different electrochemical states.[77] (d) The combination of independently evaluated Mn and O redox reactions through Mn-L mRIXS-iPFY and O-K mRIXS-sPFY interprets the total electrochemical capacity with well-defined Mn-redox and O-redox reactions in $Na_{2/3}Mg_{1/3}Mn_{2/3}O_2$.[77] Reproduced with permission,[417] Copyright 2016, IOP Publishing. Reproduced with permission,[77] Copyright 2019, Elsevier.

TFY modes thus provide information on both the surface and relatively bulk chemistry of both the TM and oxygen states of electrodes and SEI.[417,421,422]

5.6 Soft X-ray RIXS and mRIXS

The depth of today's battery research has gone beyond what conventional sXAS could offer in many aspects. Particularly for LRO studies, bulk TM and O states need to be reliably characterized to understand the important cationic and anionic reactions involved in this high capacity material. Unfortunately, many TM-L sXAS spectra in its bulk-sensitive TFY mode are heavily distorted, making it impossible to be evaluated.[423] Although O-K sXAS could be easily obtained, the features are dominated by TM characters through the strong hybridization effect. Both the intensity and the lineshape of the O-K sXAS pre-edge features vary significantly with the changing TM states,[111,424] leading to many confusing discussions on oxygen redox states in battery electrodes. For example, $LiFePO_4$ displays probably the strongest contrast in O-K sXAS pre-edge features with a clear pre-edge intensity enhancement in the charged state;[425] however, $LiFePO_4$ is known and has been verified to be a pure Fe-redox system without any oxygen redox reactions.

The challenges in probing the bulk anionic and cationic redox reactions were tackled directly by the spectroscopic community, and the high-efficiency mapping of RIXS (mRIXS) over a wide range of absorption edge energies naturally came to the horizon because it could further resolve the emission energy of the emitted photons,[426] rather than only counting the total number as in sXAS TFY signals. This has greatly improved the chemical sensitivity of the TM and O state detection.

For TMs, the inverse partial fluorescence yield (iPFY) signals from mRIXS could be used to extract undistorted bulk signals of TM-L spectra,[111] which could be quantified directly to get the precise charge transfer numbers from cationic redox reactions (Fig. 20c).[77,218] In addition, the unusual states of TMs could be revealed even if conventional sXAS cannot sense their chemical differences,[427] again due to the much improved chemical sensitivity of mRIXS.

For oxygen redox states, because mRIXS offers a new dimension of information along the emission energy, it could distinguish the oxidized oxygen species, typically at around 523.7 eV emission energy,[428,429] from the strong TM contribution at around 525 eV emission energy.[111] As a matter of fact, RIXS

cuts at several individual energies have been found earlier in LRO electrodes before mRIXS reports, however, without meaningful interpretations.[70] The extensive application of mRIXS started to emerge when the technique was established as a reliable probe for the lattice oxygen redox in LRO compounds,[73,430] with the fingerprinting feature intensity varying with the electrochemical profile and being quantifiable to obtain the reversibility of oxygen redox reactions. Fig. 20b displays how the oxidized oxygen feature (indicated by red arrows) starts to emerge during charging, and disappears during discharging.[77] Following the intensity variation of the Mn L-edge (Fig. 20c) and oxidized oxygen feature in mRIXS, reversibility and cyclability could be quantified for oxygen redox reactions (Fig. 20d). For example, the oxygen redox reaction of $Li_{1.17}Ni_{0.21}Co_{0.08}Mn_{0.54}O_2$ is found to be 76% reversible during the initial cycle with 44% being retained after 500 cycles, much higher than expected.[77]

At present, mRIXS has been recognized as a reliable tool for detecting the oxygen redox states in LRO materials with both layered and disordered rocksalt structures,[122,354,431] conventional electrodes,[432–434] and Na-ion battery electrodes.[77,218,378] The full potential of the mRIXS technique for uncovering the unconventional chemical states of both TM and O in batteries is yet to be explored. A recent mRIXS study has shown that mRIXS is sensitive enough to find the subtle effect of the oxidized oxygen states with an inductive effect from a proton in the vicinity.[86] Such a high sensitivity also makes mRIXS an ideal probe for other hard-to-detect systems, such as electrolyte solvation shells.[435]

It is important to note that, although mRIXS has now been widely used for characterizing battery electrodes, especially the oxygen redox reactions, the theoretical interpretation of this specific feature in LRO materials remains elusive. Calculations could reproduce the oxidized oxygen feature in model systems with oxidized oxygen,[428] however, they have failed to generate the feature similar to that in TM oxide electrodes, indicating the different fundamental nature of the oxidized oxygen in LRO electrodes. Indeed, a recent mRIXS comparison directly between Li_2O_2, O_2, Na-ion batteries and LRO electrodes has indicated that the oxidized oxygen states in these systems are different.[429] Nonetheless, the fundamental nature of the oxygen redox mechanism would be clarified if the mRIXS feature could be theoretically resolved in TM oxide systems, which remains a challenge for fundamental physicists, chemists, and materials scientists.

5.7 EPR

EPR can be utilized to study materials with unpaired electrons or radicals. In the journey of LRO research, the potential of EPR characterization to probe the oxidized oxygen species has been fully demonstrated.[68,128] Moreover, the development of the *in situ* EPR technique enables the visualization of reversible oxygen redox reactions in $Li_2Ru_{0.75}Sn_{0.25}O_3$,[110] as well as the O and Mn redox in Mn-based Li-rich Li_2MnO_3, $Li_{1.2}Ni_{0.2}Mn_{0.6}O_2$, and $Li_{1.2}Ni_{0.13}Mn_{0.54}Co_{0.13}O_2$ cathodes.[436] In summary, the corresponding *in situ*/*operando* EPR technique is very helpful to establish the fundamental understanding of reversible anionic redox chemistry.

6. Conclusions and outlook

To fulfill the requirements for the next-generation energy storage systems applied in electric vehicles and grid storage, it is critical to develop advanced batteries with high energy density, low cost, long service life, environmental benignity, and high safety standard. Due to the combination of both cationic and anionic redox, LRO compounds have become promising candidates for achieving energy densities beyond those of the current state-of-the-art LIB cathodes, which is the bottleneck of today's battery capacity and energy density. With over thirty years of development, continuous improvements in electrochemical performance and advances in understanding the structure and charge-compensation mechanisms of LROs have been made. Nevertheless, various performance parameters of LROs, especially the retention of energy density, cycling stability, and rate performance, are still not comparable to commercialized NCA and NCM electrodes, which hinders the application of LRO electrodes.

Fig. 21 summarizes the reaction mechanisms, electrochemical performances, and challenges of LLRO systems at both material and cell levels (involving the influence of the electrolyte). The high capacity and high energy density of LROs originate from oxygen redox reactions, which cause undesirable oxygen gas release, surface reactions, and residues of Li^+ vacancies in the TM layers. These activities can arouse and/or accelerate the following issues: (i) the formation of structural defects and even voids in the bulk, (ii) TM migration within the TM layers and/or from the TM layers to Li layers, (iii) LS transition near the surface and bulk holes, which not only do lead to electrochemical challenges, including insufficient service life, poor rate capability and low ICE, but also do activate the low-voltage redox couples and result in voltage fade, (iv) the released O_2 or radical oxygen could accelerate the oxidation of carbonate electrolytes and surface reactions, further deteriorating their electrochemical performances. Similar problems are also faced by oxygen redox active DLROs and $Na_xTM_yO_2$. Based on these facts and concerns, several future challenges and directions are highlighted in the following discussion.

6.1 Standardizing the LRO test protocol

Searching for new types of materials with appropriate stoichiometry is still highly essential to develop advanced LROs, especially promising DLROs. However, for many reported LROs, the comprehensive electrochemical performance, especially cycling stability, remains a mystery, let alone the detailed comparison between different LROs. This might mislead the readers and researchers. It is therefore highly desirable for researchers to offer a common set of electrochemical performance tests when reporting a new material, including the rate capability and cycling stability at both low and high current densities, even if the electrochemical performances are not the research focus. Besides electrochemistry, the air-stability of LROs should be investigated and included in the database, because preparation and storage conditions of materials/electrodes influence the costs and determine whether the LROs are truly commercially viable.

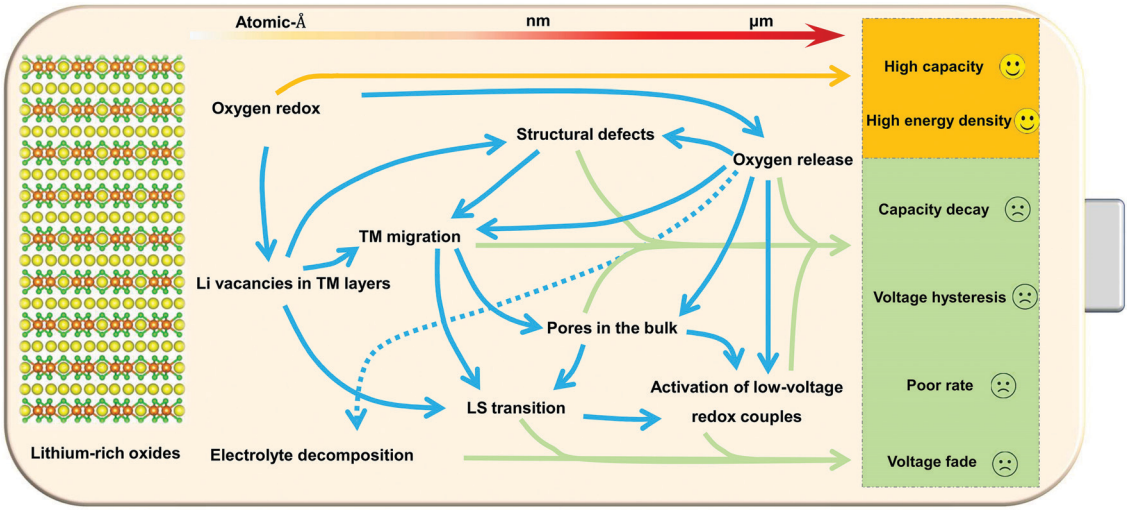

Fig. 21 Illustration of the underlying reaction mechanisms and electrochemical performances of LROs.

6.2 Eliminating the voltage fade

To resolve voltage fade and voltage hysteresis in LROs, an in-depth understanding of the redox reaction and structural evolution mechanisms of oxygen redox active materials with low voltage hysteresis and voltage fade, such as Li_2IrO_3 and Li_2RuO_3, is definitely required. In addition, as discussed above, certain Na-poor compounds, *e.g.* $Na_{2/3}Ni_{1/3}Mn_{2/3}O_2$, with strong oxygen redox reactions display a highly reversible reaction profile with negligible voltage hysteresis. In general, regulating the electronic structures and redox behaviors of LROs should be taken into consideration to stabilize oxygen radicals and reduce irreversible oxygen reactions. In addition, to better understand voltage hysteresis and voltage fade, advanced characterization tools, especially *in situ*/*operando* techniques. are highly needed to clarify the region (bulk or surface, spatial resolution), the time (temporal resolution), and the products of the oxygen redox reactions. Besides, to further understand the nature of redox reactions, direct theoretical calculations for spectroscopic analysis need to be developed and established.

6.3 Strategies accelerating the path to practical applications

LROs hold great advantages of high capacity, low cost and relatively high working potentials. However, their application prospects are still in their trial stage. Strategic plans are necessary to explore the applications of LROs: (i) balancing cationic and anionic redox in LROs to achieve both high capacity and structural stability. At the early stage of commercialization, LRO compounds with relatively low excess Li^+ contents are recommended. (ii) Computational studies, especially high throughput computing, can provide targeted guidance for the selection, synthesis, and modification of new LRO electrodes with compatible electrolytes. Calculations could be valuable also for designing ideal electrode–electrolyte interfaces and new structures of active materials. (iii) Employment of solid-state electrolytes provides another opportunity for LROs. Since solid-state electrolytes address the safety concerns of metallic Li and allow the application of high upper cut-off voltage of cathodes, it can be expected that the solid-state batteries based on LROs would offer improved safety and high energy density. (iv) Designing economic, green and facile industrial processes and optimizing the synthesis procedure to obtain LROs with high tap densities for achieving high volumetric energy density in a practical cell.

6.4 Full-cell design

Up to now, most of the scientific studies of LROs are based on half-cells with metallic Li as the counter/reference electrode. However, it is well recognized that the electrochemical behaviors of a specific electrode material in full-cells are very different to those in half-cells. First of all, the initial coulombic efficiency (ICE) is more important in full-cells than in half-cells, because the low ICE of cathodes will lead to the underutilization of anodes and trigger detrimental issues on the electrode balance. Second, the release of O_2 into organic electrolytes is a severe problem in full cells, because O_2 consumes the electrolyte, leading to cell flatulence and thus compromising the safety. Therefore, effective strategies for both electrolytes and electrode materials should be adopted to alleviate or eliminate oxygen release. Thirdly, electrode processing should be optimized for achieving high mass loading of electrodes. Such an engineering improvement is a direct and efficient way for enhancing the energy density of full-cells.

6.5 Oxygen redox in Na-based systems

It is generally accepted that little oxygen gas is released during oxygen redox in Na-based systems. In addition, for most of the layered Na-poor oxides with oxygen redox, there are no Na vacancies generated in the TM layers except for Li-substituted/doped Na_xTMO_2 compounds. Therefore, on the one hand, Na-based oxides can be used as models to grasp the intrinsic characteristics of lattice oxygen redox, reveal the relationship between lattice oxygen redox and oxygen release, and thus provide new information for the research and design of advanced LROs. On the other hand, the high reversibility of the lattice oxygen redox in Na_xTMO_2

positively supports their potential application as cathode materials for NIBs. The oxygen redox reactions are often accompanied by large voltage hysteresis and phase transformations. However, the finding that some Na-poor layered compounds could maintain extremely low voltage hysteresis with strong oxygen redox reactions indicates that there is much to learn from the Na-based systems to shed light on our understanding of LROs. Therefore, the roles of oxygen redox in the Na_xTMO_2 system need to be further clarified.

In summary, LROs have attracted enormous attention in the field of energy storage materials due to their higher specific capacity and lower cost compared with commercially available LIB cathodes. Herein, we reviewed the history, pristine structures, nature of anionic redox, structural evolution mechanisms, electrochemical challenges and corresponding materials modification, and characterization of LROs. The continuous development of characterization techniques and synthesis methods will expand the research efforts to both reaction mechanisms and electrochemical performance further. We note that formidable challenges remain for the employment of LROs in practical devices, *e.g.* O_2 release, TM migration, voltage fade, and low ICE. However, similar to the significant achievements made in the broad field of highly correlated physics through studies of high temperature superconductors that are still yet to reach practicability at room temperature, the optimism embedded in every study of LROs not only relies on the practical potential of the materials, but also research on such complex systems has inspired the bloom of a number of advanced experimental techniques and theoretical calculations for gaining unprecedented depth of information on batteries. It is our belief that such a benefit from LRO studies for the whole energy science field will surely continue and prevail even after the commercialization of the materials.

List of abbreviations

ABF-STEM	Annular bright field scanning transmission electron microscopy
CEI	Cathode electrolyte interphase
DEMS	Differential electrochemical mass spectroscopy
DFT	Density functional theory
DLROs	Cation disordered lithium-rich oxides
ED	Electron diffraction
EELS	Electron energy loss spectroscopy
EPR	Electron paramagnetic resonance
EVs	Electric vehicles
EXAFS	Extended X-ray absorption fine structure
HAADF-STEM	High-angle annular dark-field scanning transmission electron microscopy
HLR	LMROs with high-lithium content
ICE	Initial coulombic efficiency
iPFY	Inverse partial fluorescence yield
LCO	$LiCoO_2$
LMO	$LiMn_2O_4$
LFP	$LiFePO_4$
LIBs	Lithium-ion batteries
LLROs	Layered lithium-rich oxides
LLR	LMROs with low-lithium content
LMROs	Li-rich Mn-rich oxides ($Li[Li_xNi_yCo_zMn_{1-x-y-z}]O_2$)
LROs	Lithium-rich oxides
LS transition	Layer to spinel-like phase transition
MAS	Magic angle spinning
mRIXS	Mapping of resonant inelastic X-ray scattering
$Na_xTM_yO_2$	Layered sodium transition metal oxides
NCA	$LiNi_xCo_yAl_{1-x-y}O_2$
NCM	$LiNi_xCo_yMn_{1-x-y}O_2$
ND	Neutron diffraction
NIBs	Sodium ion batteries
nPDF	Neutron pair distribution function
PDF	Pair distribution function
RIXS	Resonant inelastic X-ray scattering spectroscopy
SAED	Selected area electron diffraction
SEI	Solid electrolyte interphase
ss-NMR	Solid-state nuclear magnetic resonance
STEM	Scanning transmission electron microscopy
STXM	Scanning transmission X-ray microscopy
sXAS	Soft X-ray absorption spectroscopy
TEM	Transmission electron microscopy
TEY	Total electron yield
TFY	Total fluorescence yield
TGA-MS	Thermogravimetric analysis/mass spectrometry
TM	Transition metal
XANES	X-ray adsorption near-edge structure
XAS	X-ray absorption spectroscopy
XPDF	X-ray pair distribution function
XPS	X-ray photoelectron spectroscopy
XRD	X-ray diffraction

Conflicts of interest

There are no conflicts to declare.

Acknowledgements

This work is financially supported by the National Key Research and Development Program of China (grant no. 2018YFB0905400, 2016YFB0901502) and the National Natural Science Foundation of China (grant no. 21761132030, 21935009). R. Fu acknowledges the support from the National High Magnetic Field Laboratory which is supported by NSF Cooperative Agreement DMR-1644779 and the State of Florida. M. Winter and J. Li acknowledge German Research Foundation (DFG, project Li 2916/2-1) for funding support. W. Y. is supported by the Advanced Light Source, a U.S. DOE Office of Science User Facility under contract no. DE-AC02-05CH11231. W. Zuo acknowledges the scholarship from Huawei Technologies Co., Ltd.

References

1 M. S. Whittingham, *Chem. Rev.*, 2014, **114**, 11414–11443.
2 M. Winter and R. J. Brodd, *Chem. Rev.*, 2004, **104**, 4245–4270.

3 M. A. Hannan, M. M. Hoque, A. Mohamed and A. Ayob, *Renewable Sustainable Energy Rev.*, 2017, **69**, 771–789.
4 M. Armand and J.-M. Tarascon, *Nature*, 2008, **451**, 652–657.
5 M. M. Thackeray, C. Wolverton and E. D. Isaacs, *Energy Environ. Sci.*, 2012, **5**, 7854.
6 R. Schmuch, R. Wagner, G. Hörpel, T. Placke and M. Winter, *Nat. Energy*, 2018, **3**, 267–278.
7 G. E. Blomgren, *J. Electrochem. Soc.*, 2017, **164**, A5019–A5025.
8 M. Winter, B. Barnett and K. Xu, *Chem. Rev.*, 2018, **118**, 11433–11456.
9 EUCAR, Battery requirements for future automotive applications https://eucar.be/wp-content/uploads/2019/08/20190710-EG-BEV-FCEV-Battery-requirements-FINAL.pdf.
10 A. Kurosawa, Energy Storage Roadmap Technology and Institution, https://www.icef-forum.org/platform/upload/2017cop/Roadmap_Launch_Event_at_COP23-4Atsushi_Kurosawa.pdf.
11 K. Edström, Battery 2030+ roadmap, https://battery2030.eu/research/roadmap/.
12 R. Wagner, N. Preschitschek, S. Passerini, J. Leker and M. Winter, *J. Appl. Electrochem.*, 2013, **43**, 481–496.
13 W. Dong, J. Xu, C. Wang, Y. Lu, X. Liu, X. Wang, X. Yuan, Z. Wang, T. Lin, M. Sui, I. W. Chen and F. Huang, *Adv. Mater.*, 2017, **29**, 1700136.
14 D. Li, D. Danilov, Z. Zhang, H. Chen, Y. Yang and P. H. L. Notten, *J. Electrochem. Soc.*, 2015, **162**, A858–A869.
15 K. Xu, *Chem. Rev.*, 2014, **114**, 11503–11618.
16 W. Zuo, R. Li, C. Zhou, Y. Li, J. Xia and J. Liu, *Adv. Sci.*, 2017, **4**, 1600539.
17 T. Placke, R. Kloepsch, S. Dühnen and M. Winter, *J. Solid State Electrochem.*, 2017, **21**, 1939–1964.
18 J. W. Fergus, *J. Power Sources*, 2010, **195**, 939–954.
19 M. Wolff, Y. Arinicheva, S. Lobe, C. Dellen, D. Fattakhova-Rohlfing, O. Guillon, D. Boehm, F. Zoller, R. Schmuch, J. Li, M. Winter, E. Adamczyk and V. Pralong, *Advanced ceramics for energy conversion and storage*, Elsevier, 2020.
20 X. Su, Q. Wu, J. Li, X. Xiao, A. Lott, W. Lu, B. W. Sheldon and J. Wu, *Adv. Energy Mater.*, 2014, **4**, 1300882.
21 Z. L. Zhang, Y. H. Wang, W. F. Ren, Q. Q. Tan, Y. F. Chen, H. Li, Z. Y. Zhong and F. B. Su, *Angew. Chem., Int. Ed.*, 2014, **53**, 5165–5169.
22 C. S. Wang, G. T. Wu, X. B. Zhang, Z. F. Qi and W. Z. Li, *J. Electrochem. Soc.*, 1998, **145**, 2751–2758.
23 M. Winter, J. O. Besenhard, J. H. Albering, J. Yang and M. Wachtler, *Prog. Batteries Battery Mater.*, 1998, **17**, 208–213.
24 P. Meister, H. Jia, J. Li, R. Kloepsch, M. Winter and T. Placke, *Chem. Mater.*, 2016, **28**, 7203–7217.
25 M. Winter, J. O. Besenhard, M. E. Spahr and P. Novák, *Adv. Mater.*, 1998, **10**, 725–763.
26 W. Li, B. Song and A. Manthiram, *Chem. Soc. Rev.*, 2017, **46**, 3006–3059.
27 J. Betz, G. Bieker, P. Meister, T. Placke, M. Winter and R. Schmuch, *Adv. Energy Mater.*, 2018, **9**, 1803170.
28 K. Mizushima, P. C. Jones, P. J. Wiseman and J. B. Goodenough, *Mater. Res. Bull.*, 1980, **15**, 783–789.
29 J. Cao, G. Hu, Z. Peng, K. Du and Y. Cao, *J. Power Sources*, 2015, **281**, 49–55.
30 L. Wang, B. Chen, J. Ma, G. Cui and L. Chen, *Chem. Soc. Rev.*, 2018, **47**, 6505–6602.
31 A. Fotouhi, D. J. Auger, K. Propp, S. Longo and M. Wild, *Renewable Sustainable Energy Rev.*, 2016, **56**, 1008–1021.
32 M. M. Thackeray, W. I. F. David, P. G. Bruce and J. B. Goodenough, *Mater. Res. Bull.*, 1983, **18**, 461–472.
33 A. K. Padhi, K. S. Nanjundaswamy and J. B. Goodenough, *J. Electrochem. Soc.*, 1997, **144**, 1188–1194.
34 A. Mauger and C. Julien, *Batteries*, 2018, **4**, 39.
35 N. S. Choi, Z. Chen, S. A. Freunberger, X. Ji, Y. K. Sun, K. Amine, G. Yushin, L. F. Nazar, J. Cho and P. G. Bruce, *Angew. Chem., Int. Ed.*, 2012, **51**, 9994–10024.
36 A. Manthiram, *J. Phys. Chem. Lett.*, 2011, **2**, 176–184.
37 B. Ammundsen and J. Paulsen, *Adv. Mater.*, 2001, **13**, 943–956.
38 H.-J. Noh, S. Youn, C. S. Yoon and Y.-K. Sun, *J. Power Sources*, 2013, **233**, 121–130.
39 W. D. Li, X. M. Liu, H. Celio, P. Smith, A. Dolocan, M. F. Chi and A. Manthiram, *Adv. Energy Mater.*, 2018, **8**, 1703154.
40 S.-T. Myung, F. Maglia, K.-J. Park, C. S. Yoon, P. Lamp, S.-J. Kim and Y.-K. Sun, *ACS Energy Lett.*, 2016, **2**, 196–223.
41 A. Manthiram, J. C. Knight, S.-T. Myung, S.-M. Oh and Y.-K. Sun, *Adv. Energy Mater.*, 2016, **6**, 1501010.
42 Z. Lu, D. D. MacNeil and J. R. Dahn, *Electrochem. Solid-State Lett.*, 2001, **4**, A191.
43 M. M. Thackeray, S.-H. Kang, C. S. Johnson, J. T. Vaughey, R. Benedek and S. A. Hackney, *J. Mater. Chem.*, 2007, **17**, 3112.
44 W. Wei, L. Chen, A. Pan and D. G. Ivey, *Nano Energy*, 2016, **30**, 580–602.
45 H. Zhao, B. Qiu, H. Guo, K. Jia, Z. Liu and Y. Xia, *Green Energy Environ.*, 2017, **2**, 174–185.
46 J. Wang, X. He, E. Paillard, N. Laszczynski, J. Li and S. Passerini, *Adv. Energy Mater.*, 2016, **6**, 1600906.
47 B. Li and D. Xia, *Adv. Mater.*, 2017, **29**, 1701054.
48 N. Yabuuchi, *Chem. Lett.*, 2017, **46**, 412–422.
49 C. Zhao, Q. Wang, Y. Lu, Y.-S. Hu, B. Li and L. Chen, *J. Phys. D: Appl. Phys.*, 2017, **50**, 183001.
50 G. Assat and J.-M. Tarascon, *Nat. Energy*, 2018, **3**, 373–386.
51 R. J. Clément, Z. Lun and G. Ceder, *Energy Environ. Sci.*, 2020, **13**, 345–373.
52 S. Hy, H. Liu, M. Zhang, D. Qian, B.-J. Hwang and Y. S. Meng, *Energy Environ. Sci.*, 2016, **9**, 1931–1954.
53 P. Rozier and J. M. Tarascon, *J. Electrochem. Soc.*, 2015, **162**, A2490–A2499.
54 J. Zheng, S. Myeong, W. Cho, P. Yan, J. Xiao, C. Wang, J. Cho and J.-G. Zhang, *Adv. Energy Mater.*, 2017, **7**, 1601284.
55 J. R. Croy, M. Balasubramanian, K. G. Gallagher and A. K. Burrell, *Acc. Chem. Res.*, 2015, **48**, 2813–2821.
56 H. Yu and H. Zhou, *J. Phys. Chem. Lett.*, 2013, **4**, 1268–1280.
57 G. Lang, *Z. Anorg. Allg. Chem.*, 1966, **348**, 246–256.
58 M. Jansen and R. Hoppe, *Z. Anorg. Allg. Chem.*, 1973, **397**, 279–289.
59 M. S. Whittingham, *Science*, 1976, **192**, 1126–1127.

60 P. G. Bruce, A. R. Armstrong and R. L. Gitzendanner, *J. Mater. Chem.*, 1999, **9**, 193–198.
61 M. H. Rossouw and M. M. Thackeray, *Mater. Res. Bull.*, 1991, **26**, 463–473.
62 M. H. Rossouw, D. C. Liles and M. M. Thackeray, *J. Solid State Chem.*, 1993, **104**, 464–466.
63 C. S. Johnson, S. D. Korte, J. T. Vaughey, M. M. Thackeray, T. E. Bofinger, Y. Shao-Horn and S. A. Hackney, *J. Power Sources*, 1999, **81-82**, 491–495.
64 P. Kalyani, S. Chitra, T. Mohan and S. Gopukumar, *J. Power Sources*, 1999, **80**, 103–106.
65 W. Tang, H. Kanoh, X. Yang and K. Ooi, *Chem. Mater.*, 2000, **12**, 3271–3279.
66 A. R. Armstrong, M. Holzapfel, P. Novak, C. S. Johnson, S. H. Kang, M. M. Thackeray and P. G. Bruce, *J. Am. Chem. Soc.*, 2006, **128**, 8694–8698.
67 E. McCalla, A. W. Rowe, R. Shunmugasundaram and J. R. Dahn, *Chem. Mater.*, 2013, **25**, 989–999.
68 M. Sathiya, G. Rousse, K. Ramesha, C. P. Laisa, H. Vezin, M. T. Sougrati, M. L. Doublet, D. Foix, D. Gonbeau, W. Walker, A. S. Prakash, M. Ben Hassine, L. Dupont and J. M. Tarascon, *Nat. Mater.*, 2013, **12**, 827–835.
69 J. Lee, A. Urban, X. Li, D. Su, G. Hautier and G. Ceder, *Science*, 2014, **343**, 519–522.
70 K. Luo, M. R. Roberts, R. Hao, N. Guerrini, D. M. Pickup, Y. S. Liu, K. Edstrom, J. Guo, A. V. Chadwick, L. C. Duda and P. G. Bruce, *Nat. Chem.*, 2016, **8**, 684–691.
71 D. H. Seo, J. Lee, A. Urban, R. Malik, S. Kang and G. Ceder, *Nat. Chem.*, 2016, **8**, 692–697.
72 B. Mortemard de Boisse, G. Liu, J. Ma, S. Nishimura, S. C. Chung, H. Kiuchi, Y. Harada, J. Kikkawa, Y. Kobayashi, M. Okubo and A. Yamada, *Nat. Commun.*, 2016, **7**, 11397.
73 W. E. Gent, K. Lim, Y. Liang, Q. Li, T. Barnes, S. J. Ahn, K. H. Stone, M. McIntire, J. Hong, J. H. Song, Y. Li, A. Mehta, S. Ermon, T. Tyliszczak, D. Kilcoyne, D. Vine, J. H. Park, S. K. Doo, M. F. Toney, W. Yang, D. Prendergast and W. C. Chueh, *Nat. Commun.*, 2017, **8**, 2091.
74 U. Maitra, R. A. House, J. W. Somerville, N. Tapia-Ruiz, J. G. Lozano, N. Guerrini, R. Hao, K. Luo, L. Jin, M. A. Perez-Osorio, F. Massel, D. M. Pickup, S. Ramos, X. Lu, D. E. McNally, A. V. Chadwick, F. Giustino, T. Schmitt, L. C. Duda, M. R. Roberts and P. G. Bruce, *Nat. Chem.*, 2018, **10**, 288–295.
75 G. Assat, S. L. Glazier, C. Delacourt and J.-M. Tarascon, *Nat. Energy*, 2019, **4**, 647–656.
76 M. D. Radin, J. Vinckeviciute, R. Seshadri and A. Van der Ven, *Nat. Energy*, 2019, **4**, 639–646.
77 K. Dai, J. Wu, Z. Zhuo, Q. Li, S. Sallis, J. Mao, G. Ai, C. Sun, Z. Li, W. E. Gent, W. C. Chueh, Y.-d. Chuang, R. Zeng, Z.-x. Shen, F. Pan, S. Yan, L. F. J. Piper, Z. Hussain, G. Liu and W. Yang, *Joule*, 2019, **3**, 518–541.
78 Z. Lu, L. Y. Beaulieu, R. A. Donaberger, C. L. Thomas and J. R. Dahn, *J. Electrochem. Soc.*, 2002, **149**, A778.
79 Z. Lu and J. R. Dahn, *J. Electrochem. Soc.*, 2002, **149**, A815.
80 Z. Lu and J. R. Dahn, *J. Electrochem. Soc.*, 2002, **149**, A1454.
81 A. D. Robertson and P. G. Bruce, *Chem. Commun.*, 2002, 2790–2791.
82 A. D. Robertson and P. G. Bruce, *Chem. Mater.*, 2003, **15**, 1984–1992.
83 A. R. Armstrong and P. G. Bruce, *Electrochem. Solid-State Lett.*, 2004, **7**, A1.
84 N. Tran, L. Croguennec, M. Ménétrier, F. Weill, P. Biensan, C. Jordy and C. Delmas, *Chem. Mater.*, 2008, **20**, 4815–4825.
85 A. J. Perez, R. Beer, Z. Lin, E. Salager, P.-L. Taberna, A. M. Abakumov, P. Simon and J.-M. Tarascon, *Adv. Energy Mater.*, 2018, **8**, 1702855.
86 J. Wu, X. Zhang, S. Zheng, H. Liu, J. Wu, R. Fu, Y. Li, Y. Xiang, R. Liu, W. Zuo, Z. Cui, Q. Wu, S. Wu, Z. Chen, P. Liu, W. Yang and Y. Yang, *ACS Appl. Mater. Interfaces*, 2020, **12**, 7277–7284.
87 Y. Shin and A. Manthiram, *Electrochim. Acta*, 2003, **48**, 3583–3592.
88 Y.-S. Hong, Y. J. Park, X. Wu, K. S. Ryu and S. H. Chang, *Electrochem. Solid-State Lett.*, 2003, **6**, A166.
89 H. Koga, L. Croguennec, M. Menetrier, K. Douhil, S. Belin, L. Bourgeois, E. Suard, F. Weill and C. Delmas, *J. Electrochem. Soc.*, 2013, **160**, A786–A792.
90 H. Koga, L. Croguennec, M. Ménétrier, P. Mannessiez, F. Weill and C. Delmas, *J. Power Sources*, 2013, **236**, 250–258.
91 H. Koga, L. Croguennec, M. Ménétrier, P. Mannessiez, F. Weill, C. Delmas and S. Belin, *J. Phys. Chem. C*, 2014, **118**, 5700–5709.
92 E. McCalla, J. Li, A. W. Rowe and J. R. Dahn, *J. Electrochem. Soc.*, 2014, **161**, A606–A613.
93 G. Ceder, Y. M. Chiang, D. R. Sadoway, M. K. Aydinol, Y. I. Jang and B. Huang, *Nature*, 1998, **392**, 694–696.
94 J. Rouxel, *Chem. – Eur. J.*, 1996, **2**, 1053–1059.
95 Z. Y. Wu, G. Ouvrard, S. Lemaux, P. Moreau, P. Gressier, F. Lemoigno and J. Rouxel, *Phys. Rev. Lett.*, 1996, **77**, 2101–2104.
96 P. Gard, C. Sourisseau, G. Ouvrard and R. Brec, *Solid State Ionics*, 1986, **20**, 231–238.
97 L. Blandeau, G. Ouvrard, Y. Calage, R. Brec and J. Rouxel, *J. Phys. C: Solid State Phys.*, 1987, **20**, 4271–7281.
98 L. A. Montoro, M. Abbate and J. M. Rosolen, *Electrochem. Solid-State Lett.*, 1999, **3**, 410.
99 W. S. Yoon, M. Balasubramanian, K. Y. Chung, X. Q. Yang, J. McBreen, C. P. Grey and D. A. Fischer, *J. Am. Chem. Soc.*, 2005, **127**, 17479–17487.
100 M. G. Kim, H. J. Shin, J.-H. Kim, S.-H. Park and Y.-K. Sun, *J. Electrochem. Soc.*, 2005, **152**, A1320.
101 Y. Koyama, I. Tanaka, M. Nagao and R. Kanno, *J. Power Sources*, 2009, **189**, 798–801.
102 R. Xiao, H. Li and L. Chen, *Chem. Mater.*, 2012, **24**, 4242–4251.
103 B. Li, R. Shao, H. Yan, L. An, B. Zhang, H. Wei, J. Ma, D. Xia and X. Han, *Adv. Funct. Mater.*, 2016, **26**, 1330–1337.
104 M. Saubanère, E. McCalla, J. M. Tarascon and M. L. Doublet, *Energy Environ. Sci.*, 2016, **9**, 984–991.
105 N. Yabuuchi, M. Takeuchi, M. Nakayama, H. Shiiba, M. Ogawa, K. Nakayama, T. Ohta, D. Endo, T. Ozaki,

T. Inamasu, K. Sato and S. Komaba, *Proc. Natl. Acad. Sci. U. S. A.*, 2015, **112**, 7650–7655.
106 S. L. Glazier, J. Li, J. Zhou, T. Bond and J. R. Dahn, *Chem. Mater.*, 2015, **27**, 7751–7756.
107 M. Tabuchi, A. Nakashima, H. Shigemura, K. Ado, H. Kobayashi, H. Sakaebe, K. Tatsumi, H. Kageyama, T. Nakamura and R. Kanno, *J. Mater. Chem.*, 2003, **13**, 1747.
108 E. McCalla, A. M. Abakumov, M. Saubanere, D. Foix, E. J. Berg, G. Rousse, M. L. Doublet, D. Gonbeau, P. Novak, G. Van Tendeloo, R. Dominko and J. M. Tarascon, *Science*, 2015, **350**, 1516–1521.
109 X. Rong, J. Liu, E. Hu, Y. Liu, Y. Wang, J. Wu, X. Yu, K. Page, Y.-S. Hu, W. Yang, H. Li, X.-Q. Yang, L. Chen and X. Huang, *Joule*, 2018, **2**, 125–140.
110 M. Sathiya, J. B. Leriche, E. Salager, D. Gourier, J. M. Tarascon and H. Vezin, *Nat. Commun.*, 2015, **6**, 6276.
111 W. Yang and T. P. Devereaux, *J. Power Sources*, 2018, **389**, 188–197.
112 B. Song, M. Tang, E. Hu, O. J. Borkiewicz, K. M. Wiaderek, Y. Zhang, N. D. Phillip, X. Liu, Z. Shadike, C. Li, L. Song, Y.-Y. Hu, M. Chi, G. M. Veith, X.-Q. Yang, J. Liu, J. Nanda, K. Page and A. Huq, *Chem. Mater.*, 2019, **31**, 3756–3765.
113 P. Rozier, M. Sathiya, A.-R. Paulraj, D. Foix, T. Desaunay, P.-L. Taberna, P. Simon and J.-M. Tarascon, *Electrochem. Commun.*, 2015, **53**, 29–32.
114 S. Francis Amalraj, B. Markovsky, D. Sharon, M. Talianker, E. Zinigrad, R. Persky, O. Haik, J. Grinblat, J. Lampert, M. Schulz-Dobrick, A. Garsuch, L. Burlaka and D. Aurbach, *Electrochim. Acta*, 2012, **78**, 32–39.
115 J. Bréger, M. Jiang, N. Dupré, Y. S. Meng, Y. Shao-Horn, G. Ceder and C. P. Grey, *J. Solid State Chem.*, 2005, **178**, 2575–2585.
116 Y. Nakao, K. Ozawa, Y. Nemoto, F. Uesugi, H. Fujii and T. Mochiku, *J. Ceram. Soc. Jpn.*, 2015, **123**, 589–594.
117 J. Bareno, C. H. Lei, J. G. Wen, S. H. Kang, I. Petrov and D. P. Abraham, *Adv. Mater.*, 2010, **22**, 1122–1127.
118 X. Yu, Y. Lyu, L. Gu, H. Wu, S.-M. Bak, Y. Zhou, K. Amine, S. N. Ehrlich, H. Li, K.-W. Nam and X.-Q. Yang, *Adv. Energy Mater.*, 2014, **4**, 1300950.
119 Y. N. Zhou, J. Ma, E. Hu, X. Yu, L. Gu, K. W. Nam, L. Chen, Z. Wang and X. Q. Yang, *Nat. Commun.*, 2014, **5**, 5381.
120 A. C. W. P. James and J. B. Goodenough, *J. Solid State Chem.*, 1988, **76**, 87–96.
121 M. Luo, S. Zheng, J. Wu, K. Zhou, W. Zuo, M. Feng, H. He, R. Liu, J. Zhu, G. Zhao, S. Chen, W. Yang, Z. Peng, Q. Wu and Y. Yang, *J. Mater. Chem. A*, 2020, **8**, 5115–5127.
122 E. Zhao, Q. Li, F. Meng, J. Liu, J. Wang, L. He, Z. Jiang, Q. Zhang, X. Yu, L. Gu, W. Yang, H. Li, F. Wang and X. Huang, *Angew. Chem., Int. Ed.*, 2019, **58**, 4323–4327.
123 A. Urban, I. Matts, A. Abdellahi and G. Ceder, *Adv. Energy Mater.*, 2016, **6**, 1600488.
124 J. L. Hodeau, M. Marezio, A. Santoro and R. S. Roth, *J. Solid State Chem.*, 1982, **45**, 170–179.
125 J.-S. Kim, C. S. Johnson, J. T. Vaughey, M. M. Thackeray, S. A. Hackney, W. Yoon and C. P. Grey, *Chem. Mater.*, 2004, **16**, 1996–2006.
126 P. E. Pearce, A. J. Perez, G. Rousse, M. Saubanere, D. Batuk, D. Foix, E. McCalla, A. M. Abakumov, G. Van Tendeloo, M. L. Doublet and J. M. Tarascon, *Nat. Mater.*, 2017, **16**, 580–586.
127 Y. Lyu, E. Hu, D. Xiao, Y. Wang, X. Yu, G. Xu, S. N. Ehrlich, K. Amine, L. Gu, X.-Q. Yang and H. Li, *Chem. Mater.*, 2017, **29**, 9053–9065.
128 M. Sathiya, A. M. Abakumov, D. Foix, G. Rousse, K. Ramesha, M. Saubanere, M. L. Doublet, H. Vezin, C. P. Laisa, A. S. Prakash, D. Gonbeau, G. VanTendeloo and J. M. Tarascon, *Nat. Mater.*, 2015, **14**, 230–238.
129 M. Sathiya, K. Ramesha, G. Rousse, D. Foix, D. Gonbeau, A. S. Prakash, M. L. Doublet, K. Hemalatha and J. M. Tarascon, *Chem. Mater.*, 2013, **25**, 1121–1131.
130 A. J. Perez, Q. Jacquet, D. Batuk, A. Iadecola, M. Saubanère, G. Rousse, D. Larcher, H. Vezin, M.-L. Doublet and J.-M. Tarascon, *Nat. Energy*, 2017, **2**, 954–962.
131 N. Yabuuchi, Y. Tahara, S. Komaba, S. Kitada and Y. Kajiya, *Chem. Mater.*, 2016, **28**, 416–419.
132 R. Hoffmann and R. Hoppe, *Z. Anorg. Allg. Chem.*, 1989, **573**, 157–169.
133 P. Jeżowski, K. Fic, O. Crosnier, T. Brousse and F. Béguin, *J. Mater. Chem. A*, 2016, **4**, 12609–12615.
134 R. A. House, L. Y. Jin, U. Maitra, K. Tsuruta, J. W. Somerville, D. P. Forstermann, F. Massel, L. Duda, M. R. Roberts and P. G. Bruce, *Energy Environ. Sci.*, 2018, **11**, 926–932.
135 S. Hoshino, A. M. Glushenkov, S. Ichikawa, T. Ozaki, T. Inamasu and N. Yabuuchi, *ACS Energy Lett.*, 2017, **2**, 733–738.
136 S. Zheng, F. Zheng, H. Liu, G. Zhong, J. Wu, M. Feng, Q. Wu, W. Zuo, C. Hong, Y. Chen, K. An, P. Liu, S. Wu and Y. Yang, *ACS Appl. Energy Mater.*, 2019, **2**, 5933–5944.
137 G. Vitins, E. A. Raekelboom, M. T. Weller and J. R. Owen, *J. Power Sources*, 2003, **119-121**, 938–942.
138 C. W. Park, S. H. Kim, K. S. Nahm, H. T. Chung, Y. S. Lee, J. H. Lee, S. Boo and J. Kim, *J. Alloys Compd.*, 2008, **449**, 343–348.
139 J. Rana, M. Stan, R. Kloepsch, J. Li, G. Schumacher, E. Welter, I. Zizak, J. Banhart and M. Winter, *Adv. Energy Mater.*, 2014, **4**, 1300998.
140 Y.-G. Lim, D. Kim, J.-M. Lim, J.-S. Kim, J.-S. Yu, Y.-J. Kim, D. Byun, M. Cho, K. Cho and M.-S. Park, *J. Mater. Chem. A*, 2015, **3**, 12377–12385.
141 J. Zheng, P. Xu, M. Gu, J. Xiao, N. D. Browning, P. Yan, C. Wang and J.-G. Zhang, *Chem. Mater.*, 2015, **27**, 1381–1390.
142 R. Chen, S. Ren, M. Knapp, D. Wang, R. Witter, M. Fichtner and H. Hahn, *Adv. Energy Mater.*, 2015, **5**, 1401814.
143 B. Qiu, M. Zhang, L. Wu, J. Wang, Y. Xia, D. Qian, H. Liu, S. Hy, Y. Chen, K. An, Y. Zhu, Z. Liu and Y. S. Meng, *Nat. Commun.*, 2016, **7**, 12108.
144 M. Freire, N. V. Kosova, C. Jordy, D. Chateigner, O. I. Lebedev, A. Maignan and V. Pralong, *Nat. Mater.*, 2016, **15**, 173–177.
145 T. Okumura, M. Shikano and H. Kobayashi, *J. Mater. Chem. A*, 2014, **2**, 11847–11856.

146 C. Zhan, Z. Yao, J. Lu, L. Ma, V. A. Maroni, L. Li, E. Lee, E. E. Alp, T. Wu, J. Wen, Y. Ren, C. Johnson, M. M. Thackeray, M. K. Y. Chan, C. Wolverton and K. Amine, *Nat. Energy*, 2017, **2**, 963–971.

147 M. Sathiya, K. Ramesha, G. Rousse, D. Foix, D. Gonbeau, K. Guruprakash, A. S. Prakash, M. L. Doublet and J. M. Tarascon, *Chem. Commun.*, 2013, **49**, 11376–11378.

148 E. McCalla, A. S. Prakash, E. Berg, M. Saubanère, A. M. Abakumov, D. Foix, B. Klobes, M.-T. Sougrati, G. Rousse, F. Lepoivre, S. Mariyappan, M.-L. Doublet, D. Gonbeau, P. Novak, G. Van Tendeloo, R. P. Hermann and J.-M. Tarascon, *J. Electrochem. Soc.*, 2015, **162**, A1341–A1351.

149 E. McCalla, A. Abakumov, G. Rousse, M. Reynaud, M. T. Sougrati, B. Budic, A. Mahmoud, R. Dominko, G. Van Tendeloo, R. P. Hermann and J.-M. Tarascon, *Chem. Mater.*, 2015, **27**, 1699–1708.

150 E. McCalla, M. T. Sougrati, G. Rousse, E. J. Berg, A. Abakumov, N. Recham, K. Ramesha, M. Sathiya, R. Dominko, G. Van Tendeloo, P. Novak and J. M. Tarascon, *J. Am. Chem. Soc.*, 2015, **137**, 4804–4814.

151 J. Lee, D.-H. Seo, M. Balasubramanian, N. Twu, X. Li and G. Ceder, *Energy Environ. Sci.*, 2015, **8**, 3255–3265.

152 N. Yabuuchi, M. Nakayama, M. Takeuchi, S. Komaba, Y. Hashimoto, T. Mukai, H. Shiiba, K. Sato, Y. Kobayashi, A. Nakao, M. Yonemura, K. Yamanaka, K. Mitsuhara and T. Ohta, *Nat. Commun.*, 2016, **7**, 13814.

153 T. Matsuhara, Y. Tsuchiya, K. Yamanaka, K. Mitsuhara, T. Ohta and N. Yabuuchi, *Electrochemistry*, 2016, **84**, 797–801.

154 J. Lee, D. A. Kitchaev, D. H. Kwon, C. W. Lee, J. K. Papp, Y. S. Liu, Z. Lun, R. J. Clement, T. Shi, B. D. McCloskey, J. Guo, M. Balasubramanian and G. Ceder, *Nature*, 2018, **556**, 185–190.

155 Z. N. Taylor, A. J. Perez, J. A. Coca-Clemente, F. Braga, N. E. Drewett, M. J. Pitcher, W. J. Thomas, M. S. Dyer, C. Collins, M. Zanella, T. Johnson, S. Day, C. Tang, V. R. Dhanak, J. B. Claridge, L. J. Hardwick and M. J. Rosseinsky, *J. Am. Chem. Soc.*, 2019, **141**, 7333–7346.

156 W. H. Kan, C. Wei, D. Chen, T. Bo, B. T. Wang, Y. Zhang, Y. Tian, J. S. Lee, Y. Liu and G. Chen, *Adv. Funct. Mater.*, 2019, **29**, 1808294.

157 N. Li, S. Hwang, M. Sun, Y. Fu, V. S. Battaglia, D. Su and W. Tong, *Adv. Energy Mater.*, 2019, **9**, 1902258.

158 N. Kuganathan, A. Kordatos and A. Chroneos, *Sci. Rep.*, 2019, **9**, 550.

159 S. Zheng, K. Zhou, F. Zheng, H. Liu, G. Zhong, W. Zuo, N. Xu, G. Zhao, M. Luo, J. Wu, C. Zhang, Z. Zhang, S. Wu and Y. Yang, *ACS Appl. Mater. Interfaces*, 2020, **12**, 40347–40354.

160 K. A. Jarvis, Z. Deng, L. F. Allard, A. Manthiram and P. J. Ferreira, *Chem. Mater.*, 2011, **23**, 3614–3621.

161 K. Numata, C. Sakaki and S. Yamanaka, *Chem. Lett.*, 1997, 725–726.

162 W.-S. Yoon, S. Iannopollo, C. P. Grey, D. Carlier, J. Gorman, J. Reed and G. Ceder, *Electrochem. Solid-State Lett.*, 2004, **7**, A167.

163 Y. S. Meng, G. Ceder, C. P. Grey, W. S. Yoon, M. Jiang, J. Bréger and Y. Shao-Horn, *Chem. Mater.*, 2005, **17**, 2386–2394.

164 H. Koga, L. Croguennec, P. Mannessiez, M. Ménétrier, F. Weill, L. Bourgeois, M. Duttine, E. Suard and C. Delmas, *J. Phys. Chem. C*, 2012, **116**, 13497–13506.

165 J. Bareño, M. Balasubramanian, S. H. Kang, J. G. Wen, C. H. Lei, S. V. Pol, I. Petrov and D. P. Abraham, *Chem. Mater.*, 2011, **23**, 2039–2050.

166 H. Liu, Y. Chen, S. Hy, K. An, S. Venkatachalam, D. Qian, M. Zhang and Y. S. Meng, *Adv. Energy Mater.*, 2016, **6**, 1502143.

167 D. Mohanty, J. Li, D. P. Abraham, A. Huq, E. A. Payzant, D. L. Wood and C. Daniel, *Chem. Mater.*, 2014, **26**, 6272–6280.

168 C. Genevois, H. Koga, L. Croguennec, M. Ménétrier, C. Delmas and F. Weill, *J. Phys. Chem. C*, 2014, **119**, 75–83.

169 H. Yu, R. Ishikawa, Y. G. So, N. Shibata, T. Kudo, H. Zhou and Y. Ikuhara, *Angew. Chem., Int. Ed.*, 2013, **52**, 5969–5973.

170 A. Ito, Y. Sato, T. Sanada, T. Ohwaki, M. Hatano, H. Horie and Y. Ohsawa, *Electrochemistry*, 2010, **78**, 380–383.

171 M. Gu, A. Genc, I. Belharouak, D. Wang, K. Amine, S. Thevuthasan, D. R. Baer, J.-G. Zhang, N. D. Browning, J. Liu and C. Wang, *Chem. Mater.*, 2013, **25**, 2319–2326.

172 A. K. Shukla, Q. M. Ramasse, C. Ophus, H. Duncan, F. Hage and G. Chen, *Nat. Commun.*, 2015, **6**, 8711.

173 A. K. Shukla, Q. M. Ramasse, C. Ophus, D. M. Kepaptsoglou, F. S. Hage, C. Gammer, C. Bowling, P. A. H. Gallegos and S. Venkatachalam, *Energy Environ. Sci.*, 2018, **11**, 830–840.

174 A. Boulineau, L. Croguennec, C. Delmas and F. Weill, *Chem. Mater.*, 2009, **21**, 4216–4222.

175 E. Zhao, M. Zhang, X. Wang, E. Hu, J. Liu, X. Yu, M. Olguin, T. A. Wynn, Y. S. Meng, K. Page, F. Wang, H. Li, X.-Q. Yang, X. Huang and L. Chen, *Energy Storage Mater.*, 2020, **24**, 384–393.

176 K. A. Jarvis, Z. Deng, L. F. Allard, A. Manthiram and P. J. Ferreira, *J. Mater. Chem.*, 2012, **22**, 11550.

177 S. Laha, S. Natarajan, J. Gopalakrishnan, E. Moran, R. Saez-Puche, M. A. Alario-Franco, A. J. Dos Santos-Garcia, J. C. Perez-Flores, A. Kuhn and F. Garcia-Alvarado, *Phys. Chem. Chem. Phys.*, 2015, **17**, 3749–3760.

178 G. Assat, D. Foix, C. Delacourt, A. Iadecola, R. Dedryvere and J. M. Tarascon, *Nat. Commun.*, 2017, **8**, 2219.

179 M. Oishi, C. Yogi, I. Watanabe, T. Ohta, Y. Orikasa, Y. Uchimoto and Z. Ogumi, *J. Power Sources*, 2015, **276**, 89–94.

180 M. Oishi, K. Yamanaka, I. Watanabe, K. Shimoda, T. Matsunaga, H. Arai, Y. Ukyo, Y. Uchimoto, Z. Ogumi and T. Ohta, *J. Mater. Chem. A*, 2016, **4**, 9293–9302.

181 K. Luo, M. R. Roberts, N. Guerrini, N. Tapia-Ruiz, R. Hao, F. Massel, D. M. Pickup, S. Ramos, Y. S. Liu, J. Guo, A. V. Chadwick, L. C. Duda and P. G. Bruce, *J. Am. Chem. Soc.*, 2016, **138**, 11211–11218.

182 H. Chen and M. S. Islam, *Chem. Mater.*, 2016, **28**, 6656–6663.

183 X. Li, Y. Qiao, S. Guo, Z. Xu, H. Zhu, X. Zhang, Y. Yuan, P. He, M. Ishida and H. Zhou, *Adv. Mater.*, 2018, **30**, e1705197.

184 X. Li, Y. Qiao, S. Guo, K. Jiang, M. Ishida and H. Zhou, *Adv. Mater.*, 2019, **31**, e1807825.
185 J. Hong, W. E. Gent, P. Xiao, K. Lim, D. H. Seo, J. Wu, P. M. Csernica, C. J. Takacs, D. Nordlund, C. J. Sun, K. H. Stone, D. Passarello, W. Yang, D. Prendergast, G. Ceder, M. F. Toney and W. C. Chueh, *Nat. Mater.*, 2019, **18**, 256–265.
186 N. Yabuuchi, K. Yoshii, S. T. Myung, I. Nakai and S. Komaba, *J. Am. Chem. Soc.*, 2011, **133**, 4404–4419.
187 E. Hu, X. Yu, R. Lin, X. Bi, J. Lu, S. Bak, K.-W. Nam, H. L. Xin, C. Jaye, D. A. Fischer, K. Amine and X.-Q. Yang, *Nat. Energy*, 2018, **3**, 690–698.
188 C. R. Fell, D. Qian, K. J. Carroll, M. Chi, J. L. Jones and Y. S. Meng, *Chem. Mater.*, 2013, **25**, 1621–1629.
189 D. Qian, B. Xu, M. Chi and Y. S. Meng, *Phys. Chem. Chem. Phys.*, 2014, **16**, 14665–14668.
190 Y. Okamoto, *J. Electrochem. Soc.*, 2011, **159**, A152–A157.
191 H. C. Shim, D. Kim, D. Shin, S. Hyun, C. S. Woo, T. Yu and J. P. Ahn, *Phys. Chem. Chem. Phys.*, 2017, **19**, 1268–1275.
192 P. Yan, J. Zheng, Z. K. Tang, A. Devaraj, G. Chen, K. Amine, J. G. Zhang, L. M. Liu and C. Wang, *Nat. Nanotechnol.*, 2019, **14**, 602–608.
193 M. Jiang, B. Key, Y. S. Meng and C. P. Grey, *Chem. Mater.*, 2009, **21**, 2733–2745.
194 C. P. Grey, W.-S. Yoon, J. Reed and G. Ceder, *Electrochem. Solid-State Lett.*, 2004, **7**, A290.
195 D. Y. W. Yu, K. Yanagida, Y. Kato and H. Nakamura, *J. Electrochem. Soc.*, 2009, **156**, A417.
196 J. Li, R. Shunmugasundaram, R. Doig and J. R. Dahn, *Chem. Mater.*, 2015, **28**, 162–171.
197 W.-S. Yoon, N. Kim, X.-Q. Yang, J. McBreen and C. P. Grey, *J. Power Sources*, 2003, **119-121**, 649–653.
198 A. Boulineau, L. Simonin, J.-F. Colin, E. Canévet, L. Daniel and S. Patoux, *Chem. Mater.*, 2012, **24**, 3558–3566.
199 D. Mohanty, S. Kalnaus, R. A. Meisner, K. J. Rhodes, J. Li, E. A. Payzant, D. L. Wood and C. Daniel, *J. Power Sources*, 2013, **229**, 239–248.
200 L. Simonin, J.-F. Colin, V. Ranieri, E. Canévet, J.-F. Martin, C. Bourbon, C. Baehtz, P. Strobel, L. Daniel and S. Patoux, *J. Mater. Chem.*, 2012, **22**, 11316.
201 A. Ito, Y. Sato, T. Sanada, M. Hatano, H. Horie and Y. Ohsawa, *J. Power Sources*, 2011, **196**, 6828–6834.
202 P. Yan, J. Zheng, J. G. Zhang and C. Wang, *Nano Lett.*, 2017, **17**, 3946–3951.
203 B. Xu, C. R. Fell, M. Chi and Y. S. Meng, *Energy Environ. Sci.*, 2011, **4**, 2223.
204 A. Boulineau, L. Simonin, J. F. Colin, C. Bourbon and S. Patoux, *Nano Lett.*, 2013, **13**, 3857–3863.
205 P. Yan, A. Nie, J. Zheng, Y. Zhou, D. Lu, X. Zhang, R. Xu, I. Belharouak, X. Zu, J. Xiao, K. Amine, J. Liu, F. Gao, R. Shahbazian-Yassar, J. G. Zhang and C. M. Wang, *Nano Lett.*, 2015, **15**, 514–522.
206 M. Gu, I. Belharouak, J. Zheng, H. Wu, J. Xiao, A. Genc, K. Amine, S. Thevuthasan, D. R. Baer, J. G. Zhang, N. D. Browning, J. Liu and C. Wang, *ACS Nano*, 2013, **7**, 760–767.
207 E. Zhao, L. He, B. Wang, X. Li, J. Zhang, Y. Wu, J. Chen, S. Zhang, T. Liang, Y. Chen, X. Yu, H. Li, L. Chen, X. Huang, H. Chen and F. Wang, *Energy Storage Mater.*, 2019, **16**, 354–363.
208 R. Wang, X. Li, L. Liu, J. Lee, D.-H. Seo, S.-H. Bo, A. Urban and G. Ceder, *Electrochem. Commun.*, 2015, **60**, 70–73.
209 W. H. Kan, D. Chen, J. K. Papp, A. K. Shukla, A. Huq, C. M. Brown, B. D. McCloskey and G. Chen, *Chem. Mater.*, 2018, **30**, 1655–1666.
210 D. Chen, W. H. Kan and G. Chen, *Adv. Energy Mater.*, 2019, **9**, 1901255.
211 J. Lee, J. K. Papp, R. J. Clement, S. Sallis, D. H. Kwon, T. Shi, W. Yang, B. D. McCloskey and G. Ceder, *Nat. Commun.*, 2017, **8**, 981.
212 N. Yabuuchi, M. Takeuchi, S. Komaba, S. Ichikawa, T. Ozaki and T. Inamasu, *Chem. Commun.*, 2016, **52**, 2051–2054.
213 Z. Lun, B. Ouyang, D. A. Kitchaev, R. J. Clément, J. K. Papp, M. Balasubramanian, Y. Tian, T. Lei, T. Shi, B. D. McCloskey, J. Lee and G. Ceder, *Adv. Energy Mater.*, 2019, **9**, 1802959.
214 Q. Jacquet, A. Iadecola, M. Saubanere, H. Li, E. J. Berg, G. Rousse, J. Cabana, M. L. Doublet and J. M. Tarascon, *J. Am. Chem. Soc.*, 2019, **141**, 11452–11464.
215 B. Huang, R. Wang, Y. Gong, B. He and H. Wang, *Front. Chem.*, 2019, **7**, 107.
216 Y. Qian, P. Niehoff, M. Börner, M. Grützke, X. Mönnighoff, P. Behrends, S. Nowak, M. Winter and F. M. Schappacher, *J. Power Sources*, 2016, **329**, 31–40.
217 S. Nowak and M. Winter, *J. Electrochem. Soc.*, 2015, **162**, A2500–A2508.
218 J. Wu, Z. Zhuo, X. Rong, K. Dai, Z. Lebens-Higgins, S. Sallis, F. Pan, L. F. J. Piper, G. Liu, Y. D. Chuang, Z. Hussain, Q. Li, R. Zeng, Z. X. Shen and W. Yang, *Sci. Adv.*, 2020, **6**, eaaw3871.
219 H. Xu, S. Deng and G. Chen, *J. Mater. Chem. A*, 2014, **2**, 15015–15021.
220 X. Jin, Q. Xu, H. Liu, X. Yuan and Y. Xia, *Electrochim. Acta*, 2014, **136**, 19–26.
221 C.-C. Wang, Y.-C. Lin and P.-H. Chou, *RSC Adv.*, 2015, **5**, 68919–68928.
222 H. Guo, Y. Xia, H. Zhao, C. Yin, K. Jia, F. Zhao and Z. Liu, *Ceram. Int.*, 2017, **43**, 13845–13852.
223 R.-P. Qing, J.-L. Shi, D.-D. Xiao, X.-D. Zhang, Y.-X. Yin, Y.-B. Zhai, L. Gu and Y.-G. Guo, *Adv. Energy Mater.*, 2016, **6**, 1501914.
224 J. Li, C. Zhan, J. Lu, Y. Yuan, R. Shahbazian-Yassar, X. Qiu and K. Amine, *ACS Appl. Mater. Interfaces*, 2015, **7**, 16040–16045.
225 Z. Q. Deng and A. Manthiram, *J. Phys. Chem. C*, 2011, **115**, 7097–7103.
226 J. Zhao, Z. Wang, H. Guo, X. Li, Z. He and T. Li, *Ceram. Int.*, 2015, **41**, 11396–11401.
227 Z. He, Z. Wang, H. Chen, Z. Huang, X. Li, H. Guo and R. Wang, *J. Power Sources*, 2015, **299**, 334–341.
228 Z. Ma, J. Huang, J. Quan, L. Mei, J. Guo and D. Li, *RSC Adv.*, 2016, **6**, 20522–20531.

229 Q. Li, G. Li, C. Fu, D. Luo, J. Fan and L. Li, *ACS Appl. Mater. Interfaces*, 2014, **6**, 10330–10341.
230 Y. Zhao, M. Xia, X. Hu, Z. Zhao, Y. Wang and Z. Lv, *Electrochim. Acta*, 2015, **174**, 1167–1174.
231 C. P. Laisa, R. N. Ramesha and K. Ramesha, *Electrochim. Acta*, 2017, **256**, 10–18.
232 N. Li, R. An, Y. Su, F. Wu, L. Bao, L. Chen, Y. Zheng, H. Shou and S. Chen, *J. Mater. Chem. A*, 2013, **1**, 9760.
233 L. Sun, X. Yi, X. Ren, P. Zhang and J. Liu, *J. Electrochem. Soc.*, 2016, **163**, A766–A772.
234 R. Yu, G. Wang, M. Liu, X. Zhang, X. Wang, H. Shu, X. Yang and W. Huang, *J. Power Sources*, 2016, **335**, 65–75.
235 D. Uzun, *Solid State Ionics*, 2015, **281**, 73–81.
236 L. Pan, Y. Xia, B. Qiu, H. Zhao, H. Guo, K. Jia, Q. Gu and Z. Liu, *J. Power Sources*, 2016, **327**, 273–280.
237 J. Zheng, X. Wu and Y. Yang, *Electrochim. Acta*, 2013, **105**, 200–208.
238 A. Kapylou, J. H. Song, A. Missiul, D. J. Ham, D. H. Kim, S. Moon and J. H. Park, *ChemPhysChem*, 2018, **19**, 116–122.
239 H. Yan, B. Li, Z. Yu, W. Chu and D. Xia, *J. Phys. Chem. C*, 2017, **121**, 7155–7163.
240 B. Li, H. Yan, J. Ma, P. Yu, D. Xia, W. Huang, W. Chu and Z. Wu, *Adv. Funct. Mater.*, 2014, **24**, 5112–5118.
241 Y. Liu, D. Ning, L. Zheng, Q. Zhang, L. Gu, R. Gao, J. Zhang, A. Franz, G. Schumacher and X. Liu, *J. Power Sources*, 2018, **375**, 1–10.
242 S.-T. Myung, K. Izumi, S. Komaba, H. Yashiro, H. J. Bang, Y.-K. Sun and N. Kumagai, *J. Phys. Chem. C*, 2007, **111**, 4061–4067.
243 Z. Wang, E. Liu, L. Guo, C. Shi, C. He, J. Li and N. Zhao, *Surf. Coat. Technol.*, 2013, **235**, 570–576.
244 E. Han, Y. Li, L. Zhu and L. Zhao, *Solid State Ionics*, 2014, **255**, 113–119.
245 T. Zhao, S. Chen, R. Chen, L. Li, X. Zhang, M. Xie and F. Wu, *ACS Appl. Mater. Interfaces*, 2014, **6**, 21711–21720.
246 K. Yang, Y. Liu, B. Niu, Z. Yang and J. Li, *Ionics*, 2018, **25**, 2027–2034.
247 J. Wang, X. He, R. Kloepsch, S. Wang, B. Hoffmann, S. Jeong, Y. Yang and J. Li, *Energy Technol.*, 2014, **2**, 188–193.
248 J. M. Zheng, Z. R. Zhang, X. B. Wu, Z. X. Dong, Z. Zhu and Y. Yang, *J. Electrochem. Soc.*, 2008, **155**, A775.
249 H. Liu, C. Du, G. Yin, B. Song, P. Zuo, X. Cheng, Y. Ma and Y. Gao, *J. Mater. Chem. A*, 2014, **2**, 15640.
250 S. Zhao, B. Sun, K. Yan, J. Zhang, C. Wang and G. Wang, *ACS Appl. Mater. Interfaces*, 2018, **10**, 33260–33268.
251 Z. Wang, E. Liu, C. He, C. Shi, J. Li and N. Zhao, *J. Power Sources*, 2013, **236**, 25–32.
252 Y. Liu, X. Huang, Q. Qiao, Y. Wang, S. Ye and X. Gao, *Electrochim. Acta*, 2014, **147**, 696–703.
253 W. Liu, P. Oh, X. Liu, S. Myeong, W. Cho and J. Cho, *Adv. Energy Mater.*, 2015, **5**, 1500274.
254 F. Zheng, C. Yang, X. Xiong, J. Xiong, R. Hu, Y. Chen and M. Liu, *Angew. Chem., Int. Ed.*, 2015, **54**, 13058–13062.
255 F. Wu, X. Zhang, T. Zhao, L. Li, M. Xie and R. Chen, *ACS Appl. Mater. Interfaces*, 2015, **7**, 3773–3781.
256 X. Zhang, X. Xie, R. Yu, J. Zhou, Y. Huang, S. Cao, Y. Wang, K. Tang, C. Wu and X. Wang, *ACS Appl. Energy Mater.*, 2019, **2**, 3532–3541.
257 K. Gao, S.-X. Zhao, S.-T. Guo and C.-W. Nan, *Electrochim. Acta*, 2016, **206**, 1–9.
258 S. J. Shi, J. P. Tu, Y. J. Mai, Y. Q. Zhang, C. D. Gu and X. L. Wang, *Electrochim. Acta*, 2012, **63**, 112–117.
259 H. Liu, C. Chen, C. Du, X. He, G. Yin, B. Song, P. Zuo, X. Cheng, Y. Ma and Y. Gao, *J. Mater. Chem. A*, 2015, **3**, 2634–2641.
260 D. Gao, Z. Zeng, H. Mi, L. Sun, X. Ren, P. Zhang and Y. Li, *J. Mater. Chem. A*, 2019, **7**, 23964–23972.
261 J. Zhang, Q. Lu, J. Fang, J. Wang, J. Yang and Y. NuLi, *ACS Appl. Mater. Interfaces*, 2014, **6**, 17965–17973.
262 J. Zheng, M. Gu, J. Xiao, B. J. Polzin, P. Yan, X. Chen, C. Wang and J.-G. Zhang, *Chem. Mater.*, 2014, **26**, 6320–6327.
263 R. W. Schmitz, P. Murmann, R. Schmitz, R. Müller, L. Krämer, J. Kasnatscheew, P. Isken, P. Niehoff, S. Nowak, G.-V. Röschenthaler, N. Ignatiev, P. Sartori, S. Passerini, M. Kunze, A. Lex-Balducci, C. Schreiner, I. Cekic-Laskovic and M. Winter, *Prog. Solid State Chem.*, 2014, **42**, 65–84.
264 J. Li, S. Jeong, R. Kloepsch, M. Winter and S. Passerini, *J. Power Sources*, 2013, **239**, 490–495.
265 Z. Chen and K. Amine, *J. Electrochem. Soc.*, 2006, **153**, A1221.
266 J. Liu, Z. Chen, S. Busking, I. Belharouak and K. Amine, *J. Power Sources*, 2007, **174**, 852–855.
267 Q. Wu, W. Lu, M. Miranda, T. K. Honaker-Schroeder, K. Y. Lakhsassi and D. Dees, *Electrochem. Commun.*, 2012, **24**, 78–81.
268 M. Xu, L. Hao, Y. Liu, W. Li, L. Xing and B. Li, *J. Phys. Chem. C*, 2011, **115**, 6085–6094.
269 X. Zheng, X. Wang, X. Cai, L. Xing, M. Xu, Y. Liao, X. Li and W. Li, *ACS Appl. Mater. Interfaces*, 2016, **8**, 30116–30125.
270 J. Pires, L. Timperman, A. Castets, J. S. Peña, E. Dumont, S. Levasseur, R. Dedryvère, C. Tessier and M. Anouti, *RSC Adv.*, 2015, **5**, 42088–42094.
271 Y. Zhu, X. Luo, M. Xu, L. Zhang, L. Yu, W. Fan and W. Li, *J. Power Sources*, 2016, **317**, 65–73.
272 Z. Zhou, Y. Ma, L. Wang, P. Zuo, X. Cheng, C. Du, G. Yin and Y. Gao, *Electrochim. Acta*, 2016, **216**, 44–50.
273 J. G. Han, S. J. Lee, J. Lee, J. S. Kim, K. T. Lee and N. S. Choi, *ACS Appl. Mater. Interfaces*, 2015, **7**, 8319–8329.
274 S. Tan, Z. Zhang, Y. Li, Y. Li, J. Zheng, Z. Zhou and Y. Yang, *J. Electrochem. Soc.*, 2012, **160**, A285–A292.
275 J. Pires, A. Castets, L. Timperman, J. Santos-Peña, E. Dumont, S. Levasseur, C. Tessier, R. Dedryvère and M. Anouti, *J. Power Sources*, 2015, **296**, 413–425.
276 D. J. Lee, D. Im, Y.-G. Ryu, S. Lee, J. Yoon, J. Lee, W. Choi, I. Jung, S. Lee and S.-G. Doo, *J. Power Sources*, 2013, **243**, 831–835.
277 W. Tu, P. Xia, X. Zheng, C. Ye, M. Xu and W. Li, *J. Power Sources*, 2017, **341**, 348–356.
278 M. Winter, *Z. Phys. Chem.*, 2009, **223**, 1395–1406.

279 J. C. Knight, P. Nandakumar, W. H. Kan and A. Manthiram, *J. Mater. Chem. A*, 2015, **3**, 2006–2011.
280 Y. Wang, Z. Yang, Y. Qian, L. Gu and H. Zhou, *Adv. Mater.*, 2015, **27**, 3915–3920.
281 Y. Zang, C.-X. Ding, X.-C. Wang, Z.-Y. Wen and C.-H. Chen, *Electrochim. Acta*, 2015, **168**, 234–239.
282 J. Du, Z. Shan, K. Zhu, X. Liu, J. Tian and H. Du, *J. Solid State Electrochem.*, 2014, **19**, 1037–1044.
283 X. Li, H. Xin, Y. Liu, D. Li, X. Yuan and X. Qin, *RSC Adv.*, 2015, **5**, 45351–45358.
284 Z. Zheng, X.-D. Guo, Y.-J. Zhong, W.-B. Hua, C.-H. Shen, S.-L. Chou and X.-S. Yang, *Electrochim. Acta*, 2016, **188**, 336–343.
285 J. Liu, S. Wang, Z. Ding, R. Zhou, Q. Xia, J. Zhang, L. Chen, W. Wei and P. Wang, *ACS Appl. Mater. Interfaces*, 2016, **8**, 18008–18017.
286 X. Feng, Y. Gao, L. Ben, Z. Yang, Z. Wang and L. Chen, *J. Power Sources*, 2016, **317**, 74–80.
287 P. K. Nayak, J. Grinblat, M. Levi, E. Levi, S. Kim, J. W. Choi and D. Aurbach, *Adv. Energy Mater.*, 2016, **6**, 1502398.
288 C. Lu, S. Yang, H. Wu, Y. Zhang, X. Yang and T. Liang, *Electrochim. Acta*, 2016, **209**, 448–455.
289 X. Jin, Q. Xu, X. Liu, X. Yuan and H. Liu, *Ionics*, 2016, **22**, 1369–1376.
290 B. Guo, J. Zhao, X. Fan, W. Zhang, S. Li, Z. Yang, Z. Chen and W. Zhang, *Electrochim. Acta*, 2017, **236**, 171–179.
291 J. Meng, Z. Wang, L. Xu, H. Xu, S. Zhang and Q. Yan, *J. Electrochem. Soc.*, 2017, **164**, A2594–A2602.
292 R. N. Ramesha, C. P. Laisa and K. Ramesha, *Electrochim. Acta*, 2017, **249**, 377–386.
293 M. Li, Y. Zhou, X. Wu, L. Duan, C. Zhang, F. Zhang and D. He, *Electrochim. Acta*, 2018, **275**, 18–24.
294 J. Huang, H. Liu, T. Hu, Y. S. Meng and J. Luo, *J. Power Sources*, 2018, **375**, 21–28.
295 L. Ming, B. Zhang, Y. Cao, J. F. Zhang, C. H. Wang, X. W. Wang and H. Li, *Front. Chem.*, 2018, **6**, 76.
296 H. Li, H. Guo, Z. Wang, J. Wang, X. Li, N. Chen and W. Gui, *Int. J. Hydrogen Energy*, 2018, **43**, 11109–11119.
297 T. A. Wynn, C. Fang, M. Zhang, H. Liu, D. M. Davies, X. Wang, D. Lau, J. Z. Lee, B.-Y. Huang, K.-Z. Fung, C.-T. Ni and Y. S. Meng, *J. Mater. Chem. A*, 2018, **6**, 24651–24659.
298 Y. Liang, S. Li, J. Xie, L. Yang, W. Li, C. Li, L. Ai, X. Fu, X. Cui and X. Shangguan, *New J. Chem.*, 2019, **43**, 12004–12012.
299 B. Li, X. Wang, Y. Gao, B. Wang, J. Qiu, X. Cheng and D. Dai, *J. Materiomics*, 2019, **5**, 149–155.
300 L. Bao, Z. Yang, L. Chen, Y. Su, Y. Lu, W. Li, F. Yuan, J. Dong, Y. Fang, Z. Ji, C. Shi and W. Feng, *ChemSusChem*, 2019, **12**, 2294–2301.
301 M.-J. Wang, F.-D. Yu, G. Sun, J. Wang, J.-G. Zhou, D.-M. Gu and Z.-B. Wang, *J. Mater. Chem. A*, 2019, **7**, 8302–8314.
302 M. Li, H. Wang, L. Zhao, Y. Zhou, F. Zhang and D. He, *J. Alloys Compd.*, 2019, **782**, 451–460.
303 Z. Yu, F. Ning, B. Li, Z. Sun, W. Chu and D. Xia, *J. Phys. Chem. C*, 2019, **123**, 18870–18876.
304 G. Chen, J. An, Y. Meng, C. Yuan, B. Matthews, F. Dou, L. Shi, Y. Zhou, P. Song, G. Wu and D. Zhang, *Nano Energy*, 2019, **57**, 157–165.
305 J. M. Zheng, J. Li, Z. R. Zhang, X. J. Guo and Y. Yang, *Solid State Ionics*, 2008, **179**, 1794–1799.
306 F. Wu, N. Li, Y. Su, H. Lu, L. Zhang, R. An, Z. Wang, L. Bao and S. Chen, *J. Mater. Chem.*, 2012, **22**, 1489–1497.
307 S. K. Martha, J. Nanda, Y. Kim, R. R. Unocic, S. Pannala and N. J. Dudney, *J. Mater. Chem. A*, 2013, **1**, 5587.
308 Y. Wu, J. Ming, L. Zhuo, Y. Yu and F. Zhao, *Electrochim. Acta*, 2013, **113**, 54–62.
309 B. Qiu, J. Wang, Y. Xia, Z. Wei, S. Han and Z. Liu, *ACS Appl. Mater. Interfaces*, 2014, **6**, 9185–9193.
310 C. Lu, H. Wu, Y. Zhang, H. Liu, B. Chen, N. Wu and S. Wang, *J. Power Sources*, 2014, **267**, 682–691.
311 F. Wu, N. Li, Y. Su, L. Zhang, L. Bao, J. Wang, L. Chen, Y. Zheng, L. Dai, J. Peng and S. Chen, *Nano Lett.*, 2014, **14**, 3550–3555.
312 H. Liu, D. Qian, M. G. Verde, M. Zhang, L. Baggetto, K. An, Y. Chen, K. J. Carroll, D. Lau, M. Chi, G. M. Veith and Y. S. Meng, *ACS Appl. Mater. Interfaces*, 2015, **7**, 19189–19200.
313 E. Zhao, X. Liu, H. Zhao, X. Xiao and Z. Hu, *Chem. Commun.*, 2015, **51**, 9093–9096.
314 M. Xu, Z. Chen, L. Li, H. Zhu, Q. Zhao, L. Xu, N. Peng and L. Gong, *J. Power Sources*, 2015, **281**, 444–454.
315 F. He, X. Wang, C. Du, A. P. Baker, J. Wu and X. Zhang, *Electrochim. Acta*, 2015, **153**, 484–491.
316 H. Liu, J. Huang, D. Qian, S. Hy, C. Fang, J. Luo and Y. S. Meng, *J. Electrochem. Soc.*, 2016, **163**, A971–A973.
317 Y. Lee, J. Lee, K. Y. Lee, J. Mun, J. K. Lee and W. Choi, *J. Power Sources*, 2016, **315**, 284–293.
318 S.-J. Kim, M.-C. Kim, D.-H. Kwak, D.-M. Kim, G.-H. Lee, H.-S. Choe and K.-W. Park, *J. Power Sources*, 2016, **304**, 119–127.
319 D. Chen, F. Zheng, L. Li, M. Chen, X. Zhong, W. Li and L. Lu, *J. Power Sources*, 2017, **341**, 147–155.
320 Z. Wang, S. Luo, J. Ren, D. Wang and X. Qi, *Appl. Surf. Sci.*, 2016, **370**, 437–444.
321 Y. Liu, Z. Zhang, Y. Fu, Q. Wang, J. Pan, M. Su and V. S. Battaglia, *J. Alloys Compd.*, 2016, **685**, 523–532.
322 C. Chen, T. Geng, C. Du, P. Zuo, X. Cheng, Y. Ma and G. Yin, *J. Power Sources*, 2016, **331**, 91–99.
323 L. L. Zhang, J. J. Chen, S. Cheng and H. F. Xiang, *Ceram. Int.*, 2016, **42**, 1870–1878.
324 K. Park, D. Yeon, J. H. Kim, J.-H. Park, S. Doo and B. Choi, *J. Power Sources*, 2017, **360**, 453–459.
325 J. Zeng, Y. Liu, J. Wu, Y. Cui, A. Baker, D. Qu, H. Zhang, M. Lavorgna and X. Zhang, *Electrochim. Acta*, 2017, **247**, 617–625.
326 S. Liu, Z. Wang, Y. Huang, Z. Ni, J. Bai, S. Kang, Y. Wang and X. Li, *J. Alloys Compd.*, 2018, **731**, 636–645.
327 F. Wu, Q. Li, L. Bao, Y. Zheng, Y. Lu, Y. Su, J. Wang, S. Chen, R. Chen and J. Tian, *Electrochim. Acta*, 2018, **260**, 986–993.
328 X.-D. Zhang, J.-L. Shi, J.-Y. Liang, Y.-X. Yin, J.-N. Zhang, X.-Q. Yu and Y.-G. Guo, *Adv. Mater.*, 2018, **30**, 1801751.
329 C.-x. Zhou, P.-b. Wang, B. Zhang, J.-c. Zheng, Y.-y. Zhou, C.-h. Huang and X.-m. Xi, *J. Electrochem. Soc.*, 2018, **165**, A1648–A1655.

330 B. Niu, J. Li, Y. Liu, Z. Li and Z. Yang, *Ceram. Int.*, 2019, **45**, 12484–12494.
331 J. Zheng, D. Zhu, Y. Yang and Y. Fung, *Electrochim. Acta*, 2012, **59**, 14–22.
332 Z. D. Li, Y. C. Zhang, H. F. Xiang, X. H. Ma, Q. F. Yuan, Q. S. Wang and C. H. Chen, *J. Power Sources*, 2013, **240**, 471–475.
333 J. Zhang, J. Wang, J. Yang and Y. NuLi, *Electrochim. Acta*, 2014, **117**, 99–104.
334 J. Li, L. Xing, R. Zhang, M. Chen, Z. Wang, M. Xu and W. Li, *J. Power Sources*, 2015, **285**, 360–366.
335 Y. Ji, Z. Zhang, M. Gao, Y. Li, M. J. McDonald and Y. Yang, *J. Electrochem. Soc.*, 2015, **162**, A774–A780.
336 Y. Li, F. Lian, L. Ma, C. Liu, L. Yang, X. Sun and K. Chou, *Electrochim. Acta*, 2015, **168**, 261–270.
337 P. Hong, M. Xu, X. Zheng, Y. Zhu, Y. Liao, L. Xing, Q. Huang, H. Wan, Y. Yang and W. Li, *J. Power Sources*, 2016, **329**, 216–224.
338 W. Tu, L. Xing, P. Xia, M. Xu, Y. Liao and W. Li, *Electrochim. Acta*, 2016, **204**, 192–198.
339 A. Birrozzi, N. Laszczynski, M. Hekmatfar, J. von Zamory, G. A. Giffin and S. Passerini, *J. Power Sources*, 2016, **325**, 525–533.
340 S. H. Lim, W. Cho, Y.-J. Kim and T. Yim, *J. Power Sources*, 2016, **336**, 465–474.
341 J.-G. Han, I. Park, J. Cha, S. Park, S. Park, S. Myeong, W. Cho, S.-S. Kim, S. Y. Hong, J. Cho and N.-S. Choi, *ChemElectroChem*, 2017, **4**, 56–65.
342 L. Wang, Y. Ma, Q. Li, Z. Zhou, X. Cheng, P. Zuo, C. Du, Y. Gao and G. Yin, *J. Power Sources*, 2017, **361**, 227–236.
343 J.-G. Han, J. B. Lee, A. Cha, T. K. Lee, W. Cho, S. Chae, S. J. Kang, S. K. Kwak, J. Cho, S. Y. Hong and N.-S. Choi, *Energy Environ. Sci.*, 2018, **11**, 1552–1562.
344 Y. Zhuang, F. Du, L. Zhu, H. Cao, H. Dai, J. Adkins, Q. Zhou and J. Zheng, *Electrochim. Acta*, 2018, **290**, 220–227.
345 S. Lou, Y. Ma, Z. Zhou, H. Huo, P. Zuo, X. Cheng, X. Qu, Y. Gao, C. Du and G. Yin, *ChemElectroChem*, 2018, **5**, 1569–1575.
346 J. Lan, Q. Zheng, H. Zhou, J. Li, L. Xing, K. Xu, W. Fan, L. Yu and W. Li, *ACS Appl. Mater. Interfaces*, 2019, **11**, 28841–28850.
347 B. Qiu, M. Zhang, L. Wu, J. Wang, Y. Xia, D. Qian, H. Liu, S. Hy, Y. Chen, K. An, Y. Zhu, Z. Liu and Y. S. Meng, *Nat. Commun.*, 2016, **7**, 12108.
348 K. Zhang, B. Li, Y. Zuo, J. Song, H. Shang, F. Ning and D. Xia, *Electrochem. Energy Rev.*, 2019, **2**, 606–623.
349 I. Bloom, L. Trahey, A. Abouimrane, I. Belharouak, X. Zhang, Q. Wu, W. Lu, D. P. Abraham, M. Bettge, J. W. Elam, X. Meng, A. K. Burrell, C. Ban, R. Tenent, J. Nanda and N. Dudney, *J. Power Sources*, 2014, **249**, 509–514.
350 J. R. Croy, K. G. Gallagher, M. Balasubramanian, B. R. Long and M. M. Thackeray, *J. Electrochem. Soc.*, 2013, **161**, A318–A325.
351 D. Eum, B. Kim, S. J. Kim, H. Park, J. Wu, S. P. Cho, G. Yoon, M. H. Lee, S. K. Jung, W. Yang, W. M. Seong, K. Ku, O. Tamwattana, S. K. Park, I. Hwang and K. Kang, *Nat. Mater.*, 2020, **19**, 419–427.
352 M. Zhang, H. Liu, Z. Liu, C. Fang and Y. S. Meng, *ACS Appl. Energy Mater.*, 2018, **1**, 3369–3376.
353 X. He, J. Wang, R. Wang, B. Qiu, H. Frielinghaus, P. Niehoff, H. Liu, M. C. Stan, E. Paillard, M. Winter and J. Li, *J. Mater. Chem. A*, 2016, **4**, 7230–7237.
354 D. Chen, J. Wu, J. K. Papp, B. D. McCloskey, W. Yang and G. Chen, *Small*, 2020, e2000656.
355 G. H. Newman and L. P. Klemann, *J. Electrochem. Soc.*, 1980, **127**, 2097–2099.
356 W. Zuo, W. Zhu, D. Zhao, Y. Sun, Y. Li, J. Liu and X. W. Lou, *Energy Environ. Sci.*, 2016, **9**, 2881–2891.
357 X. Wu, G. L. Xu, G. Zhong, Z. Gong, M. J. McDonald, S. Zheng, R. Fu, Z. Chen, K. Amine and Y. Yang, *ACS Appl. Mater. Interfaces*, 2016, **8**, 22227–22237.
358 N. Yabuuchi, M. Kajiyama, J. Iwatate, H. Nishikawa, S. Hitomi, R. Okuyama, R. Usui, Y. Yamada and S. Komaba, *Nat. Mater.*, 2012, **11**, 512–517.
359 X. Wu, J. Guo, D. Wang, G. Zhong, M. J. McDonald and Y. Yang, *J. Power Sources*, 2015, **281**, 18–26.
360 S. Kumakura, Y. Tahara, K. Kubota, K. Chihara and S. Komaba, *Angew. Chem., Int. Ed.*, 2016, **55**, 12760–12763.
361 W. Zuo, J. Qiu, X. Liu, F. Ren, H. Liu, H. He, C. Luo, J. Li, G. F. Ortiz, H. Duan, J. Liu, M. S. Wang, Y. Li, R. Fu and Y. Yang, *Nat. Commun.*, 2020, **11**, 3544.
362 A. Skerra and J. Brickmann, *Biophys. J.*, 1987, **51**, 977–983.
363 C. Ling and R. Zhang, *Phys. Chem. Chem. Phys.*, 2017, **19**, 10036–10041.
364 W. Zuo, J. Qiu, C. Hong, X. Liu, J. Li, G. F. Ortiz, Q. Li, S. Zheng, G. R. Zheng and Y. Yang, *ACS Appl. Energy Mater.*, 2019, **2**, 4914–4924.
365 X. Liu, W. Zuo, B. Zheng, Y. Xiang, K. Zhou, Z. Xiao, P. Shan, J. Shi, Q. Li, G. Zhong, R. Fu and Y. Yang, *Angew. Chem., Int. Ed.*, 2019, **58**, 18086–18095.
366 C. Delmas, J. Braconnier, C. Fouassier and P. Hagenmuller, *Solid State Ionics*, 1981, **3-4**, 165–169.
367 M. H. Han, E. Gonzalo, G. Singh and T. Rojo, *Energy Environ. Sci.*, 2015, **8**, 81–102.
368 A. J. Perez, D. Batuk, M. Saubanère, G. Rousse, D. Foix, E. McCalla, E. J. Berg, R. Dugas, K. H. W. van den Bos, M.-L. Doublet, D. Gonbeau, A. M. Abakumov, G. Van Tendeloo and J.-M. Tarascon, *Chem. Mater.*, 2016, **28**, 8278–8288.
369 Y. Qiao, S. Guo, K. Zhu, P. Liu, X. Li, K. Jiang, C.-J. Sun, M. Chen and H. Zhou, *Energy Environ. Sci.*, 2018, **11**, 299–305.
370 X. Zhang, Y. Qiao, S. Guo, K. Jiang, S. Xu, H. Xu, P. Wang, P. He and H. Zhou, *Adv. Mater.*, 2019, **31**, e1807770.
371 N. Yabuuchi, R. Hara, K. Kubota, J. Paulsen, S. Kumakura and S. Komaba, *J. Mater. Chem. A*, 2014, **2**, 16851–16855.
372 H. Liu, J. Xu, C. Ma and Y. S. Meng, *Chem. Commun.*, 2015, **51**, 4693–4696.
373 X. Bai, M. Sathiya, B. Mendoza-Sánchez, A. Iadecola, J. Vergnet, R. Dedryvère, M. Saubanère, A. M. Abakumov, P. Rozier and J.-M. Tarascon, *Adv. Energy Mater.*, 2018, **8**, 1802379.
374 Q. Li, Y. Qiao, S. Guo, K. Jiang, Q. Li, J. Wu and H. Zhou, *Joule*, 2018, **2**, 1134–1145.
375 B. Mortemard de Boisse, S.-i. Nishimura, E. Watanabe, L. Lander, A. Tsuchimoto, J. Kikkawa, E. Kobayashi,

D. Asakura, M. Okubo and A. Yamada, *Adv. Energy Mater.*, 2018, **8**, 1800409.
376 Y. Li, X. Wang, Y. Gao, Q. Zhang, G. Tan, Q. Kong, S. Bak, G. Lu, X.-Q. Yang, L. Gu, J. Lu, K. Amine, Z. Wang and L. Chen, *Adv. Energy Mater.*, 2019, **9**, 1803087.
377 T. Risthaus, D. Zhou, X. Cao, X. He, B. Qiu, J. Wang, L. Zhang, Z. Liu, E. Paillard, G. Schumacher, M. Winter and J. Li, *J. Power Sources*, 2018, **395**, 16–24.
378 K. Dai, J. Mao, Z. Zhuo, Y. Feng, W. Mao, G. Ai, F. Pan, Y.-d. Chuang, G. Liu and W. Yang, *Nano Energy*, 2020, **74**, 104831.
379 W. Zuo, F. Ren, Q. Li, X. Wu, F. Fang, X. Yu, H. Li and Y. Yang, Insights of the anionic redox in P2–$Na_{0.67}Ni_{0.33}Mn_{0.67}O_2$, *Nano Energy*, 2020, **78**, 105285.
380 C. Zhao, Q. Wang, Y. Lu, L. Jiang, L. Liu, X. Yu, L. Chen, B. Li and Y.-S. Hu, *Energy Storage Mater.*, 2019, **20**, 395–400.
381 C. Zhao, Z. Yao, J. Wang, Y. Lu, X. Bai, A. Aspuru-Guzik, L. Chen and Y.-S. Hu, *Chem*, 2019, **5**, 2913–2925.
382 X. Rong, E. Hu, Y. Lu, F. Meng, C. Zhao, X. Wang, Q. Zhang, X. Yu, L. Gu, Y.-S. Hu, H. Li, X. Huang, X.-Q. Yang, C. Delmas and L. Chen, *Joule*, 2019, **3**, 503–517.
383 L. Yang, X. Li, J. Liu, S. Xiong, X. Ma, P. Liu, J. Bai, W. Xu, Y. Tang, Y. Y. Hu, M. Liu and H. Chen, *J. Am. Chem. Soc.*, 2019, **141**, 6680–6689.
384 X. Cao, X. Li, Y. Qiao, M. Jia, F. Qiu, Y. He, P. He and H. Zhou, *ACS Energy Lett.*, 2019, **4**, 2409–2417.
385 H. J. Kim, A. Konarov, J. H. Jo, J. U. Choi, K. Ihm, H. K. Lee, J. Kim and S. T. Myung, *Adv. Energy Mater.*, 2019, **9**, 1901181.
386 B. Song, E. Hu, J. Liu, Y. Zhang, X.-Q. Yang, J. Nanda, A. Huq and K. Page, *J. Mater. Chem. A*, 2019, **7**, 1491–1498.
387 T. Risthaus, L. Chen, J. Wang, J. Li, D. Zhou, L. Zhang, D. Ning, X. Cao, X. Zhang, G. Schumacher, M. Winter, E. Paillard and J. Li, *Chem. Mater.*, 2019, **31**, 5376–5383.
388 X. Cao, H. Li, Y. Qiao, X. Li, M. Jia, J. Cabana and H. Zhou, *Adv. Energy Mater.*, 2020, 1903785.
389 J. Li, T. Risthaus, J. Wang, D. Zhou, X. He, N. Ehteshami, V. Murzin, A. Friesen, H. Liu, X. Hou, M. Diehl, E. Paillard, M. Winter and J. Li, *J. Power Sources*, 2020, **449**, 227554.
390 P.-F. Wang, Y. Xiao, N. Piao, Q.-C. Wang, X. Ji, T. Jin, Y.-J. Guo, S. Liu, T. Deng, C. Cui, L. Chen, Y.-G. Guo, X.-Q. Yang and C. Wang, *Nano Energy*, 2020, **69**, 104474.
391 W. Zuo, J. Qiu, X. Liu, B. Zheng, Y. Zhao, J. Li, H. He, K. Zhou, Z. Xiao, Q. Li, G. F. Ortiz and Y. Yang, *Energy Storage Mater.*, 2020, **26**, 503–512.
392 M. Tamaru, X. Wang, M. Okubo and A. Yamada, *Electrochem. Commun.*, 2013, **33**, 23–26.
393 N. Yabuuchi, R. Hara, M. Kajiyama, K. Kubota, T. Ishigaki, A. Hoshikawa and S. Komaba, *Adv. Energy Mater.*, 2014, **4**, 1301453.
394 E. de la Llave, E. Talaie, E. Levi, P. K. Nayak, M. Dixit, P. T. Rao, P. Hartmann, F. Chesneau, D. T. Major, M. Greenstein, D. Aurbach and L. F. Nazar, *Chem. Mater.*, 2016, **28**, 9064–9076.
395 L. Yang, X. Li, X. Ma, S. Xiong, P. Liu, Y. Tang, S. Cheng, Y.-Y. Hu, M. Liu and H. Chen, *J. Power Sources*, 2018, **381**, 171–180.
396 J. Billaud, G. Singh, A. R. Armstrong, E. Gonzalo, V. Roddatis, M. Armand, T. Rojo and P. G. Bruce, *Energy Environ. Sci.*, 2014, **7**, 1387–1391.
397 R. A. House, U. Maitra, M. A. Perez-Osorio, J. G. Lozano, L. Jin, J. W. Somerville, L. C. Duda, A. Nag, A. Walters, K. J. Zhou, M. R. Roberts and P. G. Bruce, *Nature*, 2020, **577**, 502–508.
398 J. Wang, D. Zhou, X. He, L. Zhang, X. Cao, D. Ning, B. Yan, X. Qi, J. Li, V. Murzin, E. Paillard, X. Liu, G. Schumacher, M. Winter and J. Li, *ACS Appl. Mater. Interfaces*, 2020, **12**, 5017–5024.
399 I. D. Seymour, D. S. Middlemiss, D. M. Halat, N. M. Trease, A. J. Pell and C. P. Grey, *J. Am. Chem. Soc.*, 2016, **138**, 9405–9408.
400 R. Qiao, Q. Li, Z. Zhuo, S. Sallis, O. Fuchs, M. Blum, L. Weinhardt, C. Heske, J. Pepper, M. Jones, A. Brown, A. Spucces, K. Chow, B. Smith, P. A. Glans, Y. Chen, S. Yan, F. Pan, L. F. Piper, J. Denlinger, J. Guo, Z. Hussain, Y. D. Chuang and W. Yang, *Rev. Sci. Instrum.*, 2017, **88**, 033106.
401 Z. Shadike, E. Zhao, Y.-N. Zhou, X. Yu, Y. Yang, E. Hu, S. Bak, L. Gu and X.-Q. Yang, *Adv. Energy Mater.*, 2018, **8**, 1702588.
402 Z. Gong and Y. Yang, *J. Energy Chem.*, 2018, **27**, 1566–1583.
403 D. Liu, Z. Shadike, R. Lin, K. Qian, H. Li, K. Li, S. Wang, Q. Yu, M. Liu, S. Ganapathy, X. Qin, Q. H. Yang, M. Wagemaker, F. Kang, X. Q. Yang and B. Li, *Adv. Mater.*, 2019, **31**, e1806620.
404 H. Liu, C. R. Fell, K. An, L. Cai and Y. S. Meng, *J. Power Sources*, 2013, **240**, 772–778.
405 Y. Liao, Practical electron microscopy and database: www.globalsino.com/EM/, Global Sino, 2018.
406 Z. Wang, D. Santhanagopalan, W. Zhang, F. Wang, H. L. Xin, K. He, J. Li, N. Dudney and Y. S. Meng, *Nano Lett.*, 2016, **16**, 3760–3767.
407 Y. Gong, J. Zhang, L. Jiang, J. A. Shi, Q. Zhang, Z. Yang, D. Zou, J. Wang, X. Yu, R. Xiao, Y. S. Hu, L. Gu, H. Li and L. Chen, *J. Am. Chem. Soc.*, 2017, **139**, 4274–4277.
408 L. Zhou, M. Leskes, A. J. Ilott, N. M. Trease and C. P. Grey, *J. Magn. Reson.*, 2013, **234**, 44–57.
409 P. J. Reeves, I. D. Seymour, K. J. Griffith and C. P. Grey, *Chem. Mater.*, 2019, **31**, 2814–2821.
410 D. Foix, M. Sathiya, E. McCalla, J.-M. Tarascon and D. Gonbeau, *J. Phys. Chem. C*, 2016, **120**, 862–874.
411 S. Han, Y. Xia, Z. Wei, B. Qiu, L. Pan, Q. Gu, Z. Liu and Z. Guo, *J. Mater. Chem. A*, 2015, **3**, 11930–11939.
412 K. Shimoda, T. Minato, K. Nakanishi, H. Komatsu, T. Matsunaga, H. Tanida, H. Arai, Y. Ukyo, Y. Uchimoto and Z. Ogumi, *J. Mater. Chem. A*, 2016, **4**, 5909–5916.
413 G. Assat, A. Iadecola, D. Foix, R. Dedryvère and J.-M. Tarascon, *ACS Energy Lett.*, 2018, **3**, 2721–2728.
414 Z. W. Lebens-Higgins, H. Chung, M. J. Zuba, J. Rana, Y. Li, N. V. Faenza, N. Pereira, B. D. McCloskey, F. Rodolakis, W. Yang, M. S. Whittingham, G. G. Amatucci, Y. S. Meng, T. L. Lee and L. F. J. Piper, *J. Phys. Chem. Lett.*, 2020, **11**, 2106–2112.

415 F. Lin, Y. Liu, X. Yu, L. Cheng, A. Singer, O. G. Shpyrko, H. L. Xin, N. Tamura, C. Tian, T. C. Weng, X. Q. Yang, Y. S. Meng, D. Nordlund, W. Yang and M. M. Doeff, *Chem. Rev.*, 2017, **117**, 13123–13186.

416 A. Manceau, M. A. Marcus and S. Grangeon, *Am. Mineral.*, 2012, **97**, 816–827.

417 Q. Li, R. Qiao, L. A. Wray, J. Chen, Z. Zhuo, Y. Chen, S. Yan, F. Pan, Z. Hussain and W. Yang, *J. Phys. D: Appl. Phys.*, 2016, **49**, 413003.

418 L. Wang, J. Song, R. Qiao, L. A. Wray, M. A. Hossain, Y. D. Chuang, W. Yang, Y. Lu, D. Evans, J. J. Lee, S. Vail, X. Zhao, M. Nishijima, S. Kakimoto and J. B. Goodenough, *J. Am. Chem. Soc.*, 2015, **137**, 2548–2554.

419 J. Wu, J. Song, K. Dai, Z. Zhuo, L. A. Wray, G. Liu, Z. X. Shen, R. Zeng, Y. Lu and W. Yang, *J. Am. Chem. Soc.*, 2017, **139**, 18358–18364.

420 W. Yang, X. Liu, R. Qiao, P. Olalde-Velasco, J. D. Spear, L. Roseguo, J. X. Pepper, Y.-d. Chuang, J. D. Denlinger and Z. Hussain, *J. Electron Spectrosc. Relat. Phenom.*, 2013, **190**, 64–74.

421 R. Qiao, I. T. Lucas, A. Karim, J. Syzdek, X. Liu, W. Chen, K. Persson, R. Kostecki and W. Yang, *Adv. Mater. Interfaces*, 2014, **1**, 1300115.

422 Z. Zhuo, P. Lu, C. Delacourt, R. Qiao, K. Xu, F. Pan, S. J. Harris and W. Yang, *Chem. Commun.*, 2018, **54**, 814–817.

423 A. J. Achkar, T. Z. Regier, H. Wadati, Y. J. Kim, H. Zhang and D. G. Hawthorn, *Phys. Rev. B: Condens. Matter Mater. Phys.*, 2011, **83**, 081106.

424 R. Qiao, S. Roychoudhury, Z. Zhuo, Q. Li, Y. Lyu, J.-H. Kim, J. Liu, E. Lee, B. J. Polzin, J. Guo, S. Yan, Y. Hu, H. Li, D. Prendergast and W. Yang, *ChemRxiv*, 2019, DOI: 10.26434/chemrxiv.11416374.v11416372.

425 X. Liu, Y. J. Wang, B. Barbiellini, H. Hafiz, S. Basak, J. Liu, T. Richardson, G. Shu, F. Chou, T. C. Weng, D. Nordlund, D. Sokaras, B. Moritz, T. P. Devereaux, R. Qiao, Y. D. Chuang, A. Bansil, Z. Hussain and W. Yang, *Phys. Chem. Chem. Phys.*, 2015, **17**, 26369–26377.

426 R. Qiao, Q. Li, Z. Zhuo, S. Sallis, O. Fuchs, M. Blum, L. Weinhardt, C. Heske, J. Pepper, M. Jones, A. Brown, A. Spucces, K. Chow, B. Smith, P.-A. Glans, Y. Chen, S. Yan, F. Pan, L. F. J. Piper, J. Denlinger, J. Guo, Z. Hussain, Y.-D. Chuang and W. Yang, *Rev. Sci. Instrum.*, 2017, **88**, 033106.

427 A. Firouzi, R. Qiao, S. Motallebi, C. W. Valencia, H. S. Israel, M. Fujimoto, L. A. Wray, Y. D. Chuang, W. Yang and C. D. Wessells, *Nat. Commun.*, 2018, **9**, 861.

428 Z. Zhuo, C. D. Pemmaraju, J. Vinson, C. Jia, B. Moritz, I. Lee, S. Sallies, Q. Li, J. Wu, K. Dai, Y. D. Chuang, Z. Hussain, F. Pan, T. P. Devereaux and W. Yang, *J. Phys. Chem. Lett.*, 2018, **9**, 6378–6384.

429 Z. Zhuo, Y. S. Liu, J. Guo, Y. D. Chuang, F. Pan and W. Yang, *J. Phys. Chem. Lett.*, 2020, **11**, 2618–2623.

430 J. Xu, M. Sun, R. Qiao, S. E. Renfrew, L. Ma, T. Wu, S. Hwang, D. Nordlund, D. Su, K. Amine, J. Lu, B. D. McCloskey, W. Yang and W. Tong, *Nat. Commun.*, 2018, **9**, 947.

431 H. Ji, J. Wu, Z. Cai, J. Liu, D.-H. Kwon, H. Kim, A. Urban, J. K. Papp, E. Foley, Y. Tian, M. Balasubramanian, H. Kim, R. J. Clément, B. D. McCloskey, W. Yang and G. Ceder, *Nat. Energy*, 2020, **5**, 213–221.

432 G. H. Lee, J. Wu, D. Kim, K. Cho, M. Cho, W. Yang and Y. M. Kang, *Angew. Chem., Int. Ed.*, 2020, **59**, 8681–8688.

433 Z. W. Lebens-Higgins, N. V. Faenza, M. D. Radin, H. Liu, S. Sallis, J. Rana, J. Vinckeviciute, P. J. Reeves, M. J. Zuba, F. Badway, N. Pereira, K. W. Chapman, T.-L. Lee, T. Wu, C. P. Grey, B. C. Melot, A. Van Der Ven, G. G. Amatucci, W. Yang and L. F. J. Piper, *Mater. Horiz.*, 2019, **6**, 2112–2123.

434 N. Li, S. Sallis, J. K. Papp, J. Wei, B. D. McCloskey, W. Yang and W. Tong, *ACS Energy Lett.*, 2019, **4**, 2836–2842.

435 Y. L. Jeyachandran, F. Meyer, S. Nagarajan, A. Benkert, M. Bar, M. Blum, W. Yang, F. Reinert, C. Heske, L. Weinhardt and M. Zharnikov, *J. Phys. Chem. Lett.*, 2014, **5**, 4143–4148.

436 M. Tang, A. Dalzini, X. Li, X. Feng, P. H. Chien, L. Song and Y. Y. Hu, *J. Phys. Chem. Lett.*, 2017, **8**, 4009–4016.